

2005

An investigation of the propagation behavior of fretting fatigue cracks in Ti-6Al-4V

Hassan A. Fadag
University of Dayton

Follow this and additional works at: https://ecommons.udayton.edu/graduate_theses

Recommended Citation

Fadag, Hassan A., "An investigation of the propagation behavior of fretting fatigue cracks in Ti-6Al-4V" (2005). *Graduate Theses and Dissertations*. 2569.
https://ecommons.udayton.edu/graduate_theses/2569

This Dissertation is brought to you for free and open access by the Theses and Dissertations at eCommons. It has been accepted for inclusion in Graduate Theses and Dissertations by an authorized administrator of eCommons. For more information, please contact mschlange1@udayton.edu, ecommons@udayton.edu.

**AN INVESTIGATION OF THE PROPAGATION BEHAVIOR OF FRETTING
FATIGUE CRACKS IN Ti-6Al-4V**

A Dissertation

Submitted to

The School of Engineering

UNIVERSITY OF DAYTON

In Partial Fulfillment of the Requirement for

the Degree

Doctor of Philosophy in Mechanical Engineering

by

Hassan A. Fadag

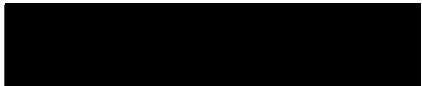
UNIVERSITY OF DAYTON

Dayton, Ohio

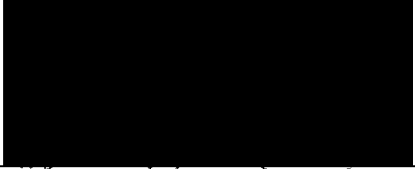
August 2005

**AN INVESTIGATION OF THE PROPAGATION BEHAVIOR OF FRETTING
FATIGUE CRACKS IN Ti-6Al-4V**


APPROVED BY:



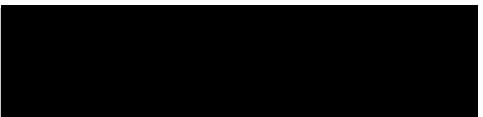
Vinod K. Jain, Ph.D.
Advisory Committee Chairman
Professor, Mechanical and Aerospace
Engineering Department




Aaron Altman, Ph.D.
Committee Member
Assistant Professor, Mechanical and
Aerospace Engineering Department




Donald L. Moon, Ph.D.
Associate Dean
Graduate Engineering Programs and Research
School of Engineering



Shankar Mall, Ph.D.
Research Advisor
Professor, Department of Aeronautic and
Astronautic, Air Force Institute of
Technology



Gerald J. Shaughnessy
Committee Member
Associate Professor, Mathematics
Department, College of Arts and Science



Joseph E. Saliba, Ph.D., P.E.
Dean
School of Engineering

ABSTRACT

AN INVESTIGATION OF THE PROPAGATION BEHAVIOR OF FRETTING FATIGUE CRACKS IN Ti-6Al-4V

Name: Hassan A. Fadag
University of Dayton

Advisor: Vinod K. Jain

Computational modeling of crack propagation behavior is conducted because it is very difficult to track crack growth under fretting conditions. Modeling and analysis of fretting crack propagation behavior was performed using a fracture mechanics code FRANC2D (FRANC2D/L). To obtain better accuracy, the crack growth model was combined with the finite element sub-modeling technique to estimate the crack path and crack propagation life in fretting fatigue specimens. This involved the computation of crack trajectories and stress intensity factors along the crack path, using the code FRANC2D, using different values of effective stress for cylindrical and flat pad geometries. The computed crack propagation lives were used to estimate the crack initiation lives by employing the results of a previous experimental study. In addition, a parametric study was performed to investigate the effects of other loading parameters, such as the normal load P , friction coefficient f , and Q/P ratio on the crack propagation behavior. The results show that as the effective stress increases, the crack propagation life decreases for both the cylindrical and flat pads. The effect of the effective stress on the cylindrical pad is more deleterious than that on the flat

pad. Finally, the effective stress was found to have the dominant effect on the propagation life followed by the ratio Q/fP . The coefficient of friction f has the least effect of the crack propagation behavior.

The effects of shot-peening and its various intensities on the propagation behavior of fretting fatigue cracks were also investigated. The results show that shot-peening improved the propagation life of fretting fatigue crack by about 3.4 times that of the unpeened specimens. However, the shot-peening intensity has no significant effect on the propagation life of the fretting fatigue cracks. The shot-peening intensity has greater impact in the initiation phase of the fretting fatigue crack life. The normalized initiation life increases, while the normalized propagation decreases with the shot-peening intensity.

ACKNOWLEDGMENTS

I would like to express my sincere gratitude and appreciation to my advisors, Dr. Shankar Mall and Dr. Vinod Jain for their encouragement and advice through the course of this study and giving me the opportunity to work in the interesting research field of fretting fatigue. I also want to thank them for helping me in tackling all the obstacles that I encountered through my research.

My appreciation and thanks are extended to Dr. Gerald Shaughnessy and Dr. Aaron Altman for serving on my advisory committee. I would also like to thank Dr. Kevin Hallinan, chairperson, Mechanical and Aerospace Engineering Department for all the help he has provided throughout my stay at The University of Dayton, especially for providing me with a computer system that helped me a lot in accomplishing my research. I also want to thank the Ohio Super Computer center for providing me time on the super computer to use ABAQUS to conduct the finite element analysis.

Thanks also go to many of my classmates for their sincere help through out my study at the University of Dayton.

Further, I would like to specially thank my wife Mai for her emotional support and dedication through my entire life. I would also like to thank my sons Mohammed and Mujtaba for their love and caring.

Finally but not last, I want to thank God for all the success; then, I want to express my sincere appreciation to my parents and my in-laws for their continuous support and encouragement.

TABLE OF CONTENTS

LIST OF FIGURES	x
LIST OF TABLES	xv
NOMENCALTURE.....	xvi
 CHAPTER I: INTRODUCTION.....	 1
1.1 Fretting Fatigue.....	1
1.2 Previous Work	2
1.2.1 Modeling of a Fretting System.....	2
1.2.2 The Effects of Fretting Parameters on Fretting Fatigue Life	3
1.2.2.1 Contact Pressure.....	3
1.2.2.2 Shear Force.....	4
1.2.2.3 The Coefficient of friction.....	4
1.2.2.4 Slip Amplitude.....	5
1.2.2.5 Cyclic Bulk Stress.....	5
1.2.2.6 Pad Geometry and Contact Width.....	6
1.2.3 Fretting Fatigue Crack Propagation.....	6
1.2.3.1 Crack Propagation Direction.....	7
1.2.3.2 Crack Growth Model.....	8
1.2.3.3 Crack Growth Criterion and Short Crack Regime Effect	10

1.2.4	The Effects of Shot-peening on Fretting Fatigue	11
1.3	Dissertation Objectives	14
CHAPTER II: CONTACT MECHANICS AND CRACK GROWTH ANALYSIS		21
2.1	Analytical Solution for Fretting Contact.....	21
2.1.1	Hertz Solution.....	23
2.1.2	The Effect of Tangential Load (Mindlin Solution).....	25
2.1.3	The Effect of Bulk Tensile Stress (Nowell and Hills Solution).....	28
2.1.4	Internal Stress Fields.....	30
2.1.5	Solution for Flat Pad with Rounded Edges.....	31
2.2	Fracture Mechanics	32
2.2.1	Concept of Linear Elastic Fracture Mechanics (LEFM)	32
2.2.2	Mixed-mode Interaction Criteria.....	36
2.2.2.1	The Maximum Tangential Stress Criterion.....	36
2.2.2.2	The Maximum Potential Energy Release Rate Criterion	37
2.2.2.3	The Minimum Strain Energy Density Criterion.....	38
2.2.3	Computation of Stress Intensity Factors	39
2.2.3.1	The Displacement Correlation Technique	40
2.2.3.2	The J-Integral Method.....	41
2.2.3.3	The Modified Crack Closure Integral Method (MCCI).....	42
2.2.4	Fatigue Crack Growth.....	44
2.2.4.1	Long Crack Threshold Growth Criterion.....	48
2.2.4.2	Short Crack Threshold Growth Criterion	48

2.3 Shot-Peening and Its Effect on Crack Growth Behavior.....	50
CHAPTER III: PROCEDURE	71
3.1 Loading Conditions.....	71
3.1.1 Effect of Cyclic Bulk Stress	72
3.1.2 Parametric Study	73
3.1.3 Effects of Shot-Peening Intensity	73
3.2 Finite Element Modeling	74
3.2.1 Global Model Analysis	74
3.2.2 Sub-Model Analysis.....	76
3.2.3 Reconstructing the Sub-Model	80
3.3 Crack Propagation Analysis.....	81
3.4 The Procedure Used to Calculate the Tensile Residual Stress.....	84
CHAPTER IV: RESULTS AND DISCUSSION.....	109
4.1 Effect of the Effective Stress (σ_{eff})	110
4.1.1 Crack Growth Criteria	110
4.1.2 Effective Stress Intensity Factors (ΔK_{eff}).....	111
4.1.3 Crack Propagation Life (N_p).....	112
4.2 Parametric Study.....	115
4.3 Effects of Shot-Peening and its Intensity	115
4.3.1 Crack Initiation Location in Shot-Peened Specimens	116
4.3.2 Shot-Peening Intensity and the Effective Stress Intensity Factors (ΔK_{eff}).....	118

4.3.3 Effect of Shot-Peening Intensity on Crack Propagation Life (N_p).....	118
4.3.4 Parametric Study for Shot-Peened Specimens.....	121
4.3.4.1 Effect of the Ratio Q/fP	121
4.3.4.2 Effect of Residual Stress Relaxation	122
CHAPTER V: CONCLUSION AND FUTURE WORK.....	156
5.1 Conclusions	156
5.2 Recommendations for Future Work	159
APPENDICES.....	160
A. Evaluating the Experimental Data	160
B. Typical ABAQUS Input File	165
C. Residual Stress Input File Format.....	172
C.1 The Residual Stress Input File Format	172
C.2 Detailed Description	172
BIBLIOGRAPHY	174

LIST OF FIGURES

Figure 1.1 Examples of mechanical systems involving the fretting fatigue process.....	15
Figure 1.2 Fan and compressor blade dovetail joint.....	16
Figure 1.3 Schematic of a fretting model.....	17
Figure 1.4 Fretting fatigue versus clamping load.....	18
Figure 1.5 Coefficient of friction versus slip amplitude.....	19
Figure 1.6 Relation between wear and fatigue strength as a function of slip amplitude.....	20
Figure 2.1 Schematic of a fretting model.....	54
Figure 2.2 Two curved bodies under contact subjected to normal load, P , and shear load, Q	55
Figure 2.3 Schematic of the stick/slip zones of two bodies under contact	56
Figure 2.4 Half plane loaded by normal and shear tractions applied on the contact surface ...	57
Figure 2.5 Model of an elliptical hole in an infinite flat plate.....	58
Figure 2.6 Schematic of the plastic zone around the crack tip	59
Figure 2.7 A center crack in an infinite flat plate	60
Figure 2.8 Definition of the coordinate axis ahead of the crack tip	61
Figure 2.9 Crack opening modes.....	61
Figure 2.10 Quarter-point elements at the crack tip.....	62
Figure 2.11 A schematic of the J -Integral contour.....	63
Figure 2.12 Analytical crack-closure integral method.....	64

Figure 2.13 Behavior of fatigue crack growth in metals	65
Figure 2.14 Schematic of a Kitagawa diagram	66
Figure 2.15 Short crack effect on the fracture mechanics threshold ΔK_{Th}	67
Figure 2.16 Simulation of shot-peening process	68
Figure 2.17 The plastic deformation process that occurs in shot-peening.....	69
Figure 2.18 A typical residual stress profile	70
Figure 3.1 Flow chart summarizing the crack propagation analysis	86
Figure 3.2 Dimensions of the cylindrical and flat pads used in this study	87
Figure 3.3 Global model of the cylindrical pad case.....	88
Figure 3.4 Global model of the flat pad case	89
Figure 3.5 Comparison between the FEM and the analytical solutions (cylindrical pad)	90
Figure 3.6 Comparison between the FEM and the analytical solutions (flat pad).....	91
Figure 3.7 Schematic of a sub-model	92
Figure 3.8 A schematic showing the driven nodes	92
Figure 3.9 Sub-model of the cylindrical pad case.....	93
Figure 3.10 Sub-model of the flat pad case	93
Figure 3.11 Variation of normalized x -direction stress around the trailing edge (cylindrical pad)	94
Figure 3.12 Variation of normalized x -direction stress around the trailing edge (flat pad)	95
Figure 3.13 Comparison of FRANC2D/L and ABAQUS solutions (cylindrical pad).....	96
Figure 3.14 Comparison of FRANC2D/L and ABAQUS solutions (flat pad).....	97
Figure 3.15 Schematic of the sub-model for the cylindrical pad with boundary and loading conditions as used in FRANC2D	98

Figure 3.16 Schematic of the sub-model for the flat pad with boundary and loading conditions as used in FRANC2D	98
Figure 3.17 Crack growth trajectory	99
Figure 3.18 The initial configuration of the crack in FRANC2D/L showing a mesh of triangulated elements	99
Figure 3.19 Flow chart summarizing the crack growth steps	100
Figure 3.20 Compressive residual stress profiles	101
Figure 3.21 The residual stress profiles	102
Figure 4.1 Crack-size dependent threshold as a function of the crack length (cylindrical pad)	123
Figure 4.2 Crack-size dependent threshold as a function of the crack length (flat pad)	124
Figure 4.3 Effective stress intensity factor as a function of crack length and loading level (cylindrical pad).....	125
Figure 4.4 Effective stress intensity factor as a function of crack length and loading level (flat pad).....	126
Figure 4.5 Crack propagation life as a function of initial crack length.....	127
Figure 4.6 Normalized crack propagation life as a function of initial crack length	128
Figure 4.7 Crack propagation lives for the cylindrical pads	129
Figure 4.8 Crack propagation lives for the flat pads.....	130
Figure 4.9 Crack propagation life as a function of the effective stress	131
Figure 4.10 Crack initiation life as a function of the effective stress	132
Figure 4.11 Normalized crack propagation life as a function of the effective stress.....	133

Figure 4.12	Normalized crack initiation life as a function of the effective stress	134
Figure 4.13	Crack propagation life as a function of the normal load.....	135
Figure 4.14	Crack propagation life as a function of coefficient of friction	136
Figure 4.15	Crack propagation life as a function of ratio Q/P	137
Figure 4.16	Total x -direction stress as a function of the specimen depth (0% stress relaxation)	138
Figure 4.17	Crack trajectory in the unpeened specimen	139
Figure 4.18	Crack trajectory in the shot-peened specimen with 10A with no residual stress relaxation.....	140
Figure 4.19	Estimation of the minimum initial crack length for the unpeened and shot-peened specimens.....	141
Figure 4.20	The effective stress intensity factor as a function of crack length and shot-peening intensity (upper branch)	142
Figure 4.21	Crack propagation lives as a function of shot-peening intensity (0% stress relaxation).....	143
Figure 4.22	Comparison of the crack propagation lives of shot-peened specimens (upper branch) with the unpeened specimen (0% stress relaxation)	144
Figure 4.23	Variation of crack propagation life with shot-peening intensity.....	145
Figure 4.24	Variation of crack initiation life with shot-peening intensity.....	146
Figure 4.25	Variation of the normalized crack propagation life with shot-peening intensity.	147
Figure 4.26	Variation of the normalized crack initiation life with shot-peening intensity.....	148
Figure 4.27	Crack propagation life as a function of ratio Q/P in 10A shot-peened specimen	149

Figure 4.28 Crack propagation life as a function of the normal load in 10A shot-peened specimen	150
Figure 4.29 Total x -direction stress as a function of the specimen depth (50% stress relaxation)	151
Figure 4.30 Crack propagation lives as a function of shot-peening intensity (50% stress relaxation)	152
Figure 4.31 Comparison of the crack propagation lives of shot-peened specimens (lower branch) with the unpeened specimen (50% stress relaxation)	153
Figure A.1 The total fretting fatigue life as a function of the effective stress (cylindrical pad)	161
Figure A.2 The total fretting fatigue life as a function of the effective stress (flat pad)	162

LIST OF TABLES

Table 3.1 Loading conditions for the cylindrical and flat pads.....	103
Table 3.2 Experimental fretting fatigue lives	104
Table 3.3 Loading conditions for the parametric study	105
Table 3.4 Experimental data from Ref. [44].....	106
Table 3.5 The mesh sizes used for global and sub-models	107
Table 3.6 The boundary condition errors for the sub-models based on σ_{xx}	107
Table 3.7 The curve-fitting constants of Equation (3.12).....	108
Table 3.8 Critical values of the residual stress profiles (Figure 3.21).....	108
Table 4.1 Summary of the parameters involved in constructing Figures 4.1 and 4.2	154
Table 4.2 Propagation life as a function of initial crack length.....	154
Table 4.3 Data used for the calculation of crack initiation life	155
Table 4.4 Data used for the parametric study	155
Table A.1 Experimental fretting fatigue lives for the cylindrical pad case	163
Table A.2 Experimental fretting fatigue lives for the flat pad case.....	164

NOMENCLATURE

a	Half width of a contact zone
b	Half thickness of the specimen
c	Half width of the stick zone
C	The sub-model length
dl/dN	Crack growth rate
E	Modulus of elasticity
f	Coefficient of friction
F_x	Nodal force in x -direction
F_y	Nodal force in y -direction
g	The amount of x -direction overlap between two bodies in contact
G	Modulus of rigidity or potential energy release rate
G_c	The critical potential energy release rate
h	The amount of y -direction overlap between two bodies in contact
k	The relative radius of curvature
K_C	Fracture toughness
K_I	Mode I stress intensity factor
K_{II}	Mode II stress intensity factor
K_{max}	Maximum stress intensity factor

K_{min}	Minimum stress intensity factor
K_{Tb}^{eff}	Effective long crack threshold
l	Crack length
l_i	Initial crack length
l_o	Small crack parameter
L	The element size
N_i	Number of crack initiation cycles
N_p	Number of crack propagation cycles
N_t	Total number of cycles
J	J integral
p	The pressure in the contact zone
p_o	The maximum contact pressure
p_L	The tractions at the left edge of the sub-model
p_R	The tractions at the right edge of the sub-model
P	Normal load (or contact load)
q	The surface shear stress
Q_{max}	Maximum shear force (or maximum tangential force)
Q_{min}	Minimum shear force (or minimum tangential force)
r	The radial distance from the crack tip
R	Bulk stress ratio
R_L	Stress intensity factors ratio or local stress ratio
S	Strain energy density

u or u	Relative displacement in x -direction
v or v	Relative displacement in y -direction
x	Coordinate along the contact surface
y	Coordinate perpendicular to the contact surface
Δ	Slip amplitude
δ	Crack opening displacement
ΔK	Stress intensity range
ΔK_C	Fracture toughness
ΔK_{eff}	Effective stress intensity factor
ΔK_{Th}^{eff}	Effective long crack threshold
ΔK_{Th}	Stress intensity threshold
ΔK_{Th}^{LC}	Long crack threshold
ΔK_{Th}^{SC}	Size-dependent threshold
Δl	Incremental crack length
ϵ_{bc}	Boundary condition error
ϵ_d	Discretization error
ϵ_s	The appropriate error level that leads to the desired accuracy for the sub-model
ϵ_{xx}	Strain in x -direction
γ	Shear modulus
λ	Surface energy per unit area

θ	Crack orientation angle
σ	Far field stress
σ_c	The critical applied stress or compressive residual stress
σ_e	Endurance limit
σ_{eff}	Effective stress
σ_{max}	Maximum axial bulk stress
σ_{min}	Minimum axial bulk stress
σ_p	The distributed normal load
σ_{Tb}^{SC}	Short crack threshold stress
σ_{xx}	Stress in x -direction
σ_{xy}	Shear Stress
σ_y	Stress in y -direction
σ_t	Tensile residual stress
τ_Q	The distributed tangential load
τ_{xy}	Shear stress
ν	Poisson's ratio

CHAPTER I

INTRODUCTION

1.1 Fretting Fatigue

Fretting fatigue occurs whenever a joint is subjected to small cyclic sliding motion on the order of $25 - 100 \mu\text{m}$ [1]. Fretting fatigue usually occurs in bolted and riveted joints, shrink-fitted components, and in other similar joints as shown in Figure 1.1. One of the most common examples of mechanical failures caused by fretting fatigue, is the failure of the dovetail joints in the blade and disk attachments of turbine engines (Figure 1.2). Fretting fatigue is usually associated with loading conditions which happen when one of the contacting parts is subjected to cyclic loading. This type of loading condition causes micro-slip in the contact region, resulting in wear and surface damage that consequently decreases the fatigue resistance of the material and accelerates cracks nucleation [2, 3] as compared to plain fatigue. Therefore, premature failure of the components can occur by fretting under stresses that are much lower than the design stress, resulting in shorter component life. Sometimes, conservative design adjustments are employed to compensate for the damage caused by fretting fatigue. These adjustments lead to larger and less efficient parts and increase their associated maintenance expenses [4]. Therefore, a better understanding of the fundamental concepts of fretting fatigue is essential from both the standpoint of durability and cost-efficiency.

The study of fretting fatigue is multidisciplinary since it involves different areas of knowledge such as friction, wear, corrosion, materials and fatigue. For instance, fretting fatigue analysis takes into consideration some of the following processes: adhesion of surfaces, breaking of adhesive bonds due to slip, production of wear debris, initiation and propagation of cracks. The processes of initiation and propagation of fretting cracks are considered crucial since they lead to component failure. Therefore, a better understanding of these two processes is a key to developing fretting resistant designs and is a major focus of this work.

1.2 Previous Work

In this section, three different dimensions of research in the study of fretting fatigue will be reviewed. The first part will discuss some of the findings around the effects of fretting parameters on the fretting fatigue life. Some of the research carried out in the investigation of the propagation behavior of the fretting fatigue cracks will be outlined in the second part. Finally, the effects of shot-peening on fretting fatigue life will be reviewed. However, before starting these discussions, the modeling of a fretting system will be discussed briefly.

1.2.1 Modeling of a Fretting System

A fretting system is simply modeled as a fatigue specimen sandwiched between two cylindrical or flat pads. A normal load P , is applied on these pads (Figure 1.3) through the use of lateral springs, and the specimen is loaded by a cyclic axial stress (σ_{min} to σ_{max}) that produces micro-slip between the pad and specimen resulting in a shear load Q , which varies from Q_{min} to Q_{max} .

1.2.2 The Effects of Fretting Parameters on Fretting Fatigue Life

The phenomenon of fretting fatigue is not completely understood because several factors can affect the fretting behavior of materials. According to Dobromirski [5], there are as many as fifty factors that can affect the fretting process. Some of these factors are contact pressure, coefficient of friction, slip amplitude, cyclic axial stress, axial stress ratio, tangential shear stress at the interface, and the number of fretting cycles [6, 18]. Many experimental studies have suggested that there are strong relationships between some of these factors. These interrelationships imply that the effects of each individual factor on the fretting fatigue behavior should be investigated systematically. Some of the work done in the effects of these parameters on the fretting fatigue life will be reviewed in the following paragraphs.

1.2.2.1 *Contact Pressure*

Adibnazari and Hoeppner [8] investigated the effect of contact pressure on 7075-T6-Aluminum alloy and the titanium alloy Ti-6Al-4V. They introduced the pressure threshold concept, which states that above a certain normal pressure, fretting fatigue is independent of pressure (Figure 1.4). Nakazawa *et al.* [9] further studied the effect of the normal load, which is related directly to the contact pressure, on the fretting life of high strength steel and titanium alloy Ti-6Al-4V. They reported that the fretting fatigue life decreased monotonously with the increasing of the contact pressure and then became constant at higher pressures. Moreover, Nakazawa *et al.* [9] noted that the tangential shear stress at the interface increased with pressure.

1.2.2.2 *Shear Force*

Lee *et al.* [10] investigated the fretting fatigue behavior of high strength steel at various contact loads. They found that the friction force amplitude increased linearly with the contact load up to a certain limit; then the rate of increase dropped and became non-linear. Since the fretting fatigue life decreases monotonously with the increasing of the contact pressure, consequently the fretting fatigue life is expected to decrease with increasing of the friction force amplitude. In his dissertation, Leiva [4] studied the effect of shear force on the fretting fatigue behavior of Ti-6Al-4V. He found that the number of cycles to failure for specimens subjected to fretting fatigue decreased as the shear force increased (keeping the other factors constant).

1.2.2.3 *The Coefficient of friction*

Nishioka and Hirakawa [11] studied the variation of the coefficient of friction for carbon steel in the fretting fatigue process. They found that its value rises initially, but becomes stable after about 100 cycles. Further, they discovered that the coefficient of friction increased gradually with slip amplitude, but reached its maximum value at about 10 to 20 microns of slip (Figure 1.5), while the fretting fatigue strength was reported to reach its lowest value at about 10 to 20 microns of slip (Figure 1.6). This similarity suggests that there is a direct link between the coefficient of friction and the fretting fatigue life. The maximum coefficient of friction can be considered at the transition of partial slip to gross slip or alternatively the transition point from the minimum fatigue life to gradually increasing fatigue life. Furthermore, Nix, Lindley and Endo *et al.* [12, 13] also found that the coefficient of friction rapidly increased initially, then decreased to a stabilized value. Likewise, the fretting

wear rate was shown to rapidly rise initially and then slow down to a steady value. The variation of coefficient of friction in the early stage of the test is presumed to scarcely affect the results of experiments; the steady state value is commonly used for fretting fatigue analysis.

1.2.2.4 *Slip Amplitude*

Vingsbo and Söderberg [14] investigated the effect of the slip amplitude and the shear force in a low carbon steel. They introduced the concept of fretting maps to characterize the fretting regimes; three regimes were identified: stick, partial slip, and gross slip. The authors found that the fretting fatigue life decreased as the slip amplitude increased up to a certain point. After this point the fretting life started to increase with the slip amplitude. This point is considered the point of transition from partial slip to gross slip regime (Figure 1.6). The higher slip amplitude is associated with increased fatigue life due to the wearing away of the initiated cracks. From this, one can conclude that the partial slip regime has the most detrimental effect on the material's fatigue properties. Furthermore, Jin and Mall [15] found the same effect of slip amplitude on the titanium alloy Ti-6Al-4V. They observed that the minimum fretting fatigue life occurred at slip amplitude of 50-60 μm . Once gross slip takes place, the fretting wear dominates during the fretting process, which results in longer fatigue life.

1.2.2.5 *Cyclic Bulk Stress*

Wallace and Neu [16] investigated the effect of the cyclic bulk stress amplitude, along with other fretting loading factors, on the fretting life of Ti-6Al-4V. They found that the bulk stress amplitude had the dominant effect on fretting fatigue life. The fretting fatigue life diminished as the

bulk stress amplitude increased. Rather than study the effect of the global fretting factors, Iyer [17] instead focused on the effect of local fretting factors such as contact peak pressure, local cyclic bulk stress range, local cyclic shear stress range, and so on. His results revealed that the fretting fatigue life decreases as the local bulk stress increases.

1.2.2.6 *Pad Geometry and Contact Width*

In cylindrical fretting pads, the contact width increases as the normal load increases by a factor of $(\text{Constant} \times P)^{1/2}$. Nowell *et al.* [18] investigated the effect of the contact width on fretting fatigue behavior. They independently varied the peak contact pressure and the contact width by changing the normal load and the fretting pad radius. Their experimental results revealed that large contact widths resulted in short fatigue life. Lee *et al.* [10] also investigated the effect of pad geometry on the fretting fatigue behavior of high strength steel at various contact loads. They concluded that at high contact load, fretting fatigue life remained almost unchanged with changes in the fretting pad radius. At low contact load, however, the fretting fatigue life was found to increase with increases in the pad radius.

1.2.3 Fretting Fatigue Crack Propagation

Generally, the life of any component subjected to fretting fatigue is divided into two portions: crack initiation and crack propagation. A number of studies have addressed the problem of fretting fatigue crack initiation and propagation both experimentally and analytically [6-27]. It is very difficult, if not impossible to quantify the crack initiation portion of the component life [19-21]. However, the crack propagation portion of life can be measured experimentally by counting the number of fatigue striations [4, 19]. The initiation

portion of the component life can then be calculated by subtracting the propagation part of life from the total life.

The propagation behavior of the fatigue cracks is considered a key issue in scheduling of inspection and maintenance of a variety of machines. Aerospace structures and engines are an obvious example where failure could lead to catastrophic loss of life. Thus, quantifying the crack propagation behavior helps to predict the period of critical crack growth, and hence the service life of the component.

In general, the experimental tracking of crack propagation under fretting fatigue condition is a very complex task because these cracks are very small and hidden under the fretting pad. However, given the critical need to better understand the failure and damage tolerance of structural parts, computational modeling of the fretting crack propagation behavior is considered a good alternative approach. This is the main focus of this dissertation. In the following paragraphs, some of the work done in the investigation of the propagation behavior of the fretting fatigue cracks will be discussed.

1.2.3.1 *Crack Propagation Direction*

Fannes [22] studied the crack growth behavior of fretting fatigue cracks of intermediate lengths; i.e. larger than several material grains. He found that the growth of the cracks was along a path where the Mode II stress intensity factor approaches to zero. As the stress field becomes influenced by a far field axial stress, Fannes noticed that the crack kinked in a direction perpendicular to that stress. This means that fretting cracks of intermediate lengths seem to grow in pure Mode I loading despite the biaxial nature of the fretting fatigue loading. Mutoh and his co-workers [23] focused on the local singular stress field at the fatigue

crack tip or at the contact edge, where the fretting cracks usually occurred, depending on the numerical analysis results achieved by the finite element code ABAQUS. They proposed that the effect of fretting conditions could be represented by the local stress field, which could describe the fretting fatigue crack initiation and propagation behavior. They also performed an analytical simulation of the fretting fatigue crack propagation and found that the fretting crack was always under mixed-mode loading conditions, and its trajectory could be estimated by the Erdogan and Sih's maximum tangential stress criterion [24]. Shkarayev and Mall [25] developed a model that quantitatively evaluated the fretting fatigue crack propagation behavior. They also assumed that the crack growth direction was governed by the maximum tangential stress criterion. They found that the fretting crack kinked in a direction almost normal to the contact surface, since the effect of the contact stresses were overcome by a stress state corresponding to the far field cyclic axial stress.

1.2.3.2 *Crack Growth Model*

Navarro *et al.* [26] proposed a procedure for estimating the total life of a fretting fatigue crack. This procedure analyzed the fretting fatigue crack initiation and propagation separately. The correlation between crack initiation and propagation was made considering a non-arbitrary crack initiation length provided by the model. The propagation of the crack was analyzed using different fatigue crack propagation laws, with some modifications to take the short crack growth into account. The results obtained by this procedure were then compared to fatigue life obtained in various fretting fatigue tests on 7075-T6 aluminum alloy. In another study involving the same procedure, Navarro and his colleagues [27] used two different laws of crack growth to evaluate the propagation life; the Paris law [28] and the Lankford curve [29].

These two laws estimated an upper and lower bound, respectively for the fatigue life of the specimen; the actual life lying somewhere in between. Golden and Grandt [3] developed a fracture mechanics based crack propagation model that worked directly with the output of a fretting fatigue contact mechanics model. During their study, they conducted a series of fretting experiments on specimens that already had initial fretting cracks. The propagation of these cracks compared well with the propagation analysis results achieved by the developed model. In the developed propagation model, the crack growth rate dl/dN , was calculated using the following formula:

$$dl/dN = b \left(\frac{\Delta K_{eff}}{\Delta K_{th}} \right)^p \left[\ln \left(\frac{\Delta K_{eff}}{\Delta K_{th}} \right) \right]^q \left[\ln \left(\frac{\Delta K_c}{\Delta K_{eff}} \right) \right]^g \quad (1.1)$$

where,

$$\Delta K_{eff} = K_{max} (1 - R_L)^m \quad (1.2)$$

$$\Delta K_{th}^{LC} (\text{MPa mm}^{1/2}) = 133 \quad b = 3.5 \times 10^{-7} \quad q = 0.235 \quad m (R_L > 0) = 0.72$$

$$\Delta K_c (\text{MPa mm}^{1/2}) = 2083 \quad p = 3.71 \quad g = -0.0066 \quad m (R_L < 0) = 0.275$$

Here ΔK_c and ΔK_{th} are the crack growth threshold and the fracture toughness for the specimens' material used in this study, which is the titanium alloy, Ti-6Al-4V. The remaining constants are curve-fitting parameters that result in dl/dN , in units of mm/cycle. These constants were curve-fitting parameters from crack growth data measured from standard tests on Ti-6Al-4V for a stress ratio of -1, 0.1, 0.5 and 0.8 [30]. ΔK_{eff} is the crack growth driving parameter according to Equation (1.2), which is known as Walker's equation [31]. The stress intensity ratio R_L , was defined as K_{min}/K_{max} and K_{min} was allowed to take negative values. ΔK_{eff} was assumed to be a function of Mode I stress intensity factors (K_{max} and K_{min}) only. Shkarayev

and Mall [25] used the same crack growth model in their study. According to Haritos [32], this crack growth model is considered one of two models proposed for predicting crack growth rates in aircraft engine materials under typical operating conditions.

1.2.3.3 *Crack Growth Criterion and Short Crack Regime Effect*

Nicholas *et al.* [33] developed a fracture mechanics methodology for the fretting fatigue problem. They found that this methodology had more value in predicting failure than for the analysis of the stress field. The reason for this was that the threshold stress intensity factor was available for long cracks under Mode I only or mixed-mode conditions and could be easily corrected for short crack effects through the use of the Kitagawa diagram [34]. Therefore, Nicholas and his colleagues used this methodology to determine the conditions for propagation or non-propagation of cracks that initiated in the edge of contact region based on a mixed-mode driving force and a short crack corrected threshold.

Chan *et al.* [35] developed a fracture mechanics-based methodology for predicting the limiting threshold stress for high-cycle fretting fatigue in structural alloys. In their study, the limiting threshold stress ranges for the non-propagation of fretting fatigue cracks were predicted on the basis that the fretting fatigue cracks are small cracks that exhibit a size-dependent growth threshold and propagate at stress intensity ranges below the large-crack threshold. Furthermore, Golden *et al.* [2] measured the crack propagation threshold of cracks formed by fretting through the testing of a unique fatigue specimen designed from the fretting pads used in previous fretting experiments. In their study, Golden and his colleagues tested some specimens with crack lengths that were less than or equal to the short crack parameter, l_c .

They found that the experimental threshold stress was slightly lower than the linear elastic fracture mechanics (LEFM) long crack threshold.

1.2.4 The Effects of Shot-peening on Fretting Fatigue

Research literature explains that fretting fatigue strength and life can be enhanced by a variety of techniques involving the surface modifications of the specimen under analysis. Some of these techniques are shot-peening [36, 37], coatings [38, 39], and soft shims [40]. Shot-peening is considered one of the most widely used techniques of surface treatments, especially for aeronautical and automotive components. Shot-peening involves bombarding the surface of the specimen with small, hard, often steel balls. These balls cause biaxial yielding in compression under each point of impact; hence a biaxial compressive residual stress occurs on the specimen surface due to the elastic recovery of the unyielded material beneath. Shot-peening changes the physical and the mechanical properties of the specimen material, such as the surface roughness and hardness. The residual stress induced by shot-peening is compressive on and near the specimen surface and tensile within the rest of the specimen thickness. This indicates that the residual stress profile induced by shot-peening changes with depth from the specimen surface. Generally, the benefits from shot-peening are contained within the compressive zone of the residual stress profile. This compressive zone tends to prevent or suppress the initiation and propagation of fretting cracks up to a particular level. Moreover, shot-peening technique helps in closing pre-existing cracks as long as they fall within the compressive zone. Many studies have shown the effects of shot-peening on the fretting fatigue behavior. In the following discussion, some of these studies will be introduced.

Namjoshi *et al.* [41] investigated the effects of shot-peening on the fretting fatigue behavior of the titanium alloy Ti-6Al-4V. They found that the fretting fatigue life was improved due to shot-peening up to one and a half orders of magnitude, particularly at low stress values. In most cases, only the compressive zone of the residual stress profile can be measured experimentally by the use of X-Ray diffraction analysis. However, the profile of the compensatory tensile residual stress is not precisely known. In this study, Namjoshi and his co-workers developed a mathematical procedure to derive this profile. This procedure will be used in this dissertation and will be discussed in detail in Chapter II. In addition, Namjoshi *et al.* observed that the fretting cracks initiated inside the specimen surface. Furthermore, Lee *et al.* [42] investigated the fretting fatigue behavior of shot-peened titanium alloy, Ti-6Al-4V at room and elevated temperatures. Their fretting fatigue tests were conducted under constant stress amplitude over a wide range of maximum stresses and a fixed stress ratio of 0.1. After measuring the residual stress by X-Ray diffraction technique before and after the fretting test, the study revealed that the residual compressive stress zone was relaxed during the process of fretting fatigue. They observed that elevated temperatures induced more stress relaxation, which in turn reduced the fretting fatigue life significantly at 260 °C. In addition, they found that this stress relaxation also affected the location of fretting crack initiation; in other words, the fretting cracks could initiate at the contact surface of the fretting specimen instead of inside it. In their study, Shkarayev and Mall [25] developed a computational model, which studies the effects of shot-peening on the propagation behavior of the fretting induced cracks. They used a finite element sub-modeling technique along with their crack growth model to make a precise prediction about the propagation life. Their results revealed a significant increase, of

about 2 to 3 times, in the crack propagation life of shot-peened specimens relative to unpeened specimens, which is in agreement with the experimental observations.

There are several parameters involved in the shot-peening process. Some of these parameters include shot-peening media (including hardness and shape), shot velocity or pressure, angle of impingement, intensity, percentage of surface coverage, etc. [43]. Numerous studies have investigated the effects of these shot peening parameters on plain fatigue; however very little work has been carried out to study the effects of these parameters on fretting fatigue. Sabelkin *et al.* [44] investigated the effects of one of the important shot-peening parameters – shot peening intensity - on the fretting fatigue behavior of the titanium alloy, Ti-6Al-4V. All other parameters were kept identical. Three different shot-peening intensities, 4A, 7A, and 10A with 100% surface coverage were tested. The researchers found that shot-peening improved the fretting fatigue life of Ti-6Al-4V; this improvement was directly related to the shot peening intensity. They also found that the residual stress zone induced by shot-peening was directly affected by the shot-peening intensity. Higher intensity from 4A to 10A led to a higher level of compensatory tensile stress and shifted the boundary between the negative and the positive residual stress zones to a larger depth. Further, Sabelkin *et al.* [44] observed that the shot-peening induced residual stresses were relaxed during the fretting fatigue process. They also found that the fretting cracks initiated on the contact surface for specimens with 4A and 7A intensities and at depth away from the contact surface of specimens with 10A intensity.

1.3 Dissertation Objectives

In this dissertation, the fretting fatigue cracks propagation behavior in the titanium alloy Ti-6Al-4V, was studied using a computational modeling method based on the LEFM concept. This method involves the knowledge of crack path, determination of the fracture parameters along the crack path, and calculating the propagation life using a crack growth model.

This dissertation includes the following:

- Use of the finite element sub-modeling technique to achieve precise stress, strain, and displacement fields for all the studied cases to help in reducing the finite element computation time.
- Study the effects of various fretting fatigue parameters on the propagation behavior of the fretting induced cracks. These parameters are the contact pressure, the friction force, the coefficient of friction, the cyclic axial stress, and the fretting pad geometry.
- Quantify the fretting cracks initiation lives for the tests that study the effects of the cyclic axial stress only. This is done by using the predicted propagation lives of these tests with the failure lives of a previous experimental study involving the same loading conditions and the same types of fretting pads.
- Study the effects of shot-peening and its intensities on the propagation behavior of fretting fatigue cracks and relating them to the experimental results of a previous study involving the same loading conditions and same shot-peening intensities.

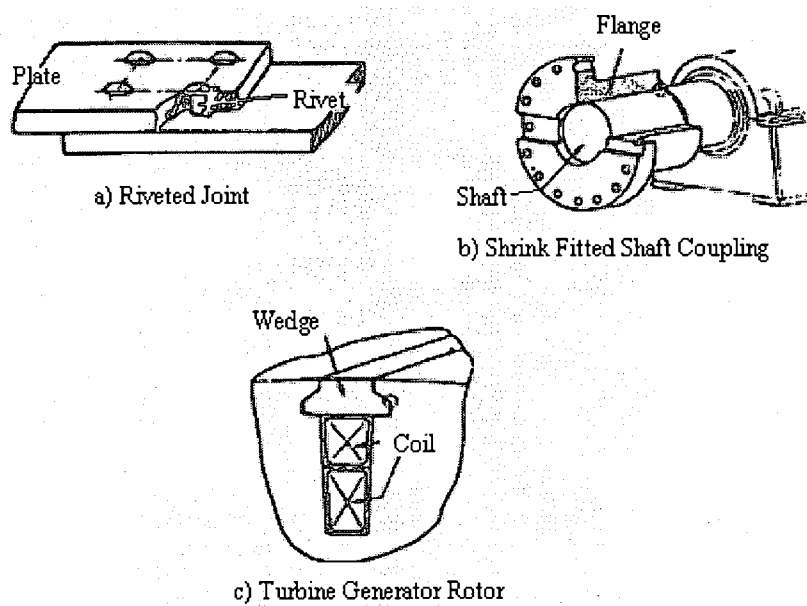


Figure 1.1 Examples of mechanical systems involving the fretting fatigue process

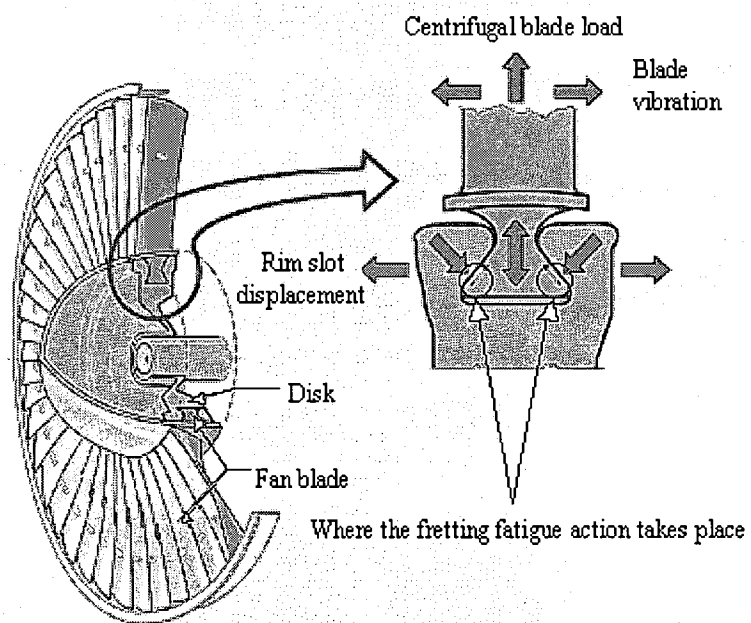


Figure 1.2 Fan and compressor blade dovetail joint [45]

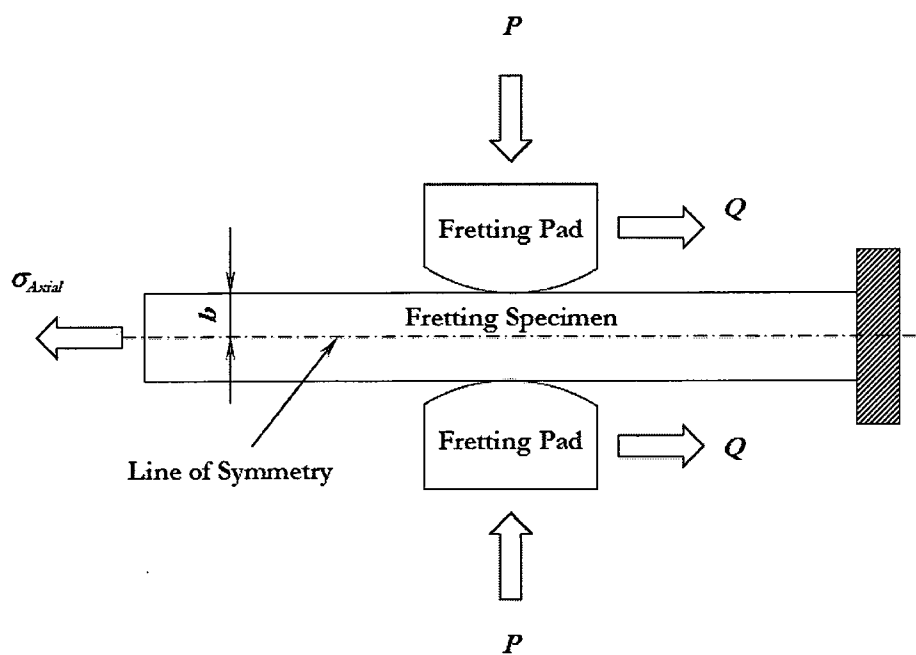


Figure 1.3 Schematic of a fretting model

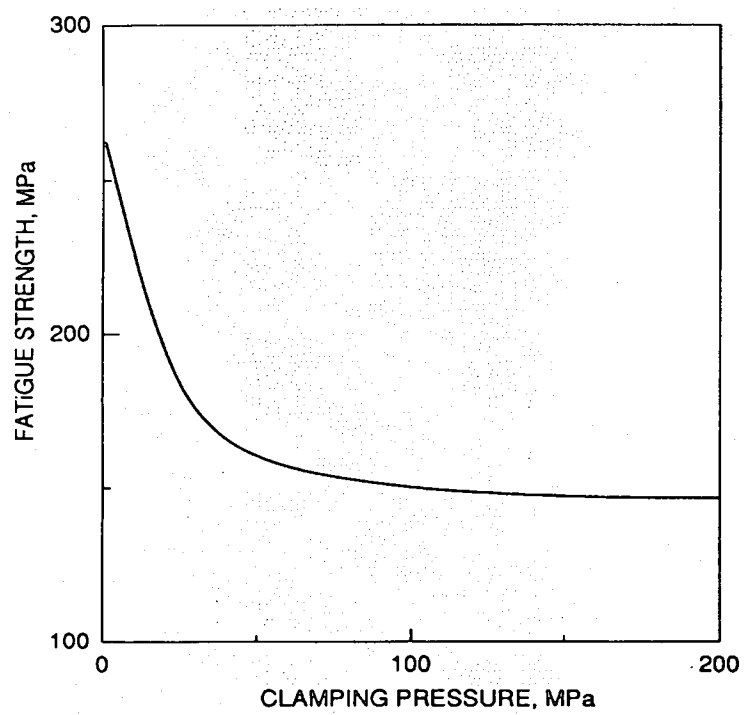


Figure 1.4 Fretting fatigue versus clamping load [8]

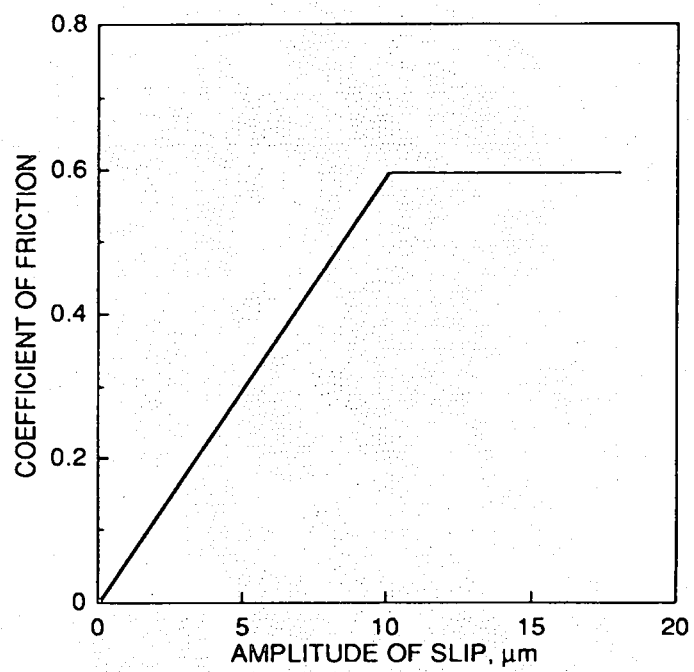


Figure 1.5 Coefficient of friction versus slip amplitude [11]

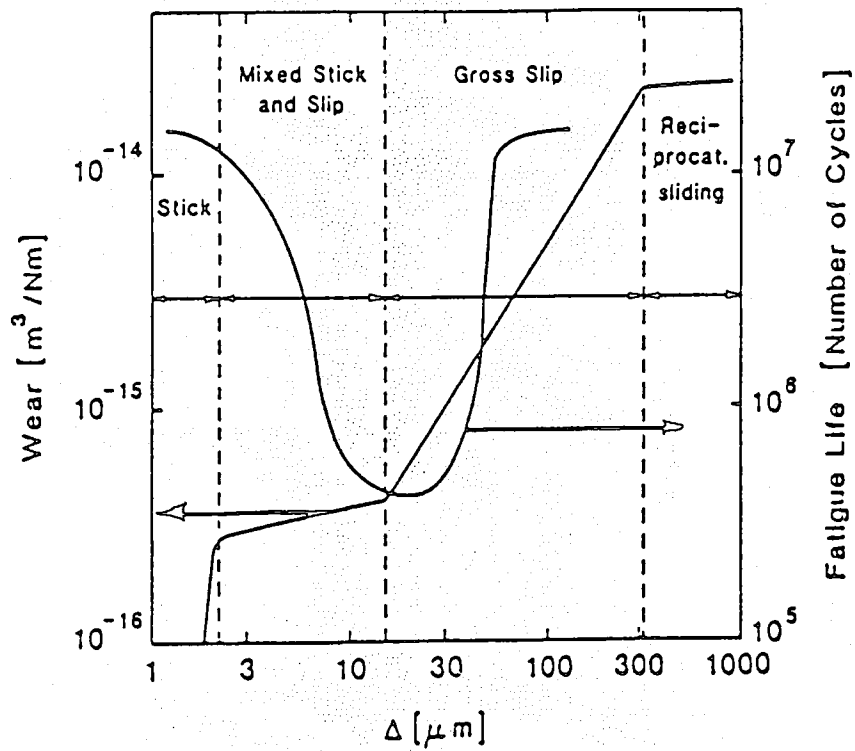


Figure 1.6 Relation between wear and fatigue strength as a function of slip amplitude [14]

CHAPTER II

CONTACT MECHANICS AND CRACK GROWTH ANALYSIS

In this chapter, key aspects of fretting fatigue crack propagation will be discussed, which include the analytical solution for fretting contact, fracture mechanics, and shot-peening.

2.1 Analytical Solution for Fretting Contact

Since fretting involves contact between two bodies, this section presents the fundamentals of contact mechanics related to fretting. Usually, a fretting contact is modeled as a flat specimen, with a thickness of $2b$, sandwiched between two cylindrical or flat pads as shown in Figure 2.1. A constant normal load P , is applied on these pads through the use of lateral springs, and the specimen is loaded by a cyclic axial stress σ , that produces micro-slip between the pad and specimen resulting in a shear load Q , which varies from Q_{min} to Q_{max} (as the axial stress fluctuates between σ_{min} and σ_{max}).

The analytical solution for the fretting contact is summarized by Hills and Nowell [46]. This solution is applicable for cylindrical, spherical, or flat bodies. The primary assumptions in this solution are: (a) the contacting bodies are elastic and isotropic, (b) have very large dimensions in comparison to the contact dimension, and (c) have infinite boundaries as compared to the contact dimensions, commonly referred as a half space. Half space assumption for the specimen is satisfied if its half thickness b , is at least ten times larger than

the contact zone half width a , i.e. $b/a > 10$. Fellows and his colleagues [47] found in their study that finite dimensions, defined by $b/a = 3$, had a significant effect on the contact surface stress in the x -direction σ_{xx} . They found that σ_{xx} could increase by as much as 20% at the contact trailing edge, if the half space assumption is not satisfied, due to the application of the normal and tangential loads. Thus, the violation of the half space assumption would cause a deviation from the analytical solution. Consequently, numerical methods, such as finite element method, are generally used for the evaluation of problems involving fretting contact.

When examining two bodies in contact and assuming that arbitrary points in the contact zone are displaced in the y -direction by $v_1(x) - v_2(x)$, then by using the displacement relationship expressed by Hills and Nowell [46], the following relationship can be developed in the contact region:

$$\frac{1}{A} \frac{\partial h}{\partial x} = \frac{1}{\pi} \int \frac{p(\xi) d\xi}{x - \xi} - \beta q(x) \quad (2.1)$$

where $h(x) = v_1(x) - v_2(x)$ (Figure 2.2), which is the amount of overlap that would take place if the two contacting bodies could penetrate each other. The subscriptions 1 and 2, here, correspond to contact bodies 1 and 2 respectively, p is the pressure in the contact zone, q is the surface shear stress, and a is the contact half width. A and β are materials constants, and they are defined as:

$$A = 2 \left[\frac{1 - \nu_1^2}{E_1} + \frac{1 - \nu_2^2}{E_2} \right] \quad (2.2)$$

$$\beta = \frac{1}{2A} \left[\frac{1 - 2\nu_1}{G_1} - \frac{1 - 2\nu_2}{G_2} \right] \quad (2.3)$$

where E , G , and ν are the modulus of elasticity, modulus of rigidity, and Poisson's ratio for the materials of the bodies in contact (Figure 2.2), respectively. An equation similar to Equation (2.1) can be derived if one assumes a tangential displacement between the contacting bodies as $g(x) = u_1(x) - u_2(x)$. The new equation is as follows:

$$\frac{1}{A} \frac{\partial g}{\partial x} = \frac{1}{\pi} \int \frac{q(\xi) d\xi}{x - \xi} + \beta p(x) \quad (2.4)$$

Since the assumption in this dissertation is that the materials of both of the bodies under contact (the fretting specimen and the pad), are made from the same material (titanium alloy, Ti-6Al-4V), therefore $\beta = 0$, both equations (2.1) and (2.4) can be simplified as follows:

$$\frac{1}{A} \frac{\partial h}{\partial x} = \frac{1}{\pi} \int \frac{p(\xi) d\xi}{x - \xi} \quad |x| \leq a \quad (2.5)$$

$$\frac{1}{A} \frac{\partial g}{\partial x} = \frac{1}{\pi} \int \frac{q(\xi) d\xi}{x - \xi} \quad |x| \leq a \quad (2.6)$$

2.1.1 Hertz Solution

When two elastically similar bodies are brought into contact by a normal load P , a pressure distribution along the contact zone $p(x)$, is produced. The solution of such a pressure distribution is known as Hertz solution. To derive this solution from Equation (2.5), the equation has to be inverted. The inversion of this equation was accomplished by Muskhelishvili and others [48, 49], and is expressed as follows:

$$p(x) = -\frac{w(x)}{A\pi} \int_{-a}^a \frac{h'(\xi) d\xi}{w(\xi)(x - \xi)} + Cw(x) \quad |x| \leq a \quad (2.7)$$

where $w(x)$ is a weight function and C is an integration constant. The values of these two parameters depend on the required behavior of $p(x)$, at the ends points [46]. When the two

bodies in contact are parallel and infinitely long cylinders; the local profile of the contact surface can be idealized as a parabola, which permits $h'(x)$ in Equation (2.7) to be written in a simple form, and the resulting integral to be evaluated analytically. The amount of overlap in freely interpenetrating bodies is defined as:

$$h(x) = \Delta - \frac{1}{2} kx^2 \quad (2.8)$$

$$\Rightarrow h'(x) = -kx \quad (2.9)$$

where Δ is the approach of two remote points and k is the relative radius of curvature, $k = 1/R_1 + 1/R_2$, where R_1 and R_2 are the radii of bodies 1 and 2. Note that in this current study, body 2 is always a flat specimen, which leads to $R_2 = \infty$; i.e. $1/R_2 = 0$. Moreover, for this case, the constant C of Equation (2.7) is zero and the weight function $w(x) = \sqrt{a^2 - x^2}$ [46]. Substitution of $w(x)$ and $h'(x)$ in Equation (2.7) gives:

$$p(x) = -\frac{\sqrt{a^2 - x^2}}{A\pi} \int_{-a}^a \frac{k\xi d\xi}{\sqrt{a^2 - x^2}(\xi - x)} \quad |x| \leq a \quad (2.10)$$

Solving the integral yields:

$$p(x) = -\frac{k}{A} \sqrt{a^2 - x^2} \quad |x| \leq a \quad (2.11)$$

This contact pressure is elliptical, but of limited use until the contact half width a , is determined. This can be achieved by employing a state of equilibrium in the contact zone between the normal load P , and the pressure distribution as follows:

$$P = - \int_{-a}^a p(\xi) d\xi = \frac{\pi k a^2}{2A} \quad (2.12)$$

$$\Rightarrow a = \sqrt{\frac{2AP}{\pi k}} \quad (2.13)$$

Therefore, Equation (2.7) can be written as follows:

$$p(x) = -p_o \sqrt{1 - (x/a)^2} \quad |x| \leq a \quad (2.14)$$

where, p_o is the maximum pressure, which is defined as $p_o = \frac{2P}{\pi a}$.

2.1.2 The Effect of Tangential Load (Mindlin Solution)

Since fretting also involves tangential loading, it is desirable to formulate the analytical solution of two cylindrical bodies in contact where both normal and tangential loads are considered. Mindlin [50] derived such a solution. In general, when two bodies in contact are subjected to both normal and tangential loads, the contact zone ($2a$) is divided into two sub-zones known as stick and slip zones as shown in Figure 2.3.

In the stick zone ($-c, c$), the contact points from both bodies move together; while in the slip zone, such points are free to move independently of each other. This slip zone originates from the interaction of the applied normal load P , and the frictional force Q . For the case of slip ($a > |x| \geq c$) the tractions are related to the friction law, such that:

$$|q(x)| = -fp(x) \quad (2.15)$$

The minus sign, here, is introduced, because a compressive surface stress is assumed negative. Moreover, the shear stress $q(x)$, opposes relative motion of the surfaces giving:

$$\text{sgn}(q(x)) = -\text{sgn}\left(\frac{\partial g}{\partial t}\right) \quad (2.16)$$

where $g = u_1(x) - u_2(x)$ is the relative displacement in the x -direction of the contacting surfaces, and t is the time. The time derivative is introduced to make the problem quasi-static. For the case of no slip ($|x| < c$), a point in the contact zone must experience a situation where shear tractions are lower than or equal to the limiting frictional force, as in:

$$|q(x)| \leq -fp(x) \quad (2.17)$$

In the stick zone, the particles of the two bodies in contact are rigidly adhered to each other and the following relationship applies:

$$u_1(x) - u_2(x) = g(x) = g_o(x) \quad (2.18)$$

where $g_o(x)$ is the value of $g(x)$ when the particles enter the stick zone. The differential form of this equation is:

$$\frac{\partial u_1(x)}{\partial x} - \frac{\partial u_2(x)}{\partial x} = \frac{\partial g(x)}{\partial x} \equiv g'_o(x) \quad (2.19)$$

When a contact contains both regions (stick and slip) in which Equations (2.15-2.17) apply, then the contact is in a state of partial slip. To achieve a solution, the following equation has to be solved:

$$\frac{1}{A} \frac{\partial g}{\partial x} = \frac{1}{\pi} \int_{\text{Contact}} \frac{q(\xi) d\xi}{x - \xi} \quad (2.20)$$

The problem with solving this equation is that the location of the stick or the slip zones is not known prior to testing. One way to resolve this issue is to guess the extent of the slip regime and then determine whether Equations (2.15), (2.17), and (2.19) can be satisfied. For example, if one assumes that there is no slip, i.e. $g_o(x) = 0$, Equations (2.20) becomes:

$$\frac{1}{\pi} \int_{-a}^a \frac{q(\xi) d\xi}{x - \xi} = 0 \quad |x| \leq a \quad (2.21)$$

Similar to the Hertz solution, it can be assumed that the form of the shear stress distribution is [46]:

$$q(x) = \frac{C}{\sqrt{a^2 - x^2}} \quad (2.22)$$

where C can be found by considering equilibrium as $Q = \int_{-a}^a q(x)dx$, which gives $C = Q/\pi$.

By examining Equation (2.22), one can observe that the shear stress, $q(x)$, would approach infinity at $x = \pm a$. As concluded from Hertz solution, the normal pressure, $p(x)$, approaches zero as $x \rightarrow \pm a$, which means that the ratio $q(x)/p(x)$ also approaches infinity at these boundaries. This indicates that an infinite friction coefficient is needed to prevent slip, which is not possible. Therefore, the investigation of the slip zone starts with the assumption that some slip would always occur between $a > |x| \geq c$, which surrounds a central stick zone $|x| < c$. As a result of this hypothesis, shear traction is modeled as a perturbation on the fully-sliding solution so that:

$$q(x) = fp_o \sqrt{1 - (x/a)^2} + q'(x) \quad (2.23)$$

where $q'(x) = 0$ is satisfied in the slip zones. This automatically ensures that one of the conditions of slip, $|q(x)| = -fp(x)$, is fulfilled in the slip zone. It is known that, in the stick zone, there is no relative tangential displacement of the surface particles due to the application of the normal load P , so that $g_o(x) = 0$. Thus within the stick zone, Equation (2.20) gives:

$$\frac{1}{\pi} \int_{-a}^a \frac{q(\xi)d\xi}{x - \xi} = 0 \quad |x| \leq c \quad (2.24)$$

Substituting Equation (2.23) into (2.24), followed by normalization of the integral over $|x| \leq c$ and integration of the sliding term gives:

$$\frac{1}{\pi} \int_{-1}^1 \frac{q'(\eta) d\eta}{\eta - t} = f p_o (c/a) t \quad -1 < t < 1 \quad (2.25)$$

where $\eta = \xi/c$ and $t = x/c$. As in Hertz solution, Equation (2.25) has to be inverted [46]; this yields:

$$q'(x) = -f p_o (c/a) \sqrt{1 - t^2} \quad |t| < 1 \quad (2.26)$$

Then by enforcing tangential equilibrium, the stick zone size, c , can be determined:

$$Q = - \int_{-a}^a q(\xi) d\xi = f p_o a \int_{-1}^1 \sqrt{1 - s^2} ds - f p_o (c^2/a) \int_{-1}^1 \sqrt{1 - s^2} ds \quad (2.27)$$

which yields:

$$Q = \frac{f p_o \pi}{2a} (a^2 - c^2) \quad (2.28)$$

From Hertz solution, $p_o = \frac{2P}{\pi a}$; thus the stick zone will be defined as:

$$c/a = \sqrt{1 - |Q/fP|} \quad (2.29)$$

2.1.3 The Effect of Bulk Tensile Stress (Nowell and Hills Solution)

In addition to the tangential load, typical fretting contact includes a bulk tensile stress in the x -direction. Nowell and Hills [51] developed an analytical solution, which addresses the influence of this type of stress. They found that the bulk stress merely shifts the position of the stick zone by an amount e , which changes the distribution of the shear stress in the contact zone, i.e. slight modifications have to be made to the Mindlin solution [50].

The Nowell and Hills analysis begins with a plane strain assumption, and the corresponding strain induced by the bulk stress is given by:

$$\varepsilon_{xx} = \frac{\sigma(1-\nu^2)}{E} \quad (2.30)$$

Further, they assumed that only one body experiences this bulk stress (body 2 in Figure 2.3, which is the fretting specimen) and that the corresponding displacement gradients in the stick zone are equal to $-\varepsilon_{xx}$, i.e.

$$\frac{\partial g}{\partial x} = \frac{\partial u_1}{\partial x} - \frac{\partial u_2}{\partial x} = -\varepsilon_{xx} = -\frac{\sigma(1-\nu^2)}{E} \quad (2.31)$$

Using Equation (2.20) leads to:

$$\frac{1}{\pi} \int_{\text{Contact}} \frac{q(\xi)d\xi}{x-\xi} = \frac{-\sigma}{4} \quad (2.32)$$

The shifted stick zone extends from $x = e - c$ to $x = e + c$. Following the same procedure as used by Mindlin, the solution yields an equation very similar to Equation (2.25):

$$\int_{-1}^1 \frac{q'(t)dt}{\eta-t} = \frac{fp_o\pi c}{a} \left(\eta + \frac{e}{c} - \frac{d}{c} \right) \quad (2.33)$$

where $\eta = (x-e)/c$, $t = (\xi-e)/c$, and $b = \sigma a / (4fp_o)$. This equation can be solved (by using) the following consistency condition [49]:

$$\int_{-1}^1 \frac{\xi + (e/c) - (b/c)}{\sqrt{1-\xi^2}} d\xi = 0 \quad (2.34)$$

This condition requires that:

$$e = b = \frac{\sigma a}{4fp_o} \quad (2.35)$$

So, the solution for $q'(x)$ can then be written as:

$$q'(x) = -fp_o(c/a) \sqrt{1 - [(x-e)/c]^2} \quad (2.36)$$

The Nowell and Hills solution is satisfactory only when the bulk tension is moderate as compared to the tangential force, because one edge of the stick zone will approach the edge of

contact and a reverse slip takes place if a large amount of bulk stress is applied [46]. The above solution is therefore only valid if $e + c \leq a$, i.e.

$$\frac{\sigma}{fp_o} \leq 4\left(1 - \sqrt{1 - Q/fP}\right) \quad (2.37)$$

2.1.4 Internal Stress Fields

In fretting research, it is important to understand the internal stress fields and the surface displacements. The Muskhelishvili potential [48, 49, 52] is considered the best way to describe these quantities for the plane problems.

The potential ϕ , is a function of position z , which is a complex coordinate ($z = x + iy$). The contact geometry (cylinder on a plane) and the coordinates used are depicted in Figure 2.4. The potential ϕ , is determined by carrying out the following contour integral along the contact line:

$$\phi(z) = \frac{1}{2\pi i} \int_{\text{Contact}} \frac{p(t) - q(t)}{t - z} dt \quad (2.38)$$

where $p(t)$ and $q(t)$ are arbitrary pressure and shear traction distributions. For sliding contacts, where $q(t) = -fp(t)$, Equation (2.38) becomes:

$$\phi(z) = \frac{1 - if}{2\pi i} \int_{\text{Contact}} \frac{p(t)}{t - z} dt \quad (2.39)$$

Once the potential ϕ , is found the stress components are defined by:

$$\sigma_{xx} + \sigma_{yy} = 2(\phi(z) + \bar{\phi}(\bar{z})) \quad (2.40)$$

$$\sigma_{yy} - \sigma_{xx} + 2i\tau_{xy} = 2((\bar{z} - z)\phi'(z) - \bar{\phi}(\bar{z}) - \phi(z)) \quad (2.41)$$

Further operations on the potential ϕ , are needed: $\phi'(z)$ implies differentiation with respect to z , $\bar{\phi}(z)$ implies taking the conjugate of the function which, for potentials defined by Equation (2.39), may be found directly from:

$$\bar{\phi}(z) = -\frac{1+if}{1-if} \phi(z) \quad (2.42)$$

The notation $\bar{\phi}(\bar{z})$ implies taking the conjugate of ϕ and replacing the argument by \bar{z} . Once ϕ is known, the other functions can be derived easily. The displacement fields can then be calculated by employing Hook's Law in conjunction with Equations (2.40) and (2.41) as follows:

$$2G\left(\frac{\partial u}{\partial x}\right) + i\frac{\partial v}{\partial y} = (\bar{z} - z)\bar{\phi}'(\bar{z}) + \phi(\bar{z}) + \kappa\phi(z) \quad (2.43)$$

where $\kappa = 3 - 4\nu$ (in plane strain) and $\kappa = (3 - \nu)/(1 + \nu)$ (in plane stress). The analytical solution for the stress and displacement fields is limited by the half space assumption. For this, finite element analysis is required to solve problems involving fretting contact.

2.1.5 Solution for Flat Pad with Rounded Edges

All the previously discussed solutions are applicable for cylindrical bodies. There has been no progress made in analytical solution development for flat bodies with round edges [19]. For instance, there is no available research to describe the effects of the shift in the stick zone for this type of contact condition. Therefore, numerical methods such as finite element analysis are required to deal with contact configurations involving flat bodies with round edges.

2.2 Fracture Mechanics

Fracture mechanics is a division of mechanics focused on the study of problems involving crack growth. In general, fatigue cracks propagate either from an existing flaw, such as an inclusion or a surface imperfection, or from damage initiated as part of the early phases of fatigue itself. Fretting fatigue falls under the latter category [46]. As discussed in the previous chapter, fretting crack life is divided into two phases: initiation and propagation. The initiation phase usually occurs on a microscopic scale and a precise understanding can be attained only through micro structural analysis. However, once the crack has developed and is larger than several material grain sizes, its propagation can be explained by the fracture mechanics technique [46]. This makes the analysis of crack propagation to appear more tractable than that of initiation. Consequently, much work, either experimental, analytical, or numerical, has been carried out over the years in the area of the fretting fatigue crack propagation [22, 23, 25-35]. In general, the objectives of any crack propagation analysis are to predict the crack propagation path, evaluate the fracture parameters along its path, and ultimately to calculate the rate of crack propagation under the applied loading. In this section, the concepts of fracture mechanics relevant to this analysis will be reviewed.

2.2.1 Concept of Linear Elastic Fracture Mechanics (LEFM)

It is known that a mechanical component may fail due to several causes such as excessive elastic deformation, plastic deformation, fracture, etc. As mentioned earlier, cracks may propagate from an existing flaw. The existence of such flaws causes the component to fail earlier than expected, although the material may still be in the elastic range. This type of failure mainly occurs due to stress risers or stress concentrations at some particular points,

such as holes, corners, contact edges, etc. In 1913, Inglis [53] developed a formula for an elliptical hole in an infinitely large plate that demonstrates the effect of stress concentration.

$$\sigma_A = \sigma \left(1 + \frac{2a}{b} \right) \quad (2.44)$$

where σ_A is the stress at the tip of the elliptical hole, σ is the far field stress, and a and b are the major and minor axes of the elliptical hole, respectively. From Figure 2.5, one can conclude that as $b \rightarrow 0$ or $a \gg b$, the elliptical hole approximates a crack and the stress at the tip becomes singular, i.e. $\sigma_A \rightarrow \infty$. The main idea behind Inglis' formula is to show how the existence of irregularities in a component can considerably reduce its strength causing the component to fail at stress levels below its expected load capacity.

Since no real material can sustain such an infinite stress, yielding is expected to occur in a zone near the crack tip, usually known as the plastic or process zone (Figure 2.6). If this zone is small compared to the other dimensions, such as crack length, distance between crack tip and the closest boundary, etc., a small scale yielding condition is believed to occur. This means that regardless of the nonlinear effects, the elastic field surrounding the process zone governs the stability of the crack. This concept forms the basis of linear elastic fracture mechanics (LEFM).

The ultimate objective of fracture mechanics is to provide ways to determine the safety of a component in the existence of cracks. In LEFM, the effects of the plastic zone are usually neglected. Therefore in the vicinity of the crack tip, where a singular stress field develops, a stability criterion based on stresses is inappropriate. Instead, an energy criterion, originally proposed by Griffith [54], suggested that a condition for instability takes place if the elastic strain energy released when the crack grows by a small amount is equal to the energy

required to create the new crack surfaces. In this criterion, for an infinitely large plate containing a crack of length $2l$, which is perpendicular to an applied uniform tensile stress field as shown in Figure 2.7, the critical applied stress σ_c , that may cause crack propagation is given by [54, 55]:

$$\sigma_c = \sqrt{\frac{2\lambda E'}{\pi l}} \quad (2.45)$$

where λ is the surface energy per unit area and E' is a function of Young's modulus E , and Poisson's ratio ν , defined as follows:

$$E' = E \quad \text{For plane stress} \quad (2.46)$$

$$E' = E/(1 - \nu^2) \quad \text{For plane strain} \quad (2.47)$$

Subsequently, Irwin [56] introduced the critical potential energy release rate G_c to include not only the surface energy, but also the energy due to plastic deformations in the plastic zone. Equation (2.45) can now be restated as [55, 56]:

$$\sigma_c = \sqrt{\frac{G_c E'}{\pi l}} \quad (2.48)$$

The energy based stability criterion is then given by:

$$G = G_c \quad (2.49)$$

where the potential energy release rate G is defined more generally as:

$$G = \frac{\sigma^2 \pi l}{E'} g \quad (2.50)$$

where g is a correction factor due to the geometry and loading of the component. For the original Griffith's problem (Figure 2.7), g is equal to unity. The parameter G_c is a measure of material resistance to crack propagation, usually known as the critical fracture energy.

In an LEFM model, the typical stress distribution, near a crack tip, is given by the following formula [55]:

$$\sigma = \frac{K}{\sqrt{2\pi r}} f(\theta) + \text{negligible terms} \dots \quad (2.51)$$

where r is the radial distance from the crack tip, and θ is the angle with respect to a line parallel to the crack as shown in Figure 2.8. The coefficient K , is the stress intensity factor. It is clear from Equation (2.51) that the stress distribution at the crack tip is invariant with respect to geometry and loading of the component. Thus, the stress intensity factor must include these effects. Therefore one can conclude that the stress intensity factor fully characterizes the stress field in the vicinity of the crack tip and hence can be used as a crack propagation criterion. In this case, the stability criterion is defined as:

$$K = K_C \quad (2.52)$$

where K_C is a material constant, known as the fracture toughness. For the case of the infinite plate shown in Figure 2.7:

$$K = \sigma\sqrt{\pi l} \quad \text{and} \quad \sigma_C = \frac{K_C}{\sqrt{\pi l}} \quad (2.53)$$

By comparing Equations (2.53) and (2.48), it can be found that both measures of toughness are related by:

$$K_C = \sqrt{G_C E'} \quad (2.54)$$

Usually, the stress field in the vicinity of the crack tip is decomposed into three modes of loading: Mode I is the opening or tensile mode, Mode II is the sliding or in-plane shear mode, and Mode III is the tearing or out-of-plane shear mode (see Figure 2.9). In 2D problems, Mode III is not present and thus only the Mode I and Mode II stress intensity

factors are used to express the crack propagation stability. Moreover, in 2D problems, stress intensity factors are considered essential in the analysis of crack propagation along with the mixed-mode crack interaction criteria, which will be discussed in the following section.

Finally, stress intensity factors can be derived in closed-form for a variety of crack geometries, component geometries, and loading conditions. However, for problems involving complex geometries and loading conditions, such as the case of fretting, numerical techniques such as finite element analysis, boundary element analysis, Green's function methods, etc., are usually required.

2.2.2 Mixed-mode Interaction Criteria

The main objective of these criteria is to determine crack stability and predict the path of propagation. Three well-known mixed-mode interaction criteria will be discussed here; (1) the maximum tangential stress, (2) the maximum potential energy release rate, and (3) the minimum strain energy density. The discussion will be limited to their applicability to 2D problems involving components subjected to two modes of loading, Mode I and Mode II. These criteria depend primarily on the stress intensity factors and have shown good agreement with experimental results [24, 57, 58].

2.2.2.1 *The Maximum Tangential Stress Criterion*

Erdogan and Sih [24] proposed this criterion in 1963. This criterion is based on the knowledge of the stress state near the crack tip. It assumes that the crack propagates in the direction that maximizes the tangential stress around the crack tip. This maximization problem is solved analytically yielding the following solution:

$$K_I \sin \theta + K_{II} (3 \cos \theta - 1) = 0 \quad (2.55)$$

where θ is the angle of crack propagation measured from a tangent to the crack path and K_I and K_{II} are the values of the stress intensity factors. This equation yields the following solution for θ .

$$\tan \frac{\theta}{2} = \frac{1}{4} \frac{K_I}{K_{II}} \pm \frac{1}{4} \sqrt{\left[\left(\frac{K_I}{K_{II}} \right)^2 + 8 \right]} \quad (2.56)$$

$$\Rightarrow \quad \theta = 2 \tan^{-1} \left[\frac{K_I \pm \sqrt{K_I^2 + 8K_{II}^2}}{4K_{II}} \right] \quad (2.57)$$

In this criterion, the crack is assumed to be unstable when:

$$K_I \cos^3 \frac{\theta}{2} - \frac{3}{2} K_{II} \sin \theta \cos \frac{\theta}{2} \geq K_{IC} \quad (2.58)$$

where K_{IC} is the fracture toughness.

2.2.2.2 The Maximum Potential Energy Release Rate Criterion

In 1974, Hussain [57] presented this criterion, which assumes that the crack propagates in the direction that maximizes the potential energy release rate. The amount of energy released is evaluated using the elastic solution of a deflected crack, having a main branch and a propagation branch at an arbitrary angle. The energy release rate is obtained as the limit of the energy released at the same time as the propagation branch vanishes, which results in the following expression:

$$G(\theta) = \left(\frac{\kappa + 1}{8\gamma} \right) [K_I^2(\theta) + K_{II}^2(\theta)] \quad (2.59)$$

where γ is the shear modulus, κ is a function of Poisson's ratio ν ; $\kappa=3-4\nu$ in plane strain, and $\kappa=\frac{3-\nu}{1+\nu}$ in plane stress. $G(\theta)$ is the energy release rate per unit length of crack front, θ is the angle of propagation, and $K_I(\theta)$ and $K_{II}(\theta)$ are the stress intensity factors at the tip of the propagation branch, in the limit as it vanishes, which are given by:

$$K_I(\theta) = \left(\frac{4}{3 + \cos^2 \theta} \right) \left(\frac{1 - \theta/\pi}{1 + \theta/\pi} \right)^{\theta/2\pi} \left[K_I \cos \theta + \frac{3}{2} K_{II} \sin \theta \right] \quad (2.60)$$

$$K_{II}(\theta) = \left(\frac{4}{3 + \cos^2 \theta} \right) \left(\frac{1 - \theta/\pi}{1 + \theta/\pi} \right)^{\theta/2\pi} \left[K_{II} \cos \theta - \frac{1}{2} K_I \sin \theta \right] \quad (2.61)$$

K_I and K_{II} , here, are the stress intensity factors at the tip of the main branch in the absence of the propagation branch. The maximization of $G(\theta)$ is solved numerically. For this criterion, the crack propagation is likely to take place when:

$$G(\theta_{\max}) = \left(\frac{\kappa + 1}{8\gamma} \right) K_{IC}^2 \quad (2.62)$$

2.2.2.3 The Minimum Strain Energy Density Criterion

This criterion was introduced by Sih [58] in 1974; and it states that the crack extension occurs in the direction along which the strain energy density possesses a minimum value. The strain energy density, expressed as a function of the propagation angle, is as follows:

$$S(\theta) = a_{11} K_I^2 + 2a_{12} K_I K_{II} + a_{22} K_{II}^2 \quad (2.63)$$

where

$$a_{11} = \frac{1}{16\pi\gamma} [(1 + \cos \theta) + (\kappa - \cos \theta)] \quad (2.64)$$

$$a_{12} = \frac{1}{16\pi\gamma} [2 \cos \theta - (\kappa - 1)] \quad (2.65)$$

$$a_{22} = \frac{1}{16\pi\gamma} [(1 - \cos \theta)(\kappa + 1) + (1 + \cos \theta)(3 \cos \theta - 1)] \quad (2.66)$$

The same numerical procedure used for the maximization of $G(\theta)$ is used for the minimization of $S(\theta)$. Crack propagation is likely to occur when:

$$S(\theta_{\min}) = \left(\frac{\kappa - 1}{8\pi\gamma} \right) K_{IC}^2 \quad (2.67)$$

The maximum tangential stress criterion is considered, computationally, the simplest compared to the other two criteria and has provided adequate results [59]. Moreover, according to Bittencourt *et al.* [60], this criterion along with the other two criteria provides the same numerical results even if the crack orientation is allowed to change in automatic fracture simulation.

2.2.3 Computation of Stress Intensity Factors

The accuracy of the numerical computation of the stress intensity factors is an important factor in the application of LEFM. Several approaches for computing the stress intensity factors can be found in the literature [61-63]; among those are the displacement correlation technique, the J-integral method, and the modified crack closure integral technique. All of these techniques are finite element based, and are applicable for 2D models.

2.2.3.1 The Displacement Correlation Technique

The displacement correlation technique is considered one of the simplest and earliest techniques used to extract stress intensity factors from finite element results. In this technique, the displacements obtained from the finite element analysis at specific locations are correlated with the analytical solutions expressed in terms of the stress intensity factors. Shih *et al.* [61] found that for quarter-point singular elements at the crack tip, the crack opening displacement δ is given by:

$$\delta(r) = (4v_{j-1} - v_{j-2})\sqrt{r/L} = K_I \left(\frac{\kappa+1}{\gamma} \right) \sqrt{r/2\pi} \quad (2.68)$$

where v_{j-1} and v_{j-2} are the relative displacements in y -direction at the $j-1$ and $j-2$ nodes (Figure 2.10), r is a distance from the crack tip along x -axis, L is the element size, and γ is the shear modulus. From Equation (2.68), the Mode I stress-intensity factor can be evaluated by:

$$K_I = \left(\frac{\gamma}{\kappa+1} \right) \sqrt{2\pi/L} (4v_{j-1} - v_{j-2}) \quad (2.69)$$

A similar formula can be derived for Mode II stress intensity factor as follows:

$$K_{II} = \left(\frac{\gamma}{\kappa+1} \right) \sqrt{2\pi/L} (4u_{j-1} - u_{j-2}) \quad (2.70)$$

where u_{j-1} and u_{j-2} are the relative displacements in x -direction at the $j-1$ and $j-2$ nodes. However in order to obtain accurate results using this technique, care must be taken in selecting the correlation points, and usually a highly refined mesh in the vicinity of crack tip is required; i.e. a higher order singular element is needed. However, this technique is not very useful when the mixed-mode conditions are pronounced [62].

2.2.3.2 The J-Integral Method

In 1968, Rice [63] introduced the classic J-integral, which is a path-independent contour integral, to study non-linear elastic materials under small scale yielding. This contour integral is defined as:

$$J_k = \int_{\Gamma} (S n_k - T_i \frac{\partial u_j}{\partial x_k}) d\Gamma \quad (2.71)$$

where $k = 1 \text{ or } 2$, S is the strain energy density, $T_i = \sigma_{ij} n_j$ is the traction vector, Γ is an arbitrary contour around the tip of the crack, and n is the unit vector normal to Γ ; σ , ϵ , and u are the stress, strain, and displacement field, respectively (Figure 2.11).

Dodds and Vargas [64] presented an updated formulation of the J-integral, known as the equivalent domain integral (EDI). In this formulation, the integration along a contour is replaced with an integration over a finite size domain, by employing the divergence theorem. EDI is considered more convenient for finite element analysis, since the routines that perform numerical integration over a finite size domain are always available [65]. For 2D problems, the EDI form of J-integral is written as an area integral [66]:

$$J_k = - \int_A \left[S \frac{\partial q}{\partial x_k} - \sigma_{ij} \frac{\partial u_i}{\partial x_k} \frac{\partial q}{\partial x_j} \right] dA - \int_A \left\{ \frac{\partial S}{\partial x_k} - \frac{\partial}{\partial x_j} \left[\sigma_{ij} \frac{\partial u_i}{\partial x_k} \right] \right\} q dA - \int_{\Gamma} t_i \frac{\partial u_i}{\partial x_k} q ds \quad (2.72)$$

where $k = 1 \text{ or } 2$, S is the strain energy density; q is a continuous weight function allowing the equivalent domain integral to be treated in the finite element formulation; σ_{ij} are the stresses; u_i are the displacements corresponding to local i -axes; t_i is the crack face pressure load; and s is the contour arc length. Usually, a linear function is chosen for q , which assumes a unit value at the crack tip and a null value along the contour. For elastic materials, the second term in Equation (2.72) disappears. The third term also disappears if the crack faces are not loaded, or

if $q = 0$ at its loaded portions. Since a linear-elastic analysis is considered in the current study and no crack face pressure load exists, Equation (2.72) becomes:

$$J_k = - \int_A \left[S \frac{\partial q}{\partial x_k} - \sigma_{ij} \frac{\partial u_i}{\partial x_k} \frac{\partial q}{\partial x_j} \right] dA \quad (2.73)$$

For LEFM problems, Hellen and Blackburn [67] established the relationship between the two components of the J-integral and the Mode I and Mode II stress intensity factors as follows:

$$J_I = \left(\frac{\kappa + 1}{8\gamma} \right) (K_I^2 + K_{II}^2) \quad (2.74)$$

$$J_{II} = \left[\frac{2(\kappa + 1)}{8\gamma} \right] K_I K_{II} \quad (2.75)$$

However, it can be observed that the component J_{II} in Equation (2.75) is path-dependent. This may lead to inaccurate computation of the stress intensity factors. Bui [68] proposed that separating the symmetric and anti-symmetric fields could eliminate this issue. Many researchers subsequently applied Bui's approach [69, 70]. All of these modifications permit the use of the J-integral method for a wide range of linear and nonlinear crack propagation problems. However, like the displacement correlation technique, the *J-Integral* technique shows poor accuracy in the computation of the stress intensity factors when the mixed-mode conditions are pronounced [62].

2.2.3.3 The Modified Crack Closure Integral Method (MCCI)

This method was first proposed by Rybicki and Kanninen [71]. This method computes the energy release rates G_I and G_{II} of two-dimensional crack under mixed-mode loading. It is considered to be a powerful method, since the energy release rates can be

estimated with only one step of analysis. The modified crack-closure method is based on Irwin's crack-closure integral concept, which assumes that the required work to close a crack from $l + \delta l$ to l is the same as that required extending it from l to $l + \delta l$. Based on this assumption, the strain-energy release rates G_I and G_{II} of a mixed-mode condition are obtained by [72]:

$$G_I = \lim_{\delta l \rightarrow 0} \frac{1}{2\delta l} \int_0^{\delta l} \sigma_{yy}(r) v(r) dr \quad (2.76)$$

$$G_{II} = \lim_{\delta l \rightarrow 0} \frac{1}{2\delta l} \int_0^{\delta l} \sigma_{xy}(r) u(r) dr \quad (2.77)$$

where δl is the virtual crack extension; σ_{yy} and σ_{xy} are the normal and shear stress distributions ahead of the crack tip; and $v(r)$ and $u(r)$ are the crack opening and sliding displacements, respectively at a distance r behind the new crack tip. The crack extension δl , and the normal stress distribution ahead of the crack tip are shown in Figure (2.12).

Using LEFM, the following equations can be used to calculate the stress intensity factors from the strain-energy release rates.

$$G_I = \left(\frac{\kappa + 1}{8\gamma} \right) K_I^2 \quad (2.78)$$

$$G_{II} = \left(\frac{\kappa + 1}{8\gamma} \right) K_{II}^2 \quad (2.79)$$

Quarter-point singular elements are placed around the crack tip to capture the singularity of the stress and strain fields. Raju [73, 74] showed that the strain-energy release rates can be expressed in terms of the nodal forces, F_x and F_y , and the nodal relative displacements v and u as:

$$G_I = \frac{1}{2\delta l} [F_{y,j}(t_{11}v_{j-2} + t_{12}v_{j-1}) + F_{y,j+1}(t_{21}v_{j-2} + t_{22}v_{j-1}) + F_{y,j+2}(t_{31}v_{j-2} + t_{32}v_{j-1})] \quad (2.80)$$

$$G_{II} = \frac{1}{2\delta l} [F_{x,j}(t_{11}u_{j-2} + t_{12}u_{j-1}) + F_{x,j+1}(t_{21}u_{j-2} + t_{22}u_{j-1}) + F_{x,j+2}(t_{31}u_{j-2} + t_{32}u_{j-1})] \quad (2.81)$$

where, $t_{11} = 14 - (33\pi/8)$, $t_{12} = -52 + (33\pi/2)$, $t_{21} = -3.5 + (21\pi/16)$, $t_{22} = 17 - (21\pi/4)$, $t_{31} = 8 - (21\pi/8)$, and $t_{32} = -32 + (21\pi/2)$. The accuracy of the MCCI method can be improved further as δ/l approaches 0. The expressions of the strain-energy release rates in Equations (2.80) and (2.81) are based on the assumption that the forces computed for both elements above and below the x -axis at location $j+2$ are equal and opposite in direction, which can only be true for pure mode (no mixed-mode), homogeneous problems. Raju [73] further corrected those expressions to accommodate mixed-mode problems. According to Bittencourt [62], the modified crack closure integral technique provides accurate results for the stress intensity factors for all levels of local mesh refinement.

2.2.4 Fatigue Crack Growth

As pointed out earlier, the stress intensity factor fully characterizes the stress field in the vicinity of the crack tip; which means that it can also characterize the crack growth. The prior discussion was about components subjected to monotonic loading. Under certain conditions, stress intensity factor can also characterize the fatigue crack growth [75]. In fatigue, when a crack propagating in a component is subjected to a constant amplitude cyclic stress, a plastic zone is developed at the crack tip. From the LEFM concept, when this plastic zone is sufficiently small such that it is surrounded within an elastic singularity zone, the conditions at the crack tip can be defined by the current value of the stress intensity factor K . Hence, the crack growth rate is characterized by K_{max} and K_{min} , which correspond to the

maximum and the minimum stresses, respectively. It is convenient to express the crack growth rate dl/dN , as in the following form:

$$dl/dN = f(\Delta K, R) \quad (2.82)$$

where $\Delta K = K_{\max} - K_{\min}$ and $R = K_{\min}/K_{\max}$ or $\sigma_{\min}/\sigma_{\max}$, both of these formulas are valid for cases with uniform far field tensile loading as shown in Figure 2.7. In literature [75], a number of expressions, for the function $f(\Delta K, R)$, have been proposed, most of which are empirical. Figure 2.13 is a log-log plot, which illustrates the typical relationship between dl/dN and ΔK in metals [46]. From the plot, it can be noticed that the crack growth rate can be divided into three stages. At intermediate ΔK values (Stage II), crack growth rate curve is linear, but it deviates from the linear trend at high and low ΔK levels. In Stage III, the crack growth rate accelerates as K_{\max} approaches K_C , which is the fracture toughness of the material. At Stage I, dl/dN approaches zero at a threshold ΔK_{Th} .

For the linear portion of the curve, the relationship between crack growth rate dl/dN , and ΔK can be described by the following formula:

$$dl/dN = C(\Delta K)^m \quad (2.83)$$

where C and m are constants that vary with both material and environment. This formula is known as the Paris Law [28] and is only applicable for Stage II of the plot in Figure 2.13. It can be noticed that the crack growth rate depends only on ΔK ; i.e. the crack growth rate is insensitive to the ratio R .

However, it is important to develop a crack growth rate formula that considers all the stages of the $dl/dN - \Delta K$ relationship curve. In addition, the effect of R has to be included,

especially for non-uniform loading problems such as in situations involving fretting fatigue [46]. In such loading conditions, the ratio R changes as the crack grows. Therefore, this ratio will be denoted as R_L (the stress intensity ratio or local stress ratio) to distinguish it from the far field stress ratio R .

A number of different empirical relationships have been developed through the years to account for the effect of the stress intensity ratio R_L [46]. One approach, which was adopted here, calculates an effective stress intensity factor range ΔK_{eff} , as an empirical function of the actual ΔK and R_L . For example, Walker [31] gives this relationship as:

$$\Delta K_{eff} = \Delta K(1 - R_L)^{m-1} \quad (2.84)$$

or in terms of K_{max} ,

$$\Delta K_{eff} = K_{max}(1 - R_L)^m \quad (2.85)$$

where m is a material constant that varies between 0 and 1.

In literature [3, 25, 30, 32], the Walker equation is used with a crack growth rate defined by the following sigmoidal empirical relationship:

$$dl/dN = b \left(\frac{\Delta K_{eff}}{\Delta K_{Th}} \right)^p \left[\ln \left(\frac{\Delta K_{eff}}{\Delta K_{Th}} \right) \right]^q \left[\ln \left(\frac{\Delta K_c}{\Delta K_{eff}} \right) \right]^8 \quad (2.86)$$

where b , q , p , g , ΔK_{Th} , ΔK_c are the material constants. Basically, dl/dN is a function of ΔK_{eff} , which by itself is a function of K_{max} and R_L . Note that K_{max} and R_L correspond only to the values of Mode I stress intensity factors. The Mode II stress intensity factors are not included in this growth model due to their negligible effect on the crack growth life [22, 25]. Equation (2.86) is a curve fit of a $dl/dN - \Delta K_{eff}$ data produced in a study described in details in Ref. [30].

Based on this equation, the unit for the crack growth rate is mm/cycle. The values of the various constants for Ti-6Al-4V at 70° F are as follows [30]:

$$\Delta K_{Th}^{LC} (\text{MPa mm}^{1/2}) = 133 \quad b = 3.5 \times 10^{-7} \quad q = 0.235 \quad m (R_L > 0) = 0.72$$

$$\Delta K_C (\text{MPa mm}^{1/2}) = 2083 \quad p = 3.71 \quad g = -0.0066 \quad m (R_L < 0) = 0.275$$

From Equation (2.86), ΔK_{eff} is considered as the crack growth driving parameter. K_{min} is implicit in R_L and is allowed to take negative values [3, 25, 30, 32, 76]. The Walker equation along with Equation (2.86) is known as the Walker model for local stress ratio effects [30]. According to Haritos *et al.* [32], this crack growth model is considered to be one of the two best available models proposed for predicting crack growth rates in aircraft engine materials under typical operating conditions.

To calculate the number of cycles required to propagate a crack from an initial length l_i to a final length l_f , the following formula is used:

$$N = \int_{l_i}^{l_f} \frac{dl}{f(K_{max}, R_L)} \quad (2.87)$$

In this dissertation, the crack propagation life was numerically integrated stepwise by choosing a small Δl and then calculating the corresponding ΔN from the current ΔK_{eff} and dl/dN , as defined by the following formula:

$$N = 0.5 \sum_{i=1}^f \Delta l \times \left[f^{-1}(K_{max(i+1)}, R_{L(i+1)}) + f^{-1}(K_{max(i)}, R_{L(i)}) \right] \quad (2.88)$$

Here, Δl was chosen to be in the range of 0.002 to 0.005 mm as recommended by Shkarayev and Mall [25], because the crack growth results with $\Delta l = 0.005$ mm closely matched with those computed with $\Delta l = 0.002$ mm.

2.2.4.1 Long Crack Threshold Growth Criterion

This criterion is based on the comparison between the applied ΔK_{eff} and the material resistance to the crack growth (ΔK_{Th}^{LC}), which is known as the long crack threshold. This criterion states that crack growth can take place when:

$$\Delta K_{eff} \geq \Delta K_{Th}^{LC} \quad (2.89)$$

According to some experimental studies [30, 33], the long crack threshold (ΔK_{Th}^{LC}) is found to be a function of the ratio R_L . By curve fitting experimental data, those studies found that the long crack threshold varies linearly with R_L as described by the following equation:

$$\Delta K_{Th}^{LC} = 4.366 - 2.424R_L \quad (2.90)$$

This relationship provides a good engineering method for estimating the threshold behavior over a wide range of R_L .

2.2.4.2 Short Crack Threshold Growth Criterion

Under some conditions, small cracks can grow at nominal threshold values that are lower than the traditional long crack threshold ΔK_{Th}^{LC} . In fact, this violation of the threshold occurs every time an originally uncracked smooth specimen breaks under constant amplitude loading. The crack that causes specimen failure must, at some early point in its life, have been too small, i.e. $l \rightarrow 0$, such that the nominal applied ΔK_{eff} was less than the nominal threshold, ΔK_{Th}^{LC} . The relationship between the smooth specimen and fracture mechanics behavior is addressed by the Kitagawa [34] diagram shown in Figure 2.14. This diagram integrates the long crack threshold ΔK_{Th}^{LC} , represented by the inclined line, with the traditional smooth

specimen endurance limit σ_o represented by the horizontal line. The region on the Kitagawa diagram above either the horizontal endurance limit line or the sloping threshold line is “unsafe” in that crack growth is predicted to occur. The region below both lines is “safe” in that no crack growth is expected. The intersection of the two lines, defined as l_o or the short crack parameter, is given by the equation [33]:

$$l_o = \frac{1}{\pi} \left(\frac{K_{Th}^{eff}}{Y\sigma_e} \right)^2 \quad (2.91)$$

where, according to Nicholas *et al.* [33] K_{Th}^{eff} is the effective long crack threshold, corrected for R_L through the following equation:

$$K_{Th}^{eff} = \frac{4.366 - 2.424R_L}{1 - R_L} \quad (2.92)$$

while σ_e is the endurance limit also corrected for R_L through the following equations:

$$\sigma_e = \frac{\sigma_o}{(1 - R_L)} \sqrt{\frac{(1 - R_L)^2}{1 - R_L^2}} \quad R_L > 0 \quad (2.93)$$

$$\sigma_e = \frac{\sigma_o}{(1 - R_L)} \sqrt{\frac{(1 - R_L)^2}{1 + R_L^2}} \quad R_L < 0 \quad (2.94)$$

where σ_o is a material constant and its value for Ti-6Al-4V is 569 MPa [33], $Y = 1.12$ is the geometry factor for a through the edge crack [25, 30]. The short crack parameter l_o , is considered as a transition point between the short crack and the long crack behaviors.

As an interpretation of the Kitagawa diagram, one can conclude that cracks smaller than l_o are able to grow at stress intensity factors that are less than the long crack threshold. Thus for cracks with lengths of this order, El Haddad, Tanaka, and others [77, 78] have

proposed that the fracture mechanics threshold is dependent on crack size according to the following relationship [33]:

$$\Delta K^{SC}_{Th} = \Delta K^{LC}_{Th} \sqrt{\frac{l}{l + l_o}} \quad (2.95)$$

This equation can be expressed in terms of a threshold stress as follows [33]:

$$\sigma^{SC}_{Th} = \frac{K^{eff}_{Th}}{Y \sqrt{\pi(l + l_o)}} \quad (2.96)$$

This formula represents the dashed smooth curve that is asymptotic to the endurance limit and the long crack threshold lines in the two extremes (Figure 2.14). Furthermore, Figure 2.15 demonstrates the effect of short crack on the fracture mechanics threshold as defined by Equation (2.95). All of El Haddad's formulas have been confirmed experimentally in the literature for a number of materials, including the titanium alloy Ti-6Al-4V [79, 80].

2.3 Shot-Peening and Its Effect on Crack Growth Behavior

Shot-peening is one of the most popular cold working procedures, which is used to improve the fatigue strength and the fatigue life of mechanical components. It is widely used in machine components, particularly those found in aeronautical and automotive vehicles [44]. Shot-peening involves bombarding the surface of the component with small, hard, steel balls as shown in Figure 2.16. This bombardment causes biaxial yielding in compression under each point of impact; hence a biaxial compressive residual stress occurs on the component surface due to the elastic recovery of the unyielded material beneath (Figure 2.17). Shot-peening changes the physical and the mechanical properties of the material. It introduces a residual compressive stress on and near the component surface with a changing profile within its

depth, and a compensatory residual tensile stress within the rest of the component along its thickness (Figure 2.18). In addition, shot-peening changes the surface roughness and hardness of the component, thereby potentially changing the coefficient of friction, and work hardening of the component material near the surface. Furthermore, shot-peening causes distortion of the grains near the surface, which reduces the propensity for crack propagation [81]. The scale of all of these modifications might vary when the severity of shot-peening changes. If shot-peening is too severe then there may be no beneficial effects from it. Instead, it may result in brittle material with higher notch sensitivity.

In general, the benefits from shot-peening are contained within the compressive zone of the residual stress profile. This zone tends to prevent or suppress the initiation and propagation of fatigue cracks by canceling out the effects of tensile stresses up to a particular level. Inside this compressive zone, any pre-existing cracks will be closed and arrested. Furthermore, the effect of shot-peening on the fatigue strength and life is more pronounced when the loading is not too severe [25].

During the operating cycles of shot-peened components, the residual stresses induced by shot-peening start to relax. This relaxation is found to increase with higher temperatures [41]. According to Sabelkin *et al.* [44], the amount of such relaxation cannot be precisely known [44]. Namjoshi among others [41, 44, 81] did not find any stress relaxation, and cracks occurred inside the material, whereas for unpeened specimens, the cracks occur on the surface. They found that the initiation site of these in-depth cracks is at a location where the compensatory tensile stress is at its maximum value.

In shot-peened components, the residual stress profile can be experimentally measured. This is commonly done by using X-Ray diffraction technique. However, the tensile

portion of the residual stress profile cannot be fully measured by X-Ray diffraction because the X-rays cannot penetrate the material at large depths, therefore, it is not known exactly. The amounts of the compressive and tensile stresses have to be equal within the component thickness, so that equilibrium within this component can be maintained. Based on this condition, some studies have assumed the compensatory tensile stress full profile, and some have developed mathematical procedures to calculate it [41, 81]. In their study, Namjoshi and his co-workers [41] found that a compressive stress in the range of 675 to 800 MPa was developed up to a depth of about 75 μm , after which it gradually decreased to zero at a depth Y_o . As equilibrium of internal forces has to be maintained, a compensating tensile stress is generated at depths below Y_o . Although, the distribution of such stress was not experimentally determined, some of its characteristics are known. For instance, the tensile stress is zero at Y_o and at the center of the specimen. To ensure the continuity of the stress, the slopes of the tensile and compressive stress portions of the residual stress profile must be equal. Finally, the areas under both stress portions have to be the same for equilibrium. Mathematically, these conditions are given as:

$$[\sigma_t(y)]_{y=Y_o} = 0 \quad (2.97)$$

$$[\sigma_t(y)]_{y=b} = 0 \quad (2.98)$$

$$\left(\frac{d\sigma_c}{dy} \right)_{y=Y_o} = \left(\frac{d\sigma_t}{dy} \right)_{y=Y_o} \quad (2.99)$$

$$\int_0^{Y_o} \sigma_c(y) dy = \int_{Y_o}^b \sigma_t(y) dy \quad (2.100)$$

where $\sigma_c(y)$ and $\sigma_t(y)$ are the compressive and tensile residual stresses in the specimen as a function of depth (y), respectively. b is the specimen half thickness. A stress distribution that

satisfies all the above conditions was obtained in the form of a serpent curve. Thus, the compensatory tensile stress can be expressed as:

$$\sigma_t(y) = \frac{pq(M+r)}{(M+r)^2 + p^2} - s; \quad b > y > Y_o \quad (2.101)$$

where $M = y - Y_o$ and p , q , r , and s are the curve-fitting constants. The dotted line in Figure 2.18 shows a compensatory tensile stress calculated by Equation (2.101).

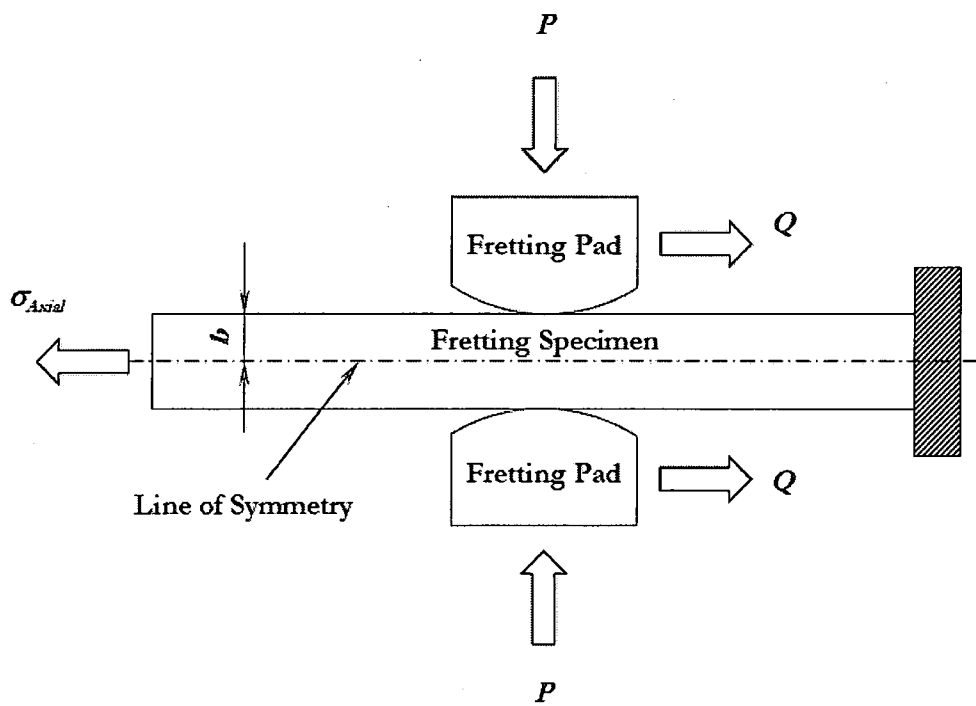


Figure 2.1 Schematic of a fretting model

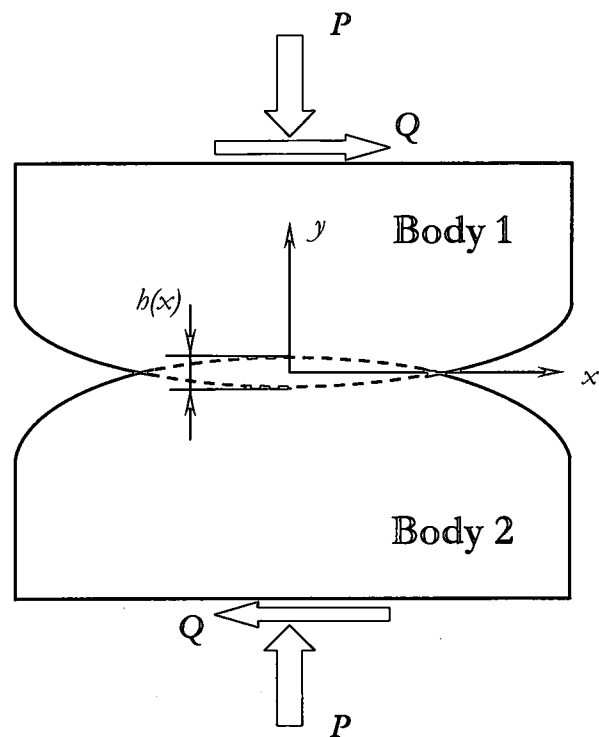


Figure 2.2 Two curved bodies under contact subjected to normal load P , and shear load Q

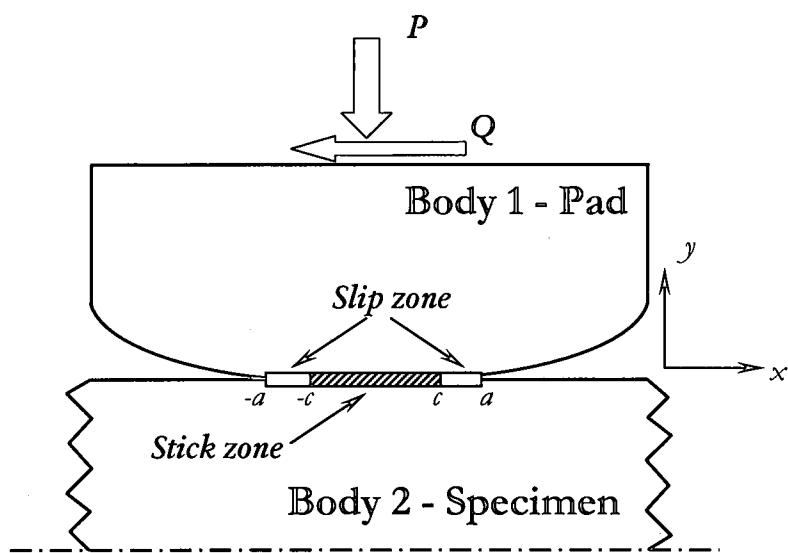


Figure 2.3 Schematic of the stick/slip zones of two bodies under contact

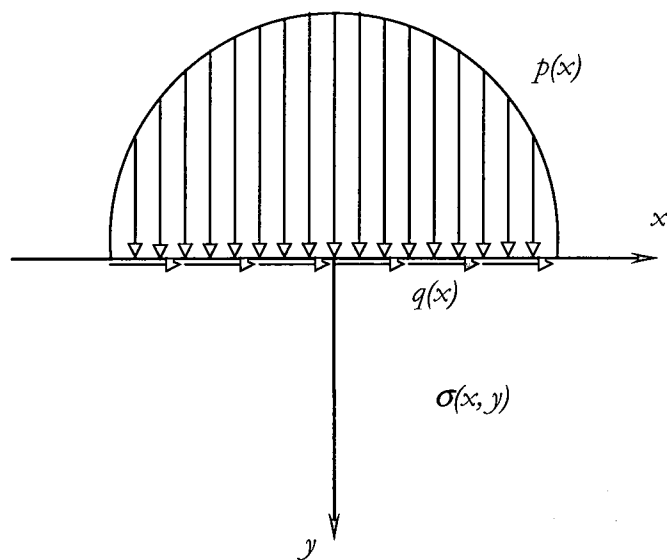


Figure 2.4 Half plane loaded by normal and shear tractions applied on the contact surface

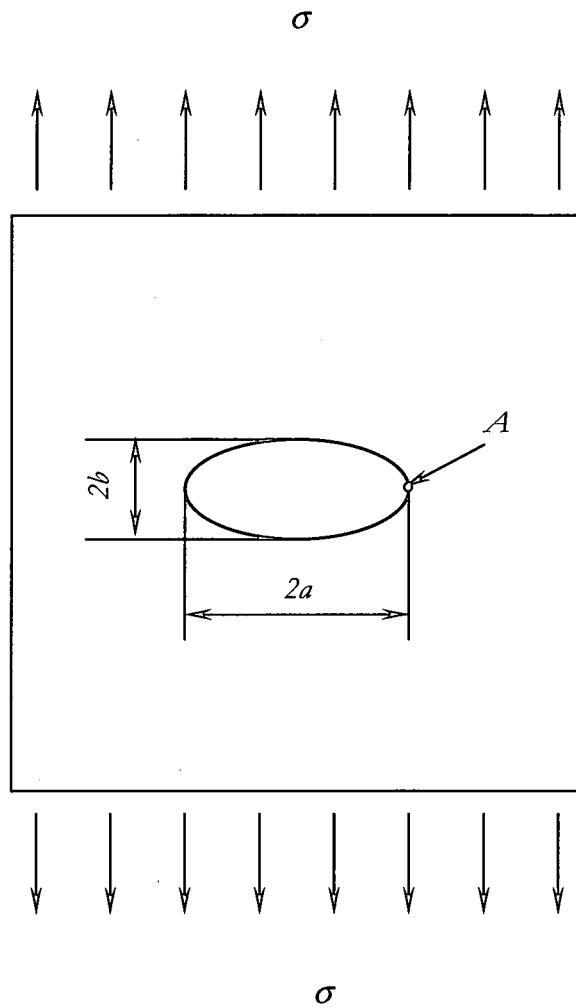


Figure 2.5 Model of an elliptical hole in an infinite flat plate

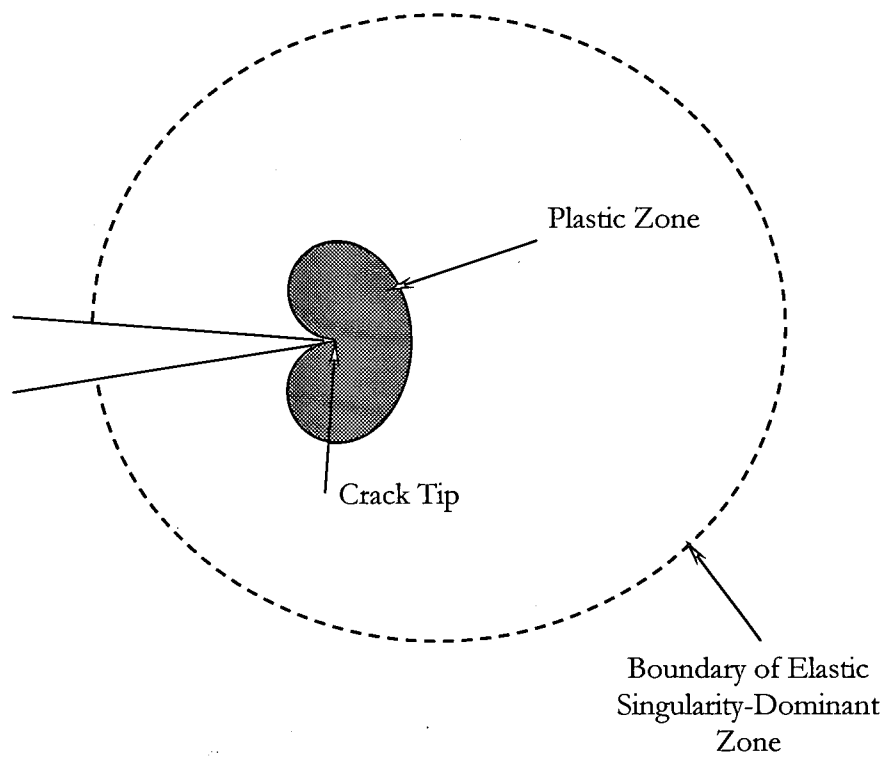


Figure 2.6 Schematic of the plastic zone around the crack tip

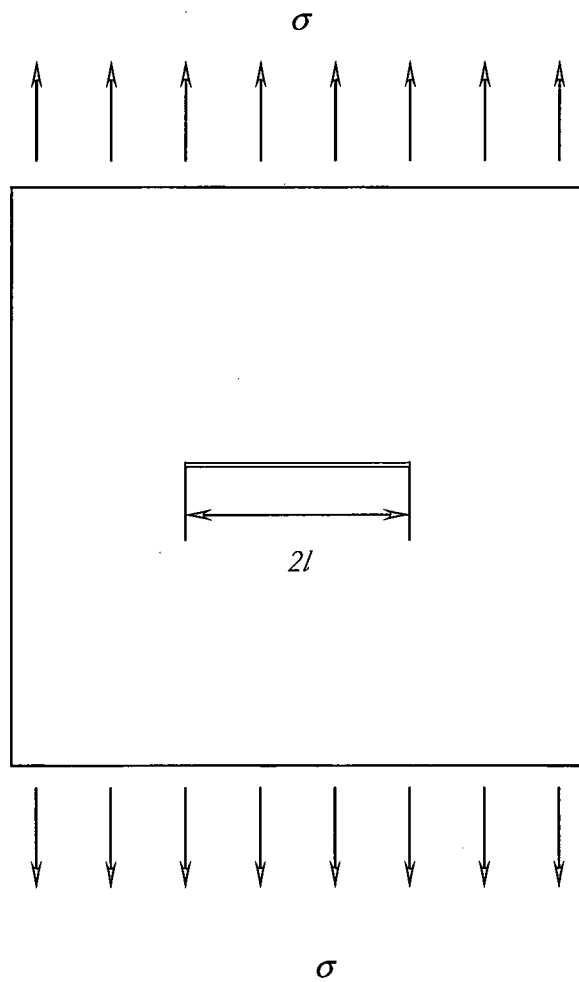


Figure 2.7 A center crack in an infinite flat plate

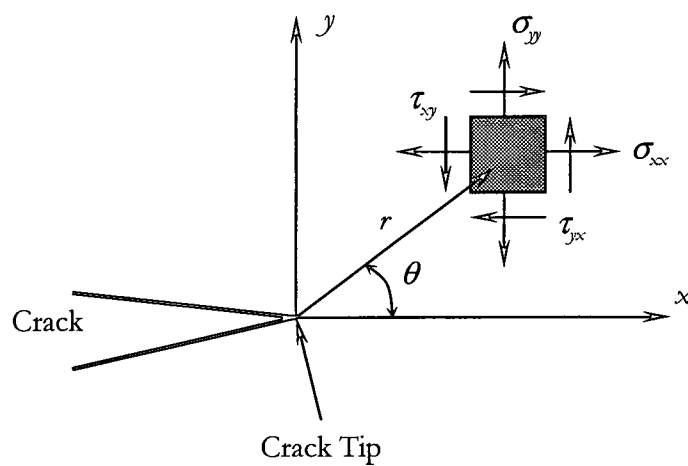


Figure 2.8 Definition of the coordinate axis ahead of the crack tip

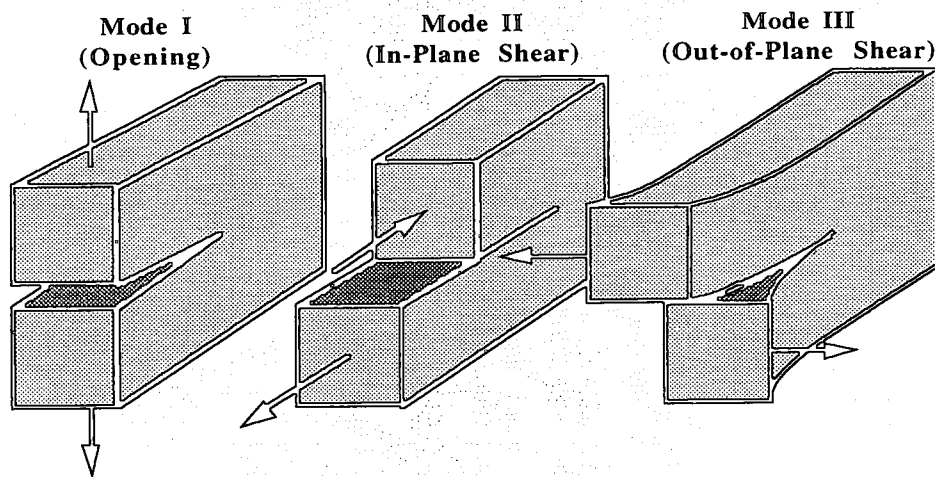


Figure 2.9 Crack opening modes

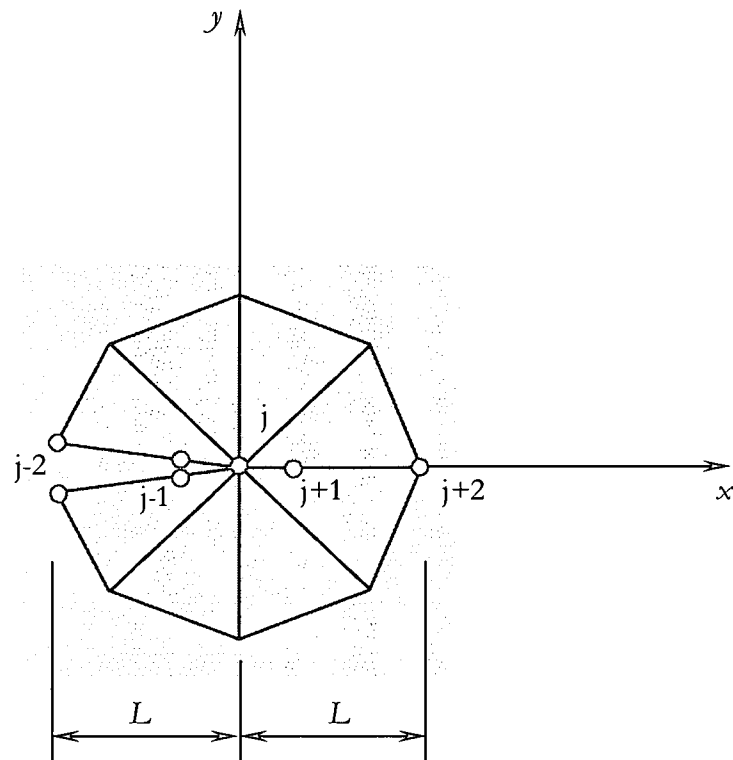


Figure 2.10 Quarter-point elements at the crack tip

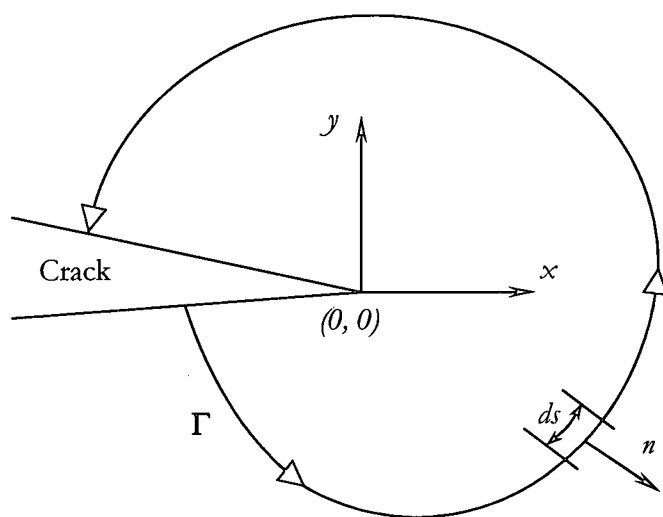


Figure 2.11 A schematic of the *J-Integral* contour

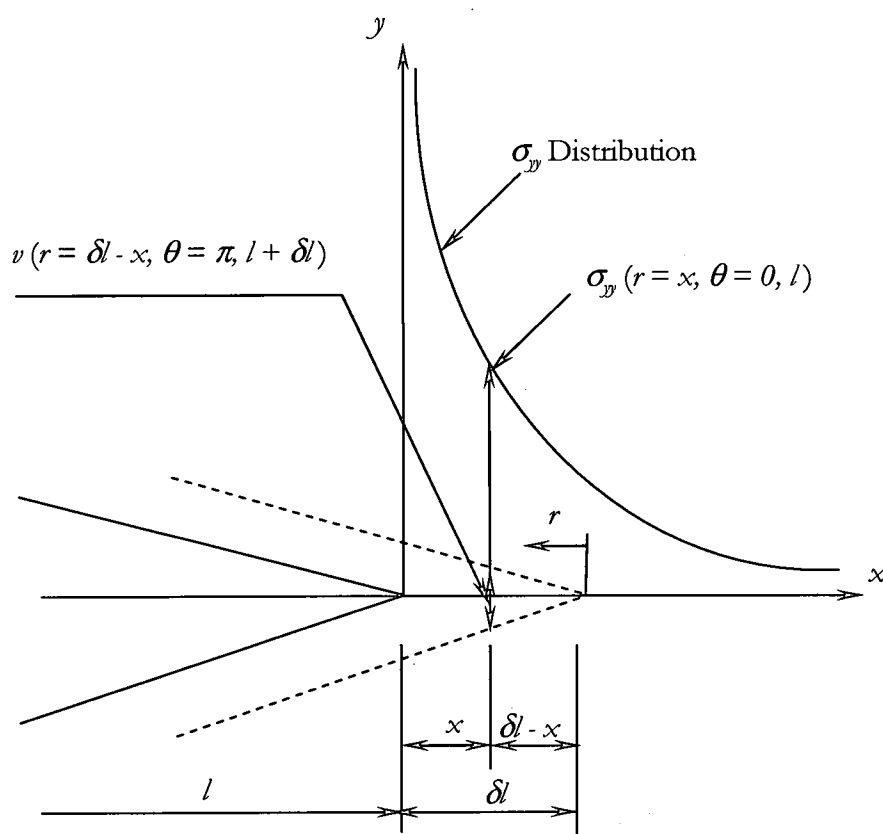


Figure 2.12 Analytical crack-closure integral method

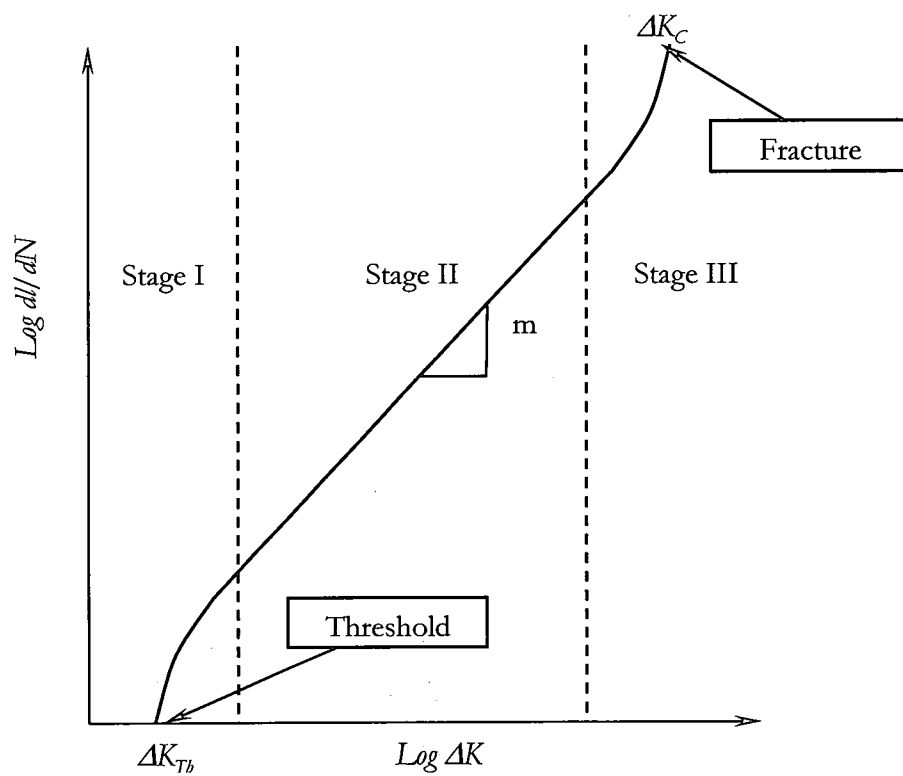


Figure 2.13 Behavior of fatigue crack growth in metals

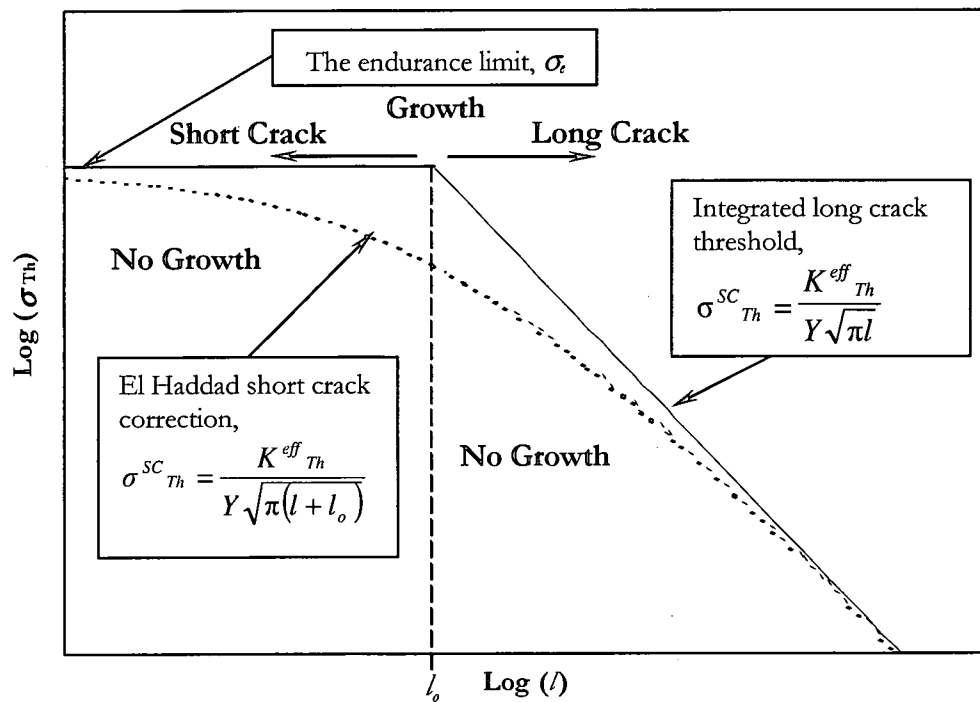


Figure 2.14 Schematic of a Kitagawa diagram

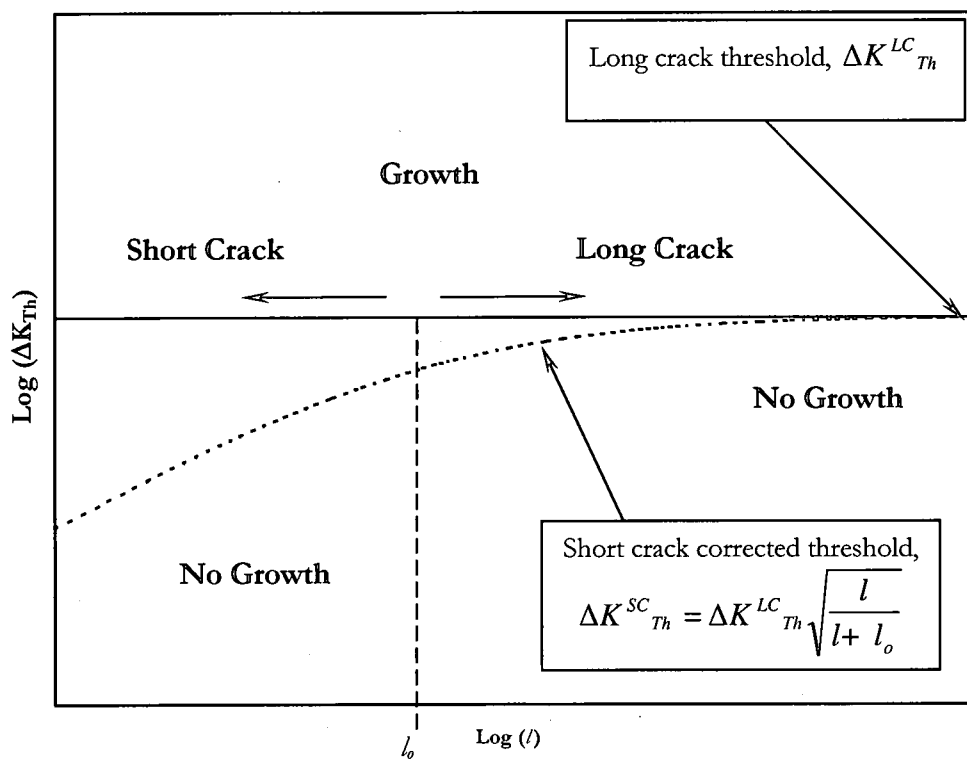


Figure 2.15 Short crack effect on the fracture mechanics threshold ΔK_{Th}

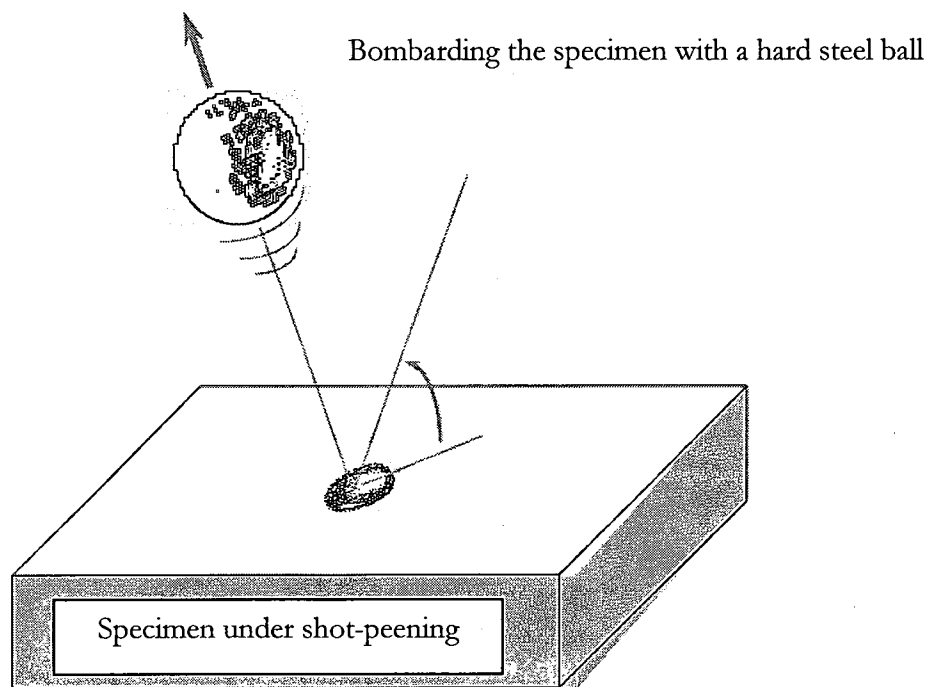
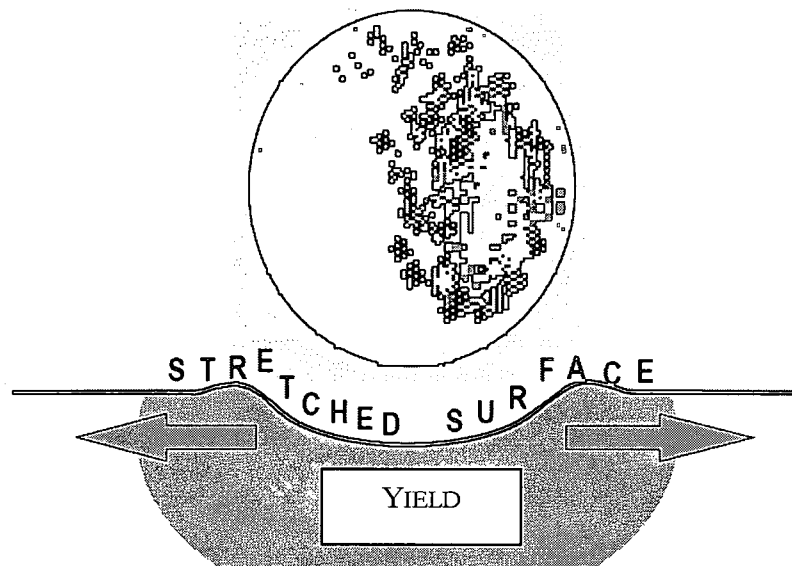


Figure 2.16 Simulation of shot-peening process



The surface is stretched by the balls impact

Compressive stresses attempt
to restore the deformed layer
to its original condition

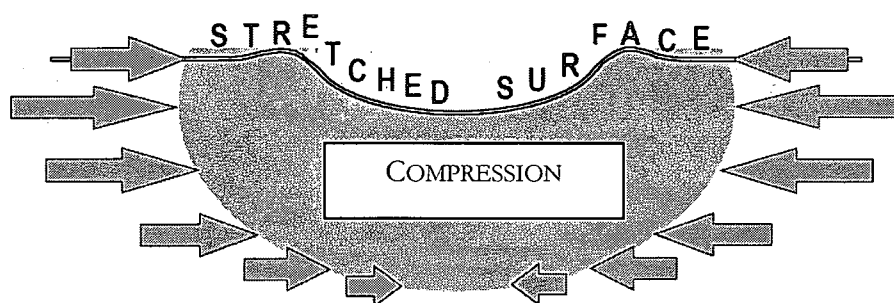


Figure 2.17 The plastic deformation process that occurs in shot-peening

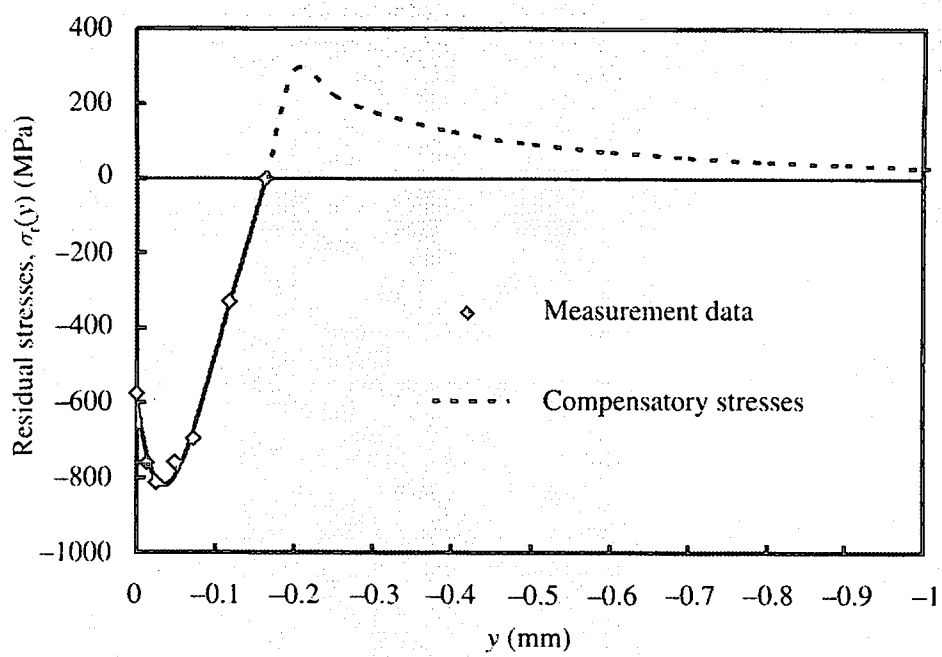


Figure 2.18 A typical residual stress profile [25]

CHAPTER III

PROCEDURE

The purpose of this chapter is to describe the research procedure that was used in this dissertation. The following main topics will be discussed: loading conditions, finite element modeling, and crack propagation analysis in unpeened and shot-peened specimens. A summary of the overall research procedure is presented in the flowchart shown in Figure 3.1.

3.1 Loading Conditions

From the fretting model shown in Figure 1.3, the material of all the fretting specimens and pads used in this study was a titanium alloy Ti-6Al-4V, with a modulus of elasticity of 126 GPa, yield strength of 930 MPa, and Poisson's ratio of 0.32. The average grain size of this material was 10 μm [25]. Two different types of fretting pads were investigated: a cylindrical pad with 50.8 mm radius and a flat pad with rounded edges as shown in Figure 3.2.

The loading conditions used in this dissertation were categorized into three different groups. Each group was chosen to analyze the effects of one or more loading factors on the propagation behavior of fretting fatigue cracks. The first group studied the effect of the axial bulk stress σ . In the second group of loading conditions, a parametric study was performed to investigate the effects of some other loading factors, such as, the normal load P , the coefficient of friction f , and the ratio Q/P . The third and last group of loading conditions studied the effects of shot-peening and its intensities.

3.1.1 Effect of Cyclic Bulk Stress

Here, fretting specimens with 1.9 mm thickness were used with both the cylindrical and flat pads. All the specimens had a 6.35 mm width. In an $S-N$ curve, the cyclic bulk stress is meaningless since it does not incorporate the effect of the bulk stress ratio R . Therefore, most experimental studies [82-85] use a representative value of this bulk stress known as the effective stress σ_{eff} , to account for the effect of the bulk stress ratio R . The effective stress σ_{eff} , is defined by Walker formula [31] as follows:

$$\sigma_{eff} = \sigma_{max} (1-R)^m \quad (3.1)$$

where $R = \sigma_{min} / \sigma_{max}$, $m = 0.45$ as recommended by the references. [82-85].

Three different levels of this stress for each type of pad were investigated – classified as “high”, “medium” and “low”. The other loading factors namely the normal load P , the coefficient of friction f , and the shear force Q , were kept fixed in all the cases. Table 3.1 summarizes all the loading conditions involved in the first part of investigation. From this table, it can be noted that the axial stress and normal load values were the same as those in a previous experimental study involving similar fretting pads [19]: this was done to provide a basis of comparison of the numerical results with the experimental data. The main goal of the comparison was to quantify the crack initiation portion of the fretting fatigue life by subtracting the calculated propagation portion of the life from the total life determined by the experimental study (Table 3.2). The evaluation of the experimental data, which was used in this dissertation, is described in details in APPENDIX A.

3.1.2 Parametric Study

In this group of loading conditions, the effects of three additional fretting loading factors on the propagation life were investigated for both types of fretting pads. These factors were the normal load P , the friction coefficient f , and the ratio Q/fP . Note that the ratio Q/fP defines the size of the stick zone as expressed by Equation (2.29). In all the investigated cases, the intermediate value of the effective stress, which was derived in the cyclic bulk stress analysis, was chosen to be the basis of this parametric study. The base values of the factors under investigation are $P = 1335$ N, $f = 0.5$, and $Q/fP = 0.85$ (Table 3.1). To perform the parametric study, two more values for each factor were used: $P = 2670$ and 4005 N, $f = 0.75$ and 1.0 and $Q/fP = 0.35$ and 0.6 . Table 3.3 summarizes all the loading conditions involved in this parametric study.

3.1.3 Effects of Shot-Peening Intensity

In this last group of loading conditions, fretting specimens with 6.4 mm thickness and 6.35 mm width were used. In addition, only cylindrical pads were used in all the cases. The investigation of this part was based on a previous experimental study which studied the effects of shot-peening intensity on the initiation behavior of fretting fatigue cracks. Table 3.4 summarizes the experimental data from Ref. [44]. In this dissertation, the effects of shot-peening intensity on the propagation behavior of the fretting fatigue cracks were studied. Three levels of shot-peening intensity were investigated; namely 4A, 7A, and 10A with a 100% surface coverage. To study the effect of these intensities, the other loading factors were kept fixed. The following values for cyclic bulk stress, normal load, shear force, and coefficient of friction were used: $\sigma_{max} = 500$ MPa, $\sigma_{min} = 50$ MPa, $P = 1335$ N, $Q_{max} = 1000$ N, $Q_{min} = -1000$ N, and $f = 1.0$.

3.2 Finite Element Modeling

Fretting fatigue experiments usually involve fretting specimens with thicknesses that violate the half space assumption ($b/a < 10$) that must be satisfied for the analytical solution. Therefore finite element analysis is needed to compute the stress, strain, and displacement fields in the fretting pad and specimen. In this dissertation, the finite element analysis simulates the fretting contact partial slip conditions. In addition, the finite element analysis is divided into two parts: global model analysis and sub-model analysis.

3.2.1 Global Model Analysis

Here, the finite element analysis simulates the whole fretting fatigue model, i.e. the pad and the specimen. The commercial code ABAQUS version 6.3 [86] was used to perform the global analysis. For validation, the global finite element solutions of all the cases were compared to the solutions of analytical techniques that assumed a half space existed in each fretting specimen [19]. Figures 3.3 and 3.4 show the global finite element models for fretting models with cylindrical pads and flat pads with rounded edges, respectively. It can be seen that the global finite element model consists of three bodies. The first body is a lateral spring, the second is the fretting pad (cylindrical or flat with rounded edges), and the third is the fretting specimen which is always flat. A distributed normal load P , was applied on the top surface of the fretting pad. The lateral spring represents a rigid body constraint that restricts motion of the pad in the x and y -direction prior to the application of the load steps. The modulus of elasticity of this spring was set to a very small value (i.e. $E = 0.03$ MPa) so that only a small load could be transmitted to it. Cyclic shear force Q , was applied to the left side of the pad as shown in Figures 3.3 and 3.4. Due to the symmetry of the fretting problem, the global model

included only one pad and half of the fretting specimen. The bottom of this specimen was constrained in the y -direction due to symmetry. At the right edge of the specimen, a cyclic axial stress σ , was applied; and at the left end nodes were restricted to move in the x -direction to simulate a fixed support. To maintain the line of action of the normal load P , perpendicular to the specimen surface, a multi-point constraint (MPC) condition was applied to the top surface of the fretting pad so that all of its nodes had the same vertical displacement.

The loads were applied in three steps. In the first step, the normal load P was applied on the pad to establish the contact. In the second step, the maximum shear force Q_{max} and the maximum axial stress σ_{max} were applied to match the experimental maximum cyclic load conditions. Finally, the minimum shear force Q_{min} and the minimum axial stress σ_{min} were applied to match the experimental minimum cyclic load conditions. A Master-Slave algorithm was used to carry out the contact analysis [86].

In the global model, a finer mesh size was used in the vicinity of the contact zone. The mesh size was gradually increased in the regions away from the contact zone as shown in Figures 3.3 and 3.4. It can be noticed from those figures that the refined bands were finer in the regions neighboring the contact zone and coarser in the regions further away (up in the pad and down in the specimen). The purpose of MPC between the layers of different meshes was to ensure equal displacement at the boundaries where the mesh refinement varied. The reason for building the global model with different mesh sizes was to increase the computational efficiency of the finite element analysis. A plane strain four-noded element was used for this study because this type of element was found to be most appropriate for such problems by a number of workers [4, 19, 81]. A sample of a typical ABAQUS input file for the global model is found in APPENDIX B.

For each type of pad, two different mesh sizes were tested - designated as medium (m) and fine (f). The mesh refinement was only applied on the refined bands that are adjacent to the contact zone. The medium mesh size was $24.8 \mu\text{m} \times 24.8 \mu\text{m}$ for the cylindrical pad case, and $56 \mu\text{m} \times 56 \mu\text{m}$ for the flat pad case. The fine mesh size was $12.4 \mu\text{m} \times 12.4 \mu\text{m}$ for the cylindrical pad case and $28 \mu\text{m} \times 28 \mu\text{m}$ for the flat pad case. These large mesh sizes were chosen intentionally to justify the use of the sub-modeling technique. The global models with fine mesh sizes were then compared to the analytical solutions as shown in Figures 3.5 and 3.6. Small deviations were noticed due to the violation of the half space assumption. For the cylindrical pad case, the normalized contact surface stress in the x -direction σ_{xx} , was chosen for the comparison. It can be noticed that the x -coordinate was normalized by dividing it with the contact half width a . However for the flat pad case, the normalized contact surface pressure σ_y , was used for the comparison. This is due to the fact that there is no analytical solution available for σ_{xx} for the flat pad case [19]. Note that the normalization, here, was made by dividing the stress values with the maximum contact pressure p_0 .

3.2.2 Sub-Model Analysis

In fretting, the contact zone is the most critical region. Therefore, an extra mesh refinement is sometimes needed to obtain more accurate stress, strain, and displacement fields, particularly at the locations where the fretting fatigue cracks usually initiate. Consequently, the concept of finite element sub-modeling was used. The ABAQUS sub-modeling feature was chosen specifically to obtain the loading and boundary conditions both at the edges and in the contact region of the sub-model. This facilitated the sub-modeling process for crack

propagation analysis, which was performed by the fracture mechanics codes FRANC2D and FRANC2D/L.

The main purpose of sub-modeling is to study a local portion of a global model with a refined mesh based on interpolation of the solution from an initial, relatively coarser, global model (Figure 3.7). The sub-modeling technique is most useful when it is necessary to obtain an accurate and detailed solution in a local region; and the detailed modeling of that local region has a negligible effect on the overall solution. The response at the boundary of the sub-model is defined by the solution of the global model, and it together with any loads applied to the sub-model determine the solution of the sub-model [86]. Note that the sub-model solution at the boundaries must not be altered significantly by the deferent local modeling. Figure 3.8 shows an example of a possible sub-model for the current fretting fatigue problem. The bold lines represent the boundary nodes of the sub-model, which is known (in ABAQUS) as the driven nodes. In general, sub-modeling analysis consists of (i) running a global analysis and saving the results in the vicinity of the sub-model boundary (ii) constructing the sub-model and defining the total set of driven nodes in it (iii) defining the driven variables in the sub-model analysis by listing the actual nodes and degrees of freedom to be driven in each step of analysis and (iv) running the sub-model analysis using the “driven variables” to obtain the solution. The driven nodes should only contain the surfaces where the sub-model has been cut from the global model, i.e. the boundary of the sub-model (Figure 3.8). However, for the contact problems, like the one shown in Figure 3.8, the surfaces under contact should not be included in the driven nodes.

In this dissertation, the sub-modeling process was used with the global models shown in Figures 3.3 and 3.4. The selected sub-model domains for both the cylindrical and flat pads are shown in Figures 3.9 and 3.10. In these sub-models, the mesh refinement was only applied

on the refined bands that were neighboring the contact zone. To justify the use of sub-modeling technique, a convergence criterion was employed to check if the peak stress produced from the two global models of the two different mesh sizes (discussed in the preceding section) converged or not. The peak stress was considered to converge if [87]:

$$\left| \frac{\sigma_{\max}^f - \sigma_{\max}^m}{\sigma_{\max}^f} \right| \leq \varepsilon_s \quad (3.2)$$

where, σ_{\max} = the peak stress at the trailing edge of the fretting contact, ε_s = the desired error level that leads to the preferred accuracy of the results and is ranked as follows: $\varepsilon_s = 0.01$ or 1% for excellent accuracy, $\varepsilon_s = 0.05$ or 5% for good accuracy and $\varepsilon_s = 0.1$ or 10% for acceptable accuracy [87]. If the error ε_s lies at 1% or less, then sub-modeling is not necessary. However, if the error is more than 10% and a better accuracy is desired, sub-modeling becomes necessary. Here, two different mesh sizes (medium and fine) for both the cylindrical and flat pads were tested. The mesh sizes were $9.3 \mu\text{m} \times 9.3 \mu\text{m}$ and $6.9 \mu\text{m} \times 6.9 \mu\text{m}$ for the cylindrical pad case, and $14 \mu\text{m} \times 14 \mu\text{m}$ and $11.2 \mu\text{m} \times 11.2 \mu\text{m}$ for the flat pad case. Two types of errors: boundary condition error ε_{bc} and the discretization error ε_d had to be checked to ensure that the sub-model displacements at the boundary converged. These errors were defined by the following formulas:

$$\varepsilon_{bc} = \frac{\sigma_{\max}^{fbc} - \sigma_{\max}^{mbc}}{\sigma_{\max}^{fbc}} \quad (3.3)$$

$$\varepsilon_d = \frac{\sigma_{\max}^{fs} - \sigma_{\max}^{ms}}{\sigma_{\max}^{fs}} \quad (3.4)$$

where, σ_{\max}^{fbc} and σ_{\max}^{mbc} = the peak stresses calculated for the fine sub-model mesh using the boundary conditions obtained from the fine and medium global mesh, respectively. σ_{\max}^{fs} and σ_{\max}^{ms} = the peak stresses calculated for the fine and the medium sub-model mesh, respectively, using the boundary conditions obtained from the fine global mesh. The sum of these two errors represents the total error ε , which is:

$$\varepsilon = \varepsilon_{bc} + \varepsilon_d \quad (3.5)$$

From Equation (3.5), two different situations arise: one when ε_{bc} and ε_d are of opposite signs and cancel each other, the other when they are of the same signs and accumulate. To make sure that the magnitude of the total error was less than the desired error level ε_s , the following conditions were used [87]:

$$|\varepsilon_{bc}| < \varepsilon_s, \text{ and } |\varepsilon_d| < \varepsilon_s \quad \text{if } \varepsilon_{bc}\varepsilon_d < 0 \quad (3.6)$$

$$|\varepsilon_{bc}| < \alpha\varepsilon_s, \text{ and } |\varepsilon_d| < (1-\alpha)\varepsilon_s \quad \text{if } \varepsilon_{bc}\varepsilon_d > 0 \quad (3.7)$$

where α varies from 0 to 1; a value of 0.5 for α was considered here [87].

The normalized stress σ_{xx} , (at the contact surface) was chosen as a critical parameter for the comparison of sub-models. From global models with different mesh sizes, the values of the error ε_s , were found to be 3.9% and 4.3% for the cylindrical and flat pads respectively. These values indicated that sub-modeling was needed to achieve even more accurate results. Figures 3.11 and 3.12 show the variation of normalized σ_{xx} , for the sub-models of the cylindrical and the flat pads, around the trailing edge, respectively. Note, that the sub-model with the finer mesh provided the most accurate results. Tables 3.5 and 3.6 summarize all the data obtained from the sub-models analysis. From these tables and Equation (3.6), it may be

noticed that both the boundary conditions and the discretization errors were lower than 1% for the medium and the fine mesh sub-models. This means that both the medium and the fine global mesh sizes provided sub-models with acceptable accuracy. Therefore, the mesh sizes of the global models used in this study were $24.8\ \mu\text{m} \times 24.8\ \mu\text{m}$ and $56\ \mu\text{m} \times 56\ \mu\text{m}$ for the cylindrical and flat pad cases, respectively. For the sub-models of both pads, the mesh sizes of $9.3\ \mu\text{m} \times 9.3\ \mu\text{m}$ and $14\ \mu\text{m} \times 14\ \mu\text{m}$ were used.

3.2.3 Reconstructing the Sub-Model

After constructing the sub-model in ABAQUS, a modification was made to use this sub-model with the fracture mechanics code FRANC2D (or FRANC2D/L) to perform the crack propagation analysis. This included, reconstructing the sub-model with plane strain 8-noded elements since both of the FRANC2D codes could only accept either 8 or 6-noded elements.

The reconstruction of the sub-model was done using the commercial finite element code ANSYS, because it is convenient to translate a model from ANSYS to FRANC2D format through a translator. In the reconstruction of the sub-model, the fretting pad portion was substituted by its equivalent load tractions, which include normal and shear tractions. After translation to FRANC2D format, the reconstructed sub-model was then tested to validate its results with the ABAQUS results. A small deviation of about 3% or less was found, which was considered to be negligible. Figures 3.13 and 3.14 demonstrate the comparison between the FRANC2D and ABAQUS results for both the cylindrical and flat pad sample cases. The variation of the normalized σ_{xx} was the factor in this comparison.

In FRANC2D, an edge crack was inserted in the sub-model to perform the crack growth analysis (Figures 3.15 and 3.16). The sub-model was rectangular in shape and its height was equal to the half-thickness b , of the specimen. The sub-model length C , had to be at least

ten times the maximum crack length to ensure that the boundaries of the sub-model were far enough from the stress concentration produced by the crack [25]. Therefore, sub-model lengths of 5.08 mm and 12.28 mm were used for the cylindrical and flat pads, respectively (Figures 3.9 and 3.10). The displacements in the vertical direction were restrained at the bottom edge of the sub-model due to symmetry of the specimen and loading conditions. The center point was also restrained in the horizontal direction. The action of the fretting pad at the top surface of the sub-model was replaced by the distributed normal and shear loads, $\sigma_p(x, b)$ and $\tau_Q(x, b)$, along the contact line $[-a, a]$. Moreover, the tractions $p_L(-C/2, y)$ and $p_R(C/2, y)$, were applied on the left and right edges of the sub-model, respectively. The values of $\sigma_p(x, b)$, $\tau_Q(x, b)$, $p_L(-C/2, y)$, $p_R(C/2, y)$, were obtained from the results of ABAQUS sub-model. The contact half width a was obtained from the ABAQUS results. The contact half width a is very important since it is considered to be the region where the fretting cracks usually initiate as recommended by many studies [4, 19, 81].

3.3 Crack Propagation Analysis

The crack propagation analysis was performed by using the fracture mechanics codes FRANC2D and FRANC2D/L, which were created by Cornell Fracture Group at Cornell University. If the fretting case included the application of residual stresses induced by shot-peening, then FRANC2D was used, since the capability of inserting the residual stresses was fully implemented in FRANC2D only. Even though both of the codes gave the same results, FRANC2D/L was used for the cases that did not involve the application of the residual stresses, since it was much faster than FRANC2D. Note that the fracture mechanics concepts discussed in chapter II were fully implemented in both of these codes. Since most of the cases

did not involve residual stresses, the name "FRANC2D/L" was used in the description of the numerical nature of these fracture mechanics codes.

Before discussing the crack propagation analysis, the limitations of linear fracture mechanics in the evaluation of crack propagation have to be addressed. The success of this analysis depends on the estimation of the length and orientation of the initial crack [46]. Many studies suggested that the assumed initial crack length should be greater than the material grain size [30, 46, 88]. Due to this reason, the initial crack length, in this study, was chosen to be at least twice the grain size.

In FRANC2D/L, a crack is represented by a curvilinear path, consisting of, J , straight segments, as shown in Figure 3.17. In the first step, an initial crack of length, l_1 , with a slope, θ_1 , from y -axis was introduced at a point on the trailing edge (Figures 3.17). The location was chosen because many studies suggested that the crack in fretting fatigue initiated somewhere at the trailing edge of the contact zone. For all the cases, the value of the angle $\theta_1 = -45^\circ$. This was based on many experimental studies that showed the initial orientation of fretting cracks is mostly at $\pm 45^\circ$ with $\pm 10^\circ$ [4, 19, 81]. After inserting the initial crack, the numerical analysis was performed with a crack length increment of Δl . In the first step, the incremented crack rotated around the tip of the initial crack located at (x_2, y_2) and made the new crack orientation at a slope of (θ_2) , and so on [25].

In FRANC2D/L, the mesh is modified in each incremental step using the Suhara-Fukuda algorithm [89], which generates a trial mesh of triangulated elements (Figure 3.18), and a new crack geometry is represented at each incremental step to reflect the current crack configuration. FRANC2D/L uses the same three mixed-mode interaction criteria, which were discussed in chapter II. Those criteria are the maximum tangential stress criterion, the

maximum potential energy release rate criterion, and the minimum strain energy density criterion. However, according to the speculations made by Miranda *et al.* and Bittencourt *et al.* [59, 60], the maximum tangential stress criterion [24] was used in this dissertation to determine the crack growth directions. According to the maximum tangential stress criterion, the crack angle at the turning point, i , is found by:

$$\theta_i = \theta_{i-1} + 2 \tan^{-1} \left[\frac{K_{I \max i} - \sqrt{K_{I \max i}^2 + 8K_{II \max i}^2}}{4K_{II \max i}} \right] \quad (3.8)$$

At each crack propagation step i , the values of Mode I and II stress intensity factors were computed and a complete crack path was reconstructed through the total number of propagation steps J , as specified earlier. FRANC2D/L also uses the three techniques for computing the stress intensity factors, which were discussed in chapter II. These techniques are the displacement correlation technique, the J-integral technique, and the modified crack closure integral technique. Based on Bittencourt comments [62], the modified crack closure integral technique [71] was used to calculate the stress intensity factors. The values of these factors corresponding to the maximum and minimum loading conditions of each of the cases were extracted at every propagation step along with their corresponding crack lengths. These values were later used in Walker crack growth model [3, 25, 30, 32] (discussed in chapter II) to determine the crack propagation life. The flowchart shown in Figure 3.19 summarizes all the steps involved in the computation of the propagation life of the fretting fatigue cracks.

3.4 The Procedure Used to Calculate the Tensile Residual Stress

The mathematical procedure used to calculate the compensatory tensile residual stress was discussed in chapter II [41]. This procedure was used to evaluate the tensile portions of the residual stress profiles developed from shot-peening of three different intensities (4A, 7A, and 10A) with 100% surface coverage. The compressive portions of these residual stress profiles were measured completely by the X-Ray diffraction technique (Figure 3.20) [44]. The first step before calculating the compensatory tensile residual stress was to curve-fit the experimental measurements of the compressive part of the residual stress as shown in Figure 3.20. The best fit polynomials of these data are:

For 4A case:

$$\sigma_c = -(1.44\text{E}-06)y^4 - (4.92\text{E}-04)y^3 + (1.75\text{E}-01)y^2 - (5.10\text{E}+00)y - (7.51\text{E}+02) \quad (3.9)$$

For 7A case:

$$\sigma_c = (2.51\text{E}-08)y^5 - (1.22\text{E}-05)y^4 + (1.84\text{E}-03)y^3 - (5.80\text{E}-02)y^2 + (2.39\text{E}-01)y - (8.00\text{E}+02) \quad (3.10)$$

For 10A case:

$$\sigma_c = (6.25\text{E}-10)y^6 - (4.01\text{E}-07)y^5 + (9.71\text{E}-05)y^4 - (1.09\text{E}-02)y^3 + (5.87\text{E}-01)y^2 - (1.15\text{E}+01)y - (7.68\text{E}+02) \quad (3.11)$$

The equation used to calculate the compensatory tensile residual stress was:

$$\sigma_t(y) = \frac{pq(M+r)}{(M+r)^2 + p^2} - s; \quad b > y > Y_o \quad (3.12)$$

where $M = y - Y_o$ and p , q , r , and s are the curve-fitting constants. After applying the whole procedure, the compensatory tensile residual stress of each shot-peening intensity was

determined. Figure 3.21 shows the complete residual stress profiles for all the three cases of shot-peening intensities. The values of the curve-fitting constants for all the cases are summarized in Table 3.7. In addition, Table 3.8 summarizes the values and locations of the maximum compressive and tensile residual stresses.

For all the shot-peening cases, FRANC2D was used since it had the capability of processing the residual stresses. The residual stress fields had to be written in a separate input file with a particular format (APPENDIX C). The information included in this file were the coordinates of a point, the corresponding values of the stress components, and an indicator to tell if this point was located on a boundary or in the inside of the studied model. FRANC2D provided an option of inserting those residual stresses by reading the input file. FRANC2D then mapped those stresses on the original model. Internally, those stresses were converted to equivalent nodal forces through the use of the following expression:

$$F(\sigma_{\text{Res.}}) = - \int B^T \sigma_{\text{Res.}} dV \quad (3.13)$$

where B is the shape-function derivative matrix and $\sigma_{\text{Res.}}$ is the residual stress vector.

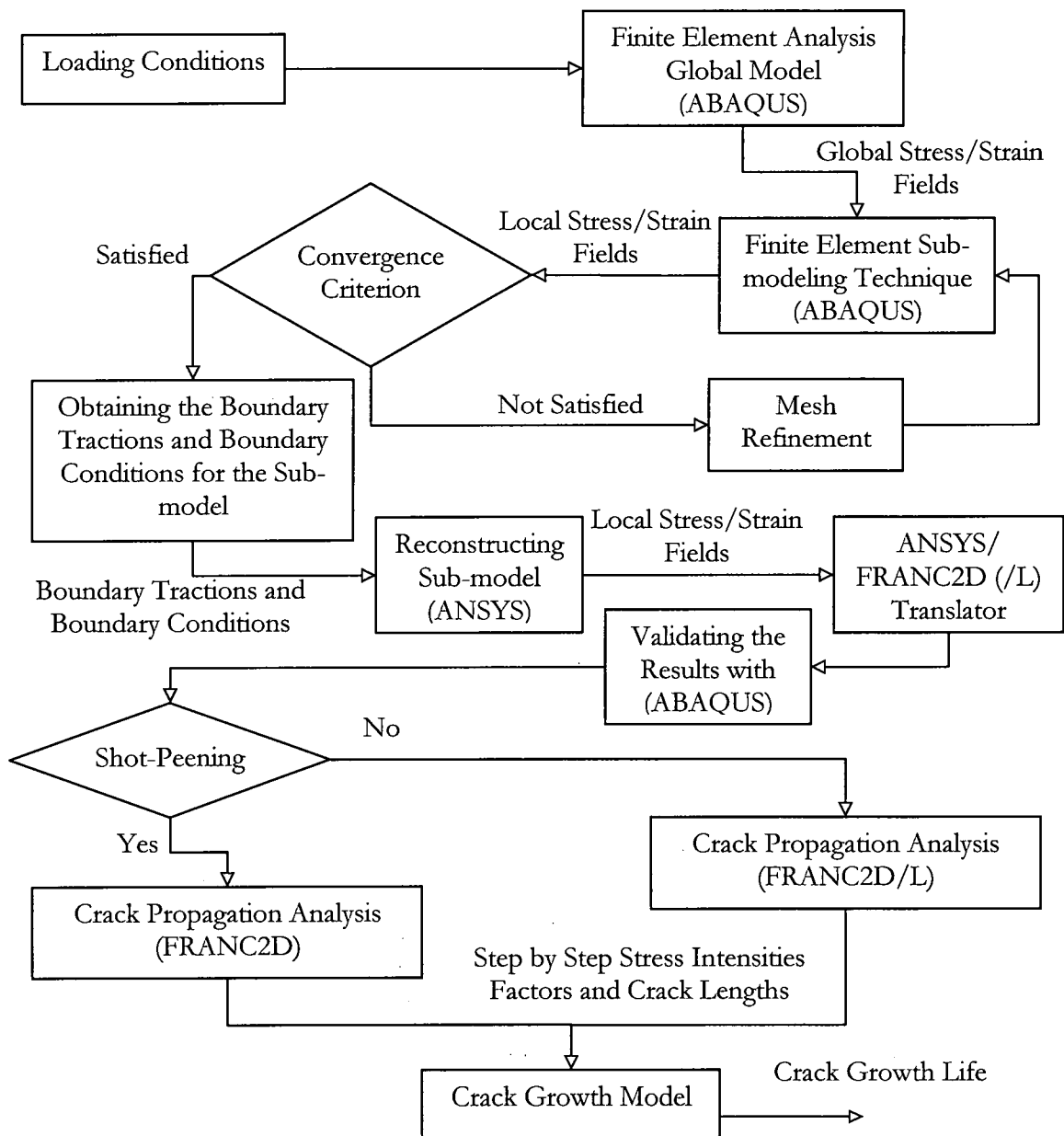
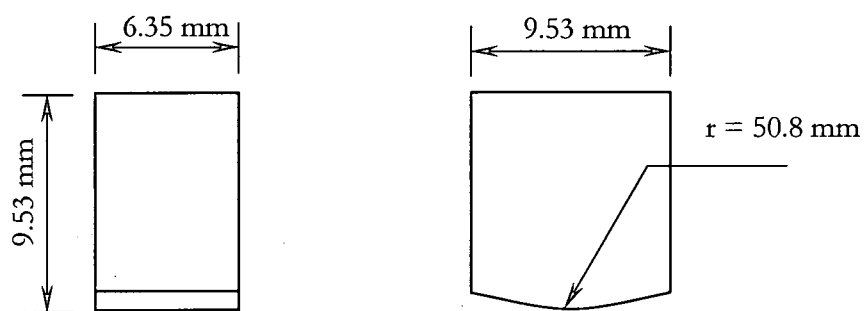
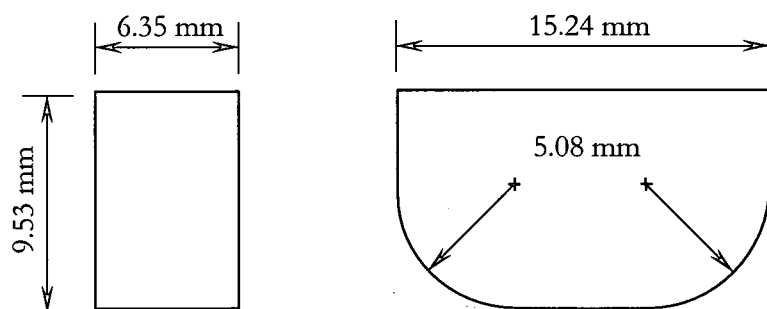


Figure 3.1 Flow chart summarizing the crack propagation analysis



a) Cylindrical Pad



b) Flat Pad

Figure 3.2 Dimensions of the cylindrical and flat pads used in this study

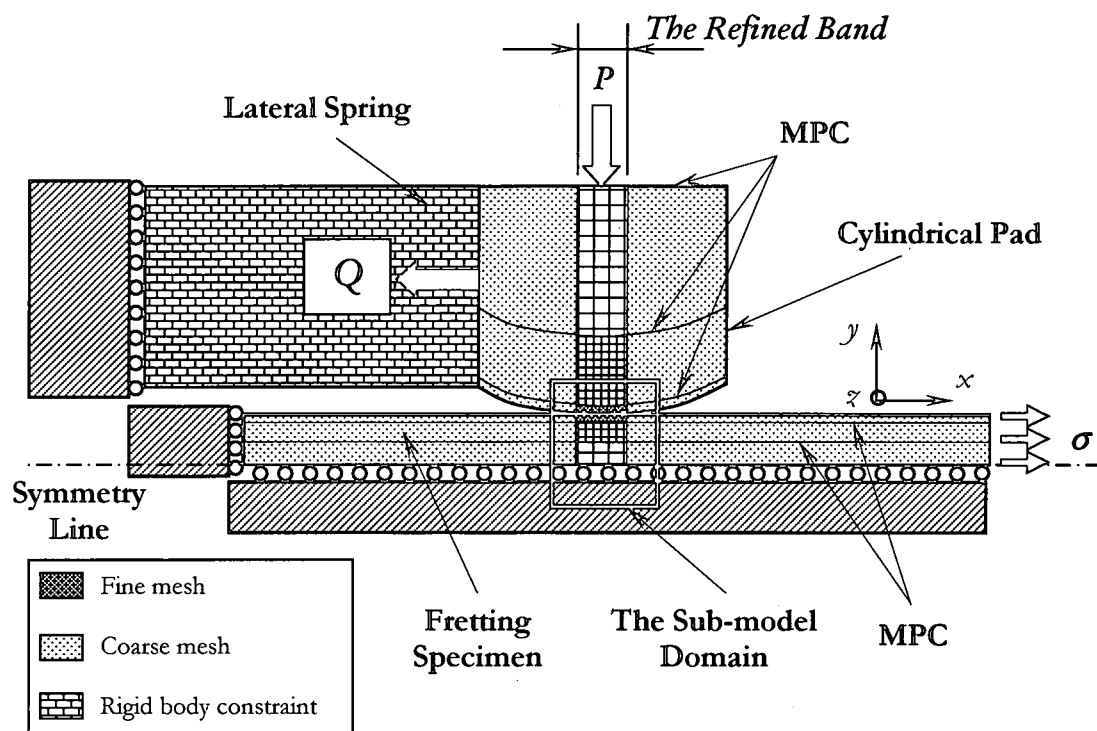


Figure 3.3 Global model of the cylindrical pad case

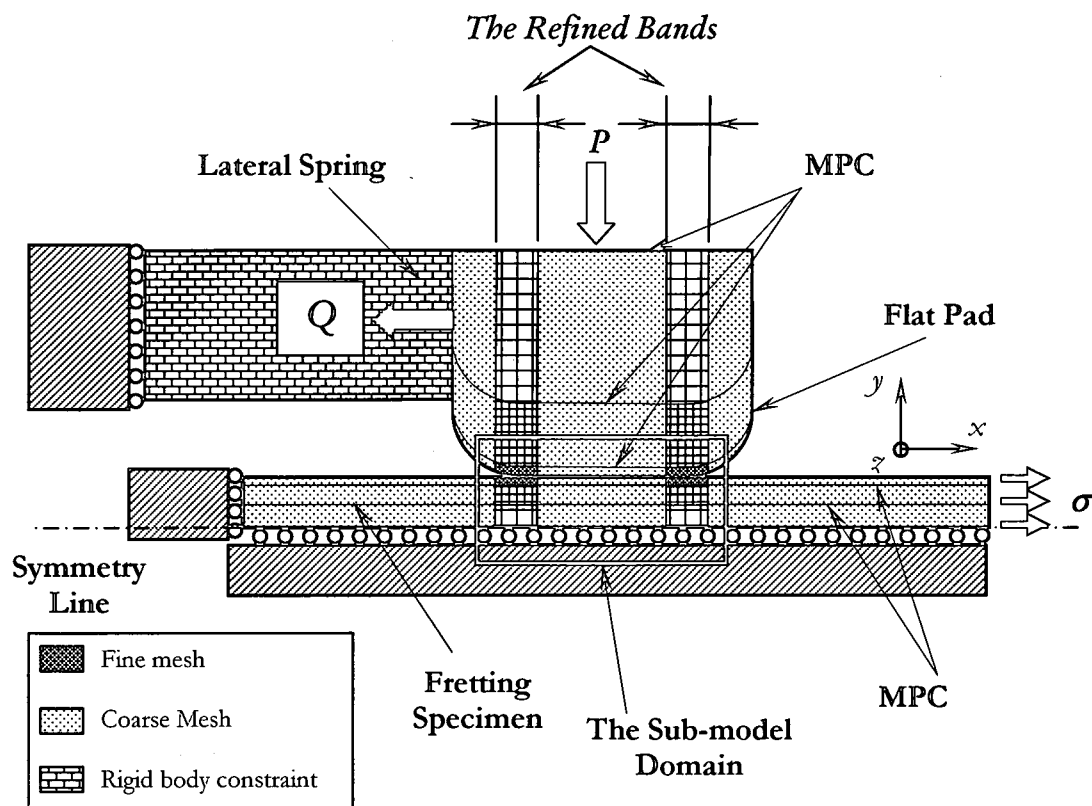


Figure 3.4 Global model of the flat pad case

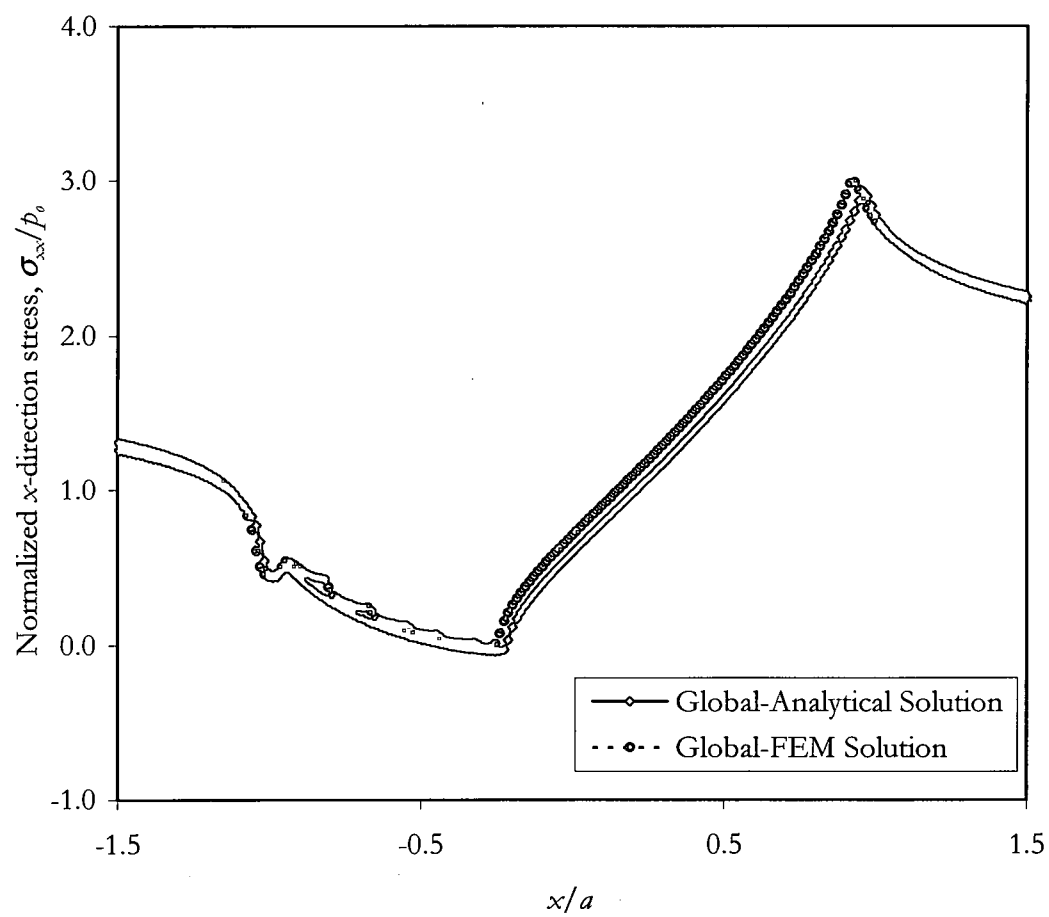


Figure 3.5 Comparison between the FEM and the analytical solutions. Specimen thickness = 1.9 mm. Cylindrical pad radius = 50.8 mm. Loading conditions: $\sigma_{max} = 529$ MPa, $P = 1335$ N, $f = 0.75$, $Q/fP = 0.85$. Mesh size: $12.4 \mu\text{m} \times 12.4 \mu\text{m}$.

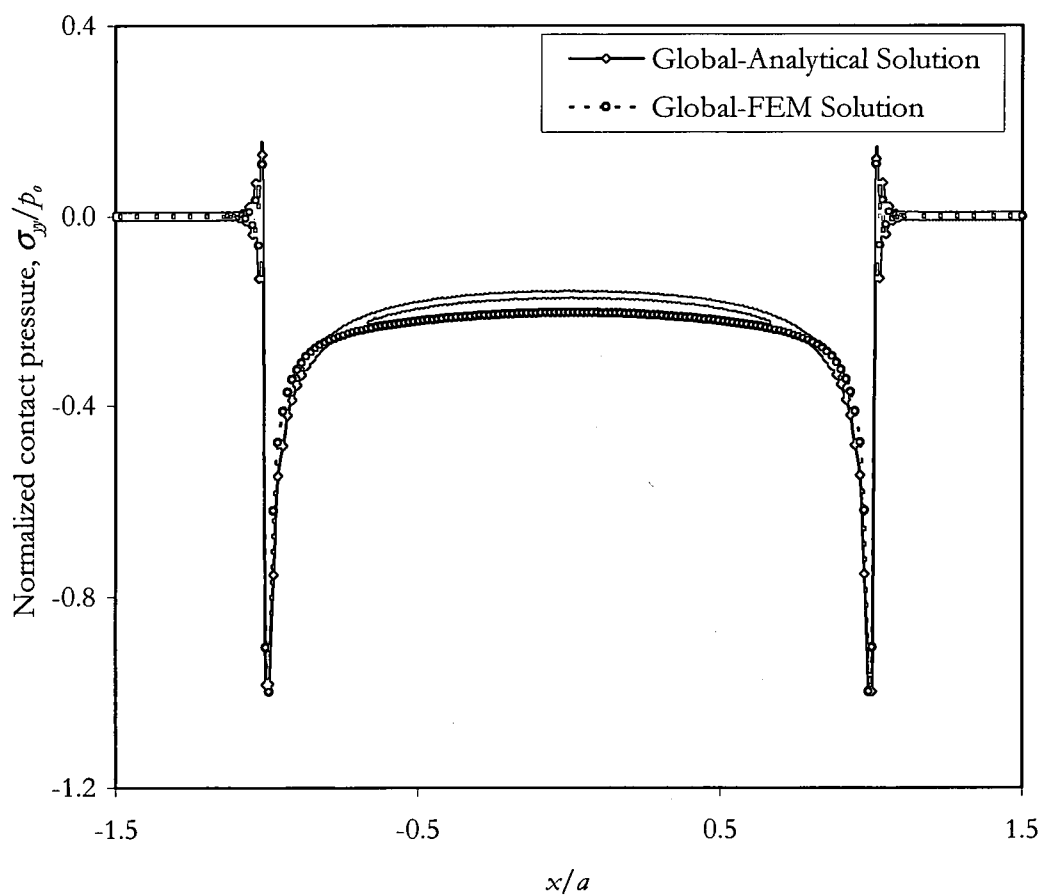


Figure 3.6 Comparison between the FEM and the analytical solutions. Specimen thickness = 1.9 mm. Flat pad. Loading conditions: $\sigma_{max} = 484$ MPa, $P = 1335$ N, $f = 0.75$, $Q/fP = 0.85$. Mesh size: $28 \mu\text{m} \times 28 \mu\text{m}$.

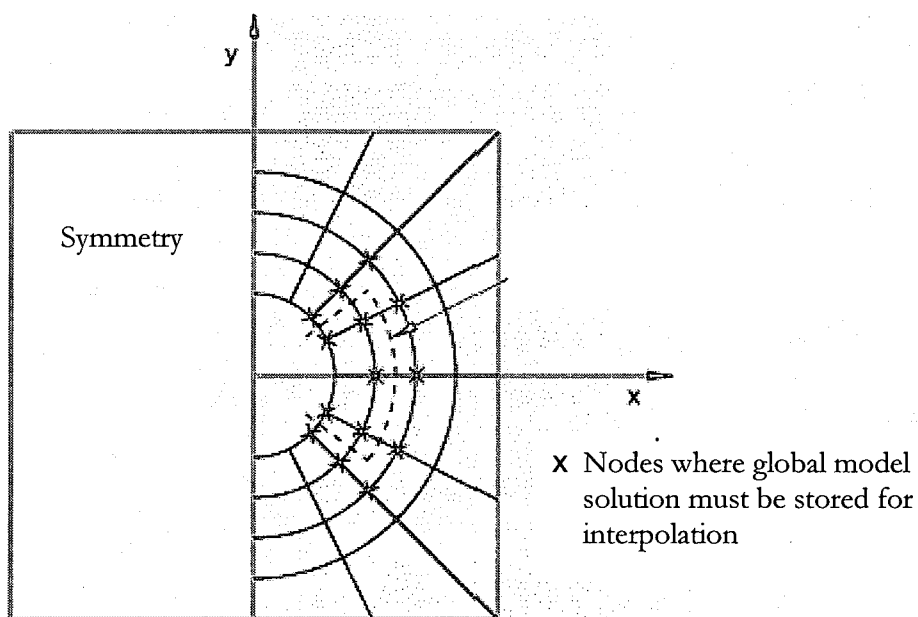


Figure 3.7 Schematic of a sub-model

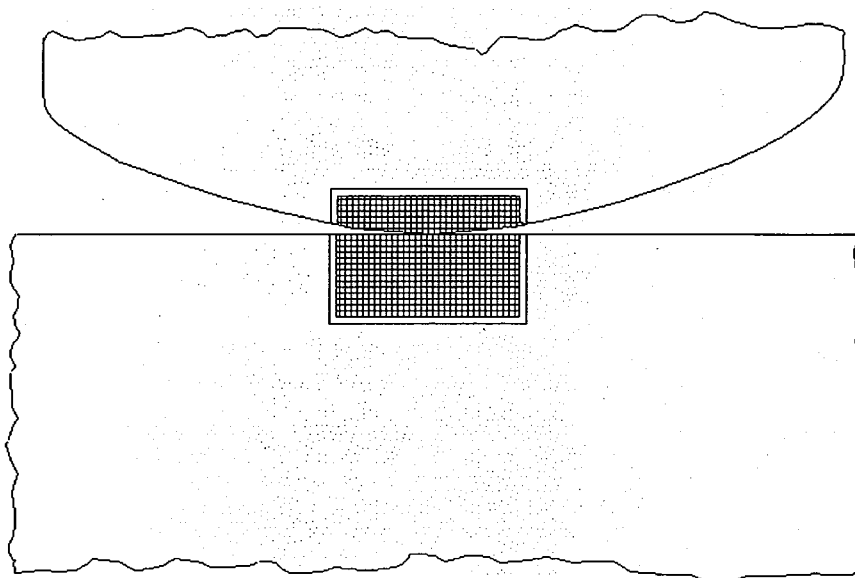


Figure 3.8 A schematic showing the driven nodes

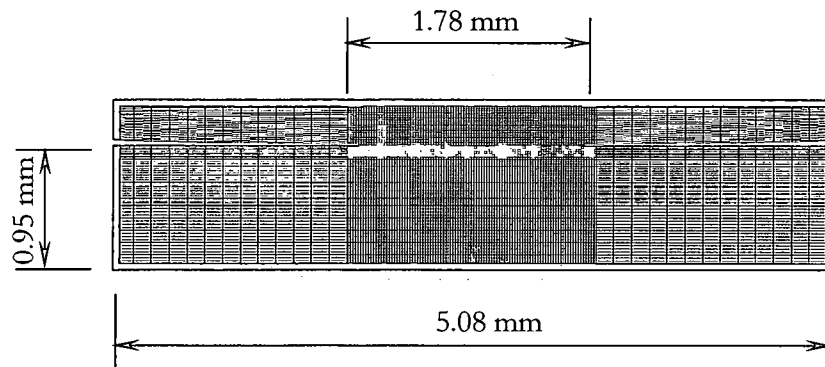


Figure 3.9 Sub-model of the cylindrical pad case

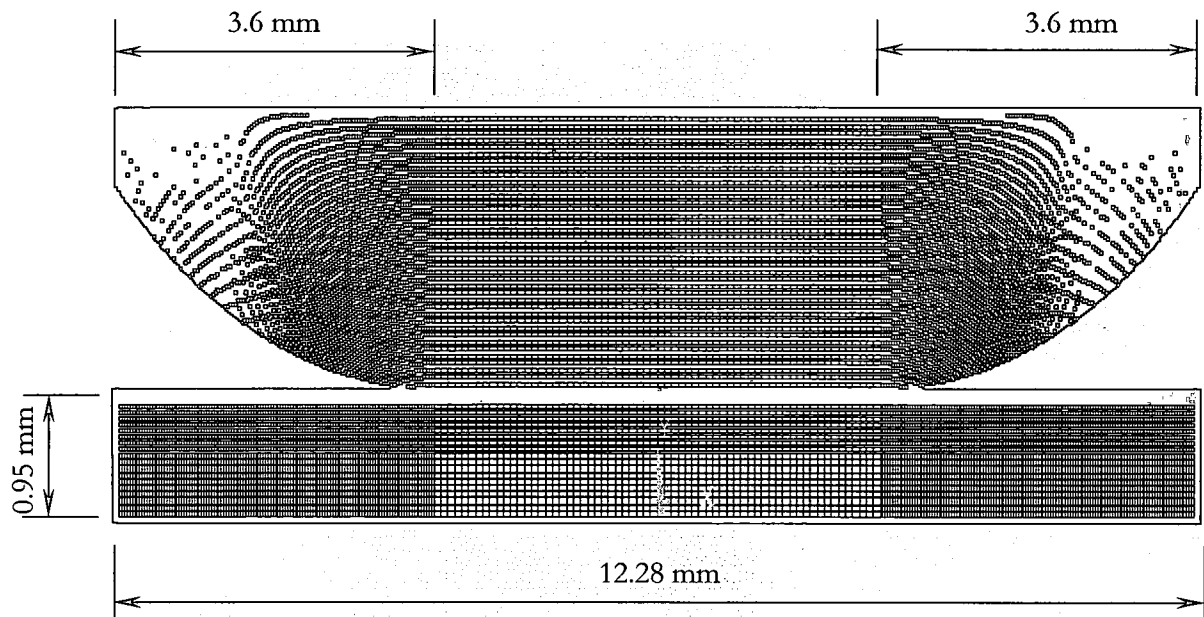


Figure 3.10 Sub-model of the flat pad case

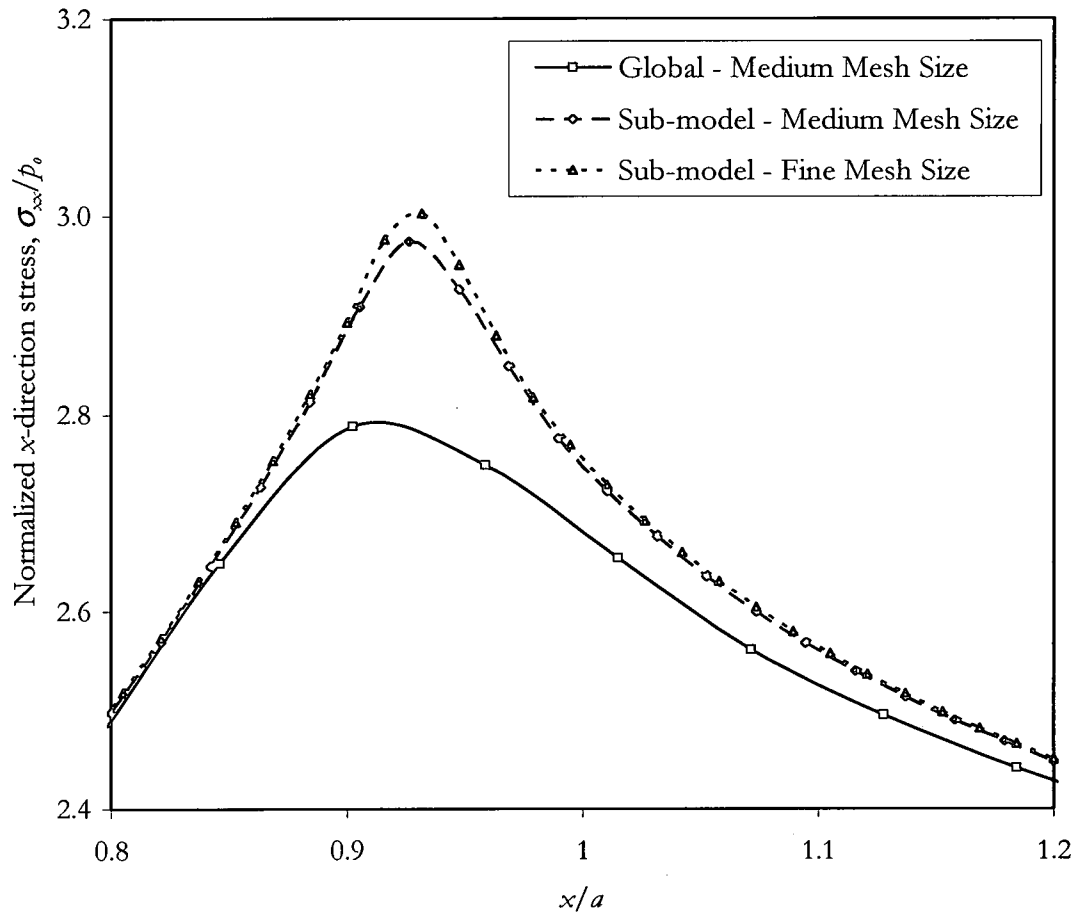


Figure 3.11 Variation of normalized x -direction stress around the trailing edge. Specimen thickness = 1.9 mm. Cylindrical pad radius = 50.8 mm. Loading conditions: $\sigma_{max} = 529$ MPa, $P = 1335$ N, $f = 0.75$, $Q/fP = 0.85$. The medium and fine mesh sizes of the sub-model are $9.3 \mu\text{m} \times 9.3 \mu\text{m}$ and $6.9 \mu\text{m} \times 6.9 \mu\text{m}$, respectively. They were both developed from a global model with a medium mesh size of $24.8 \mu\text{m} \times 24.8 \mu\text{m}$.

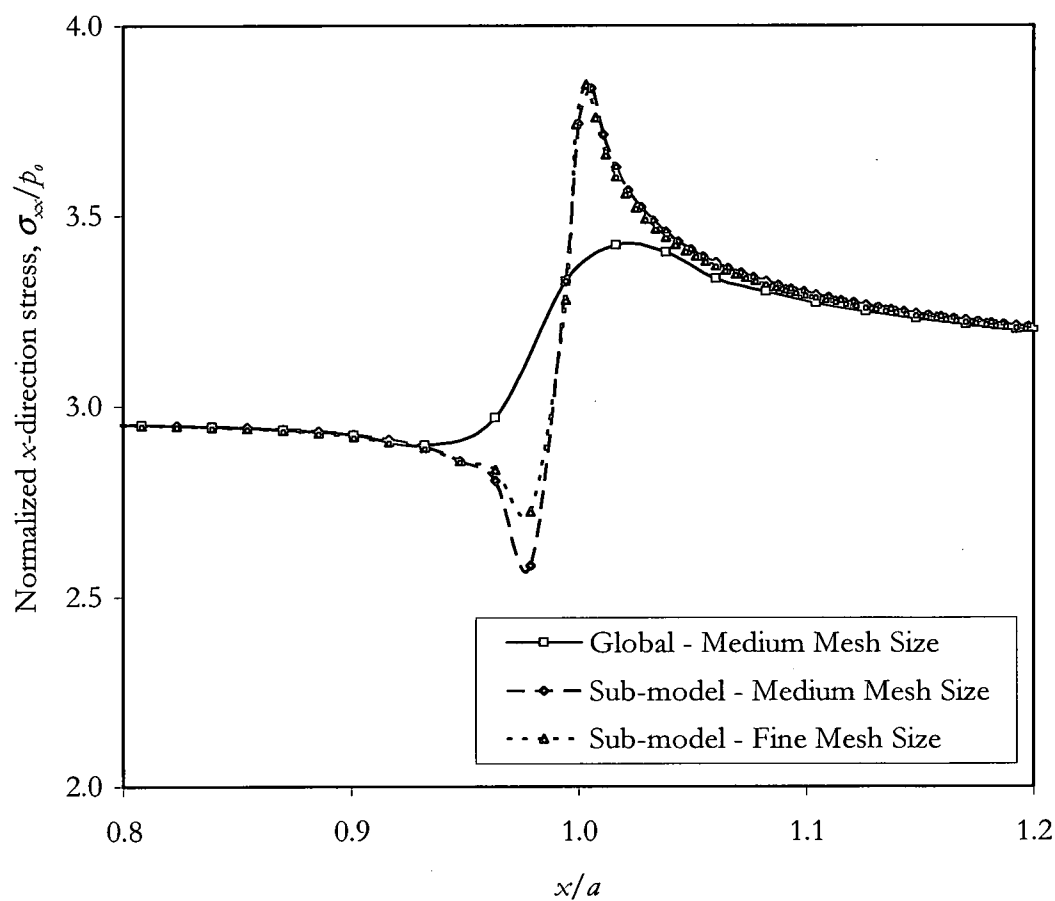


Figure 3.12 Variation of normalized x -direction stress around the trailing edge. Specimen thickness = 1.9 mm. Flat pad. Loading conditions: $\sigma_{max} = 484$ MPa, $P = 1335$ N, $f = 0.75$, $Q/fP = 0.85$. The medium and fine mesh sizes of the sub-model are $14 \mu\text{m} \times 14 \mu\text{m}$ and $11.2 \mu\text{m} \times 11.2 \mu\text{m}$, respectively. They were both developed from a global model with a medium mesh size of $56 \mu\text{m} \times 56 \mu\text{m}$.

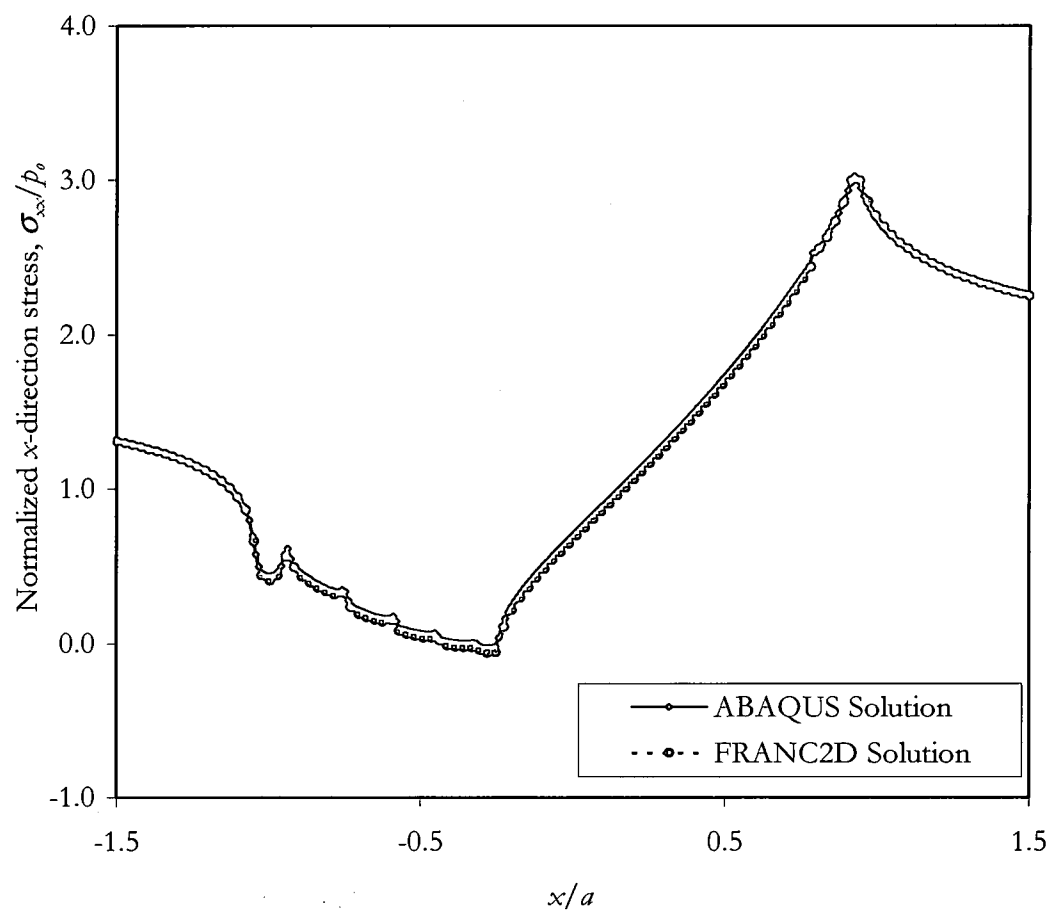


Figure 3.13 Comparison of FRANC2D/L and ABAQUS solutions. Specimen thickness = 1.9 mm. Cylindrical pad radius = 50.8 mm radius. Loading conditions: $\sigma_{max} = 529$ MPa, $P = 1335$ N, $f = 0.75$, $Q/fP = 0.85$. Mesh size: $9.3 \mu\text{m} \times 9.3 \mu\text{m}$.

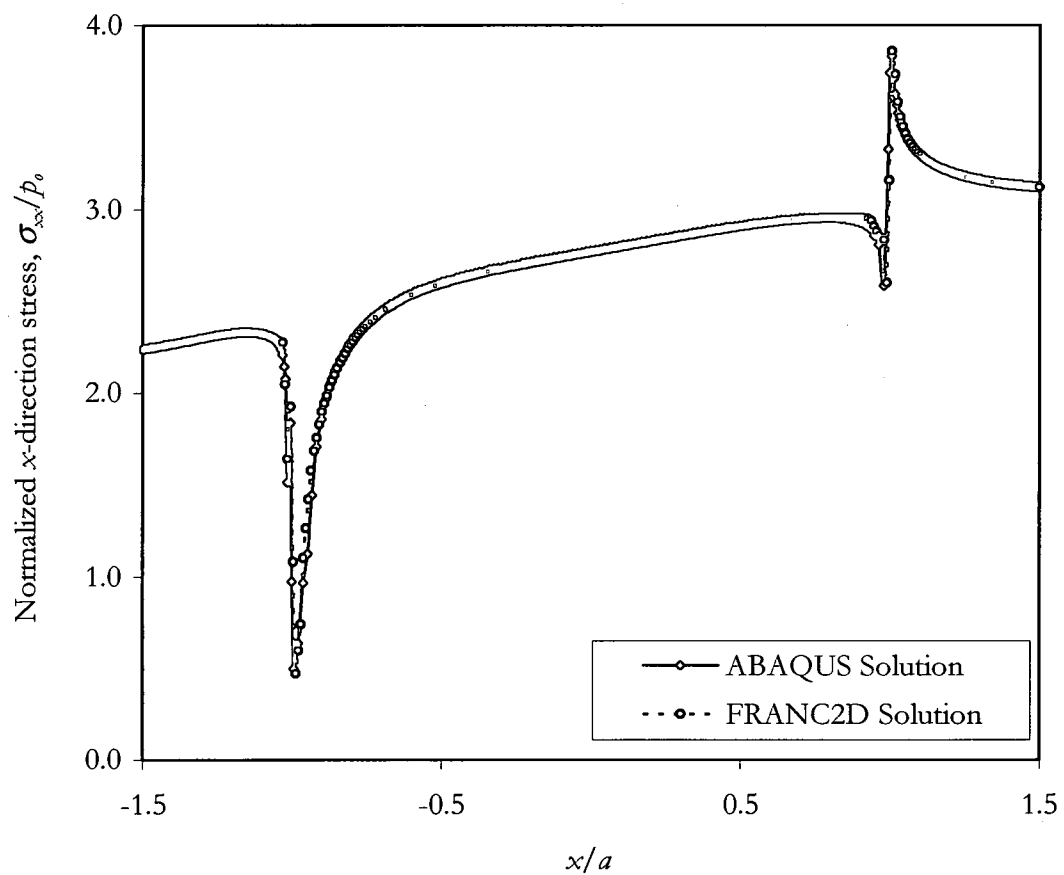


Figure 3.14 Comparison of FRANC2D/L and ABAQUS solutions. Specimen thickness = 1.9 mm. Flat pad. Loading conditions: $\sigma_{max} = 484$ MPa, $P = 1335$ N, $f = 0.75$, $Q/fP = 0.85$. Mesh size: $14 \mu\text{m} \times 14 \mu\text{m}$.

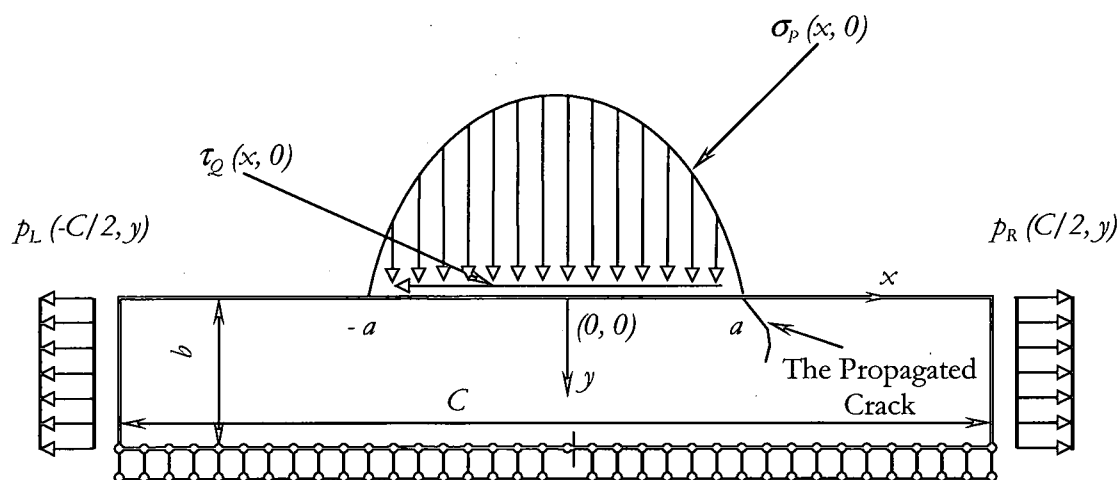


Figure 3.15 Schematic of the sub-model for the cylindrical pad with boundary and loading conditions as used in FRANC2D

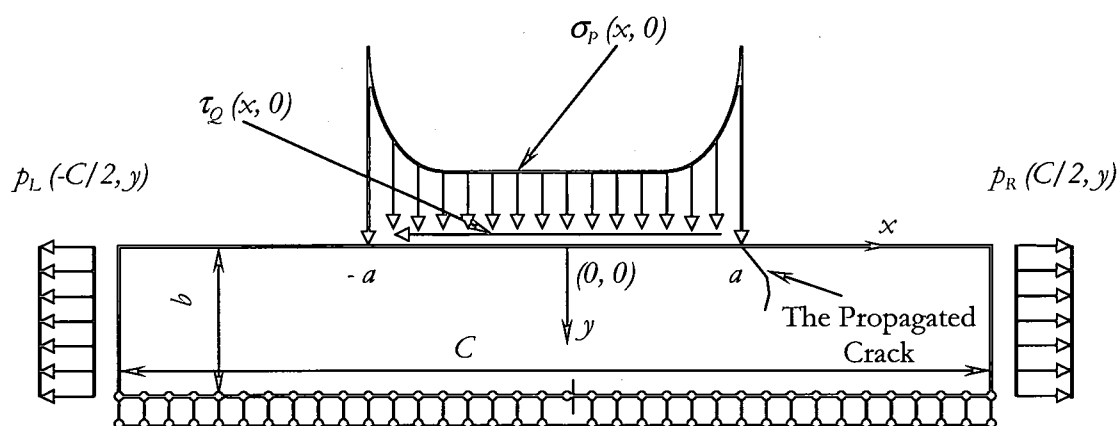


Figure 3.16 Schematic of the sub-model for the flat pad with boundary and loading conditions as used in FRANC2D

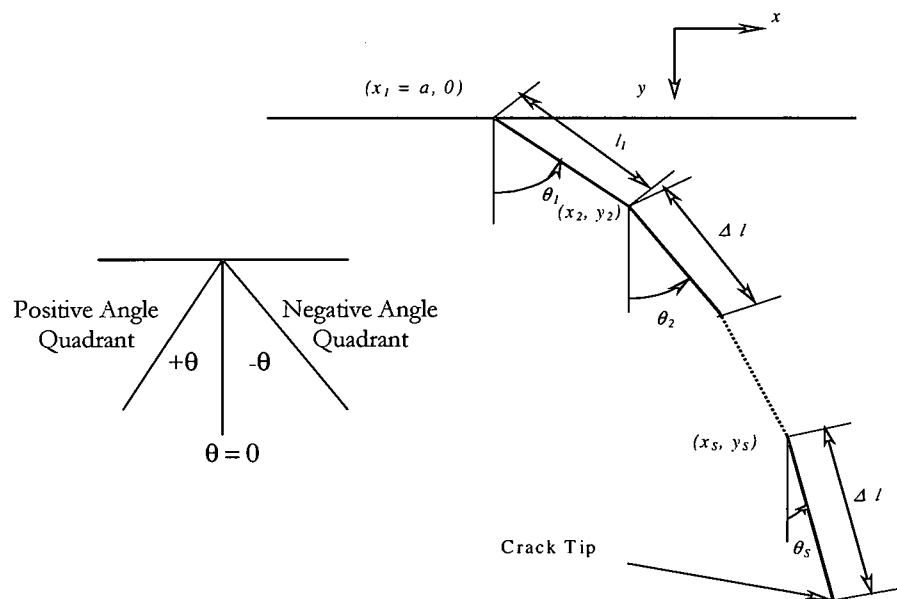


Figure 3.17 Crack growth trajectory

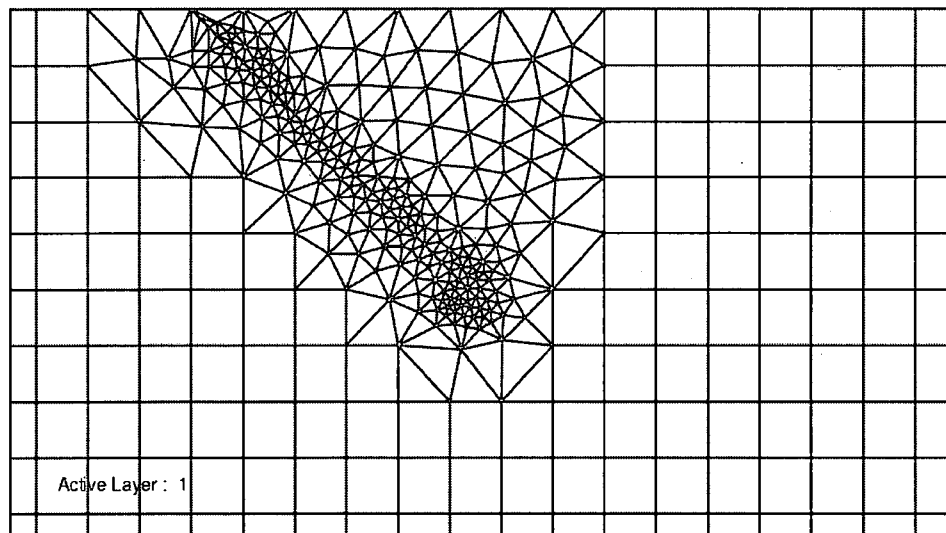


Figure 3.18 The initial configuration of the crack in FRANC2D/L showing a mesh of triangulated elements

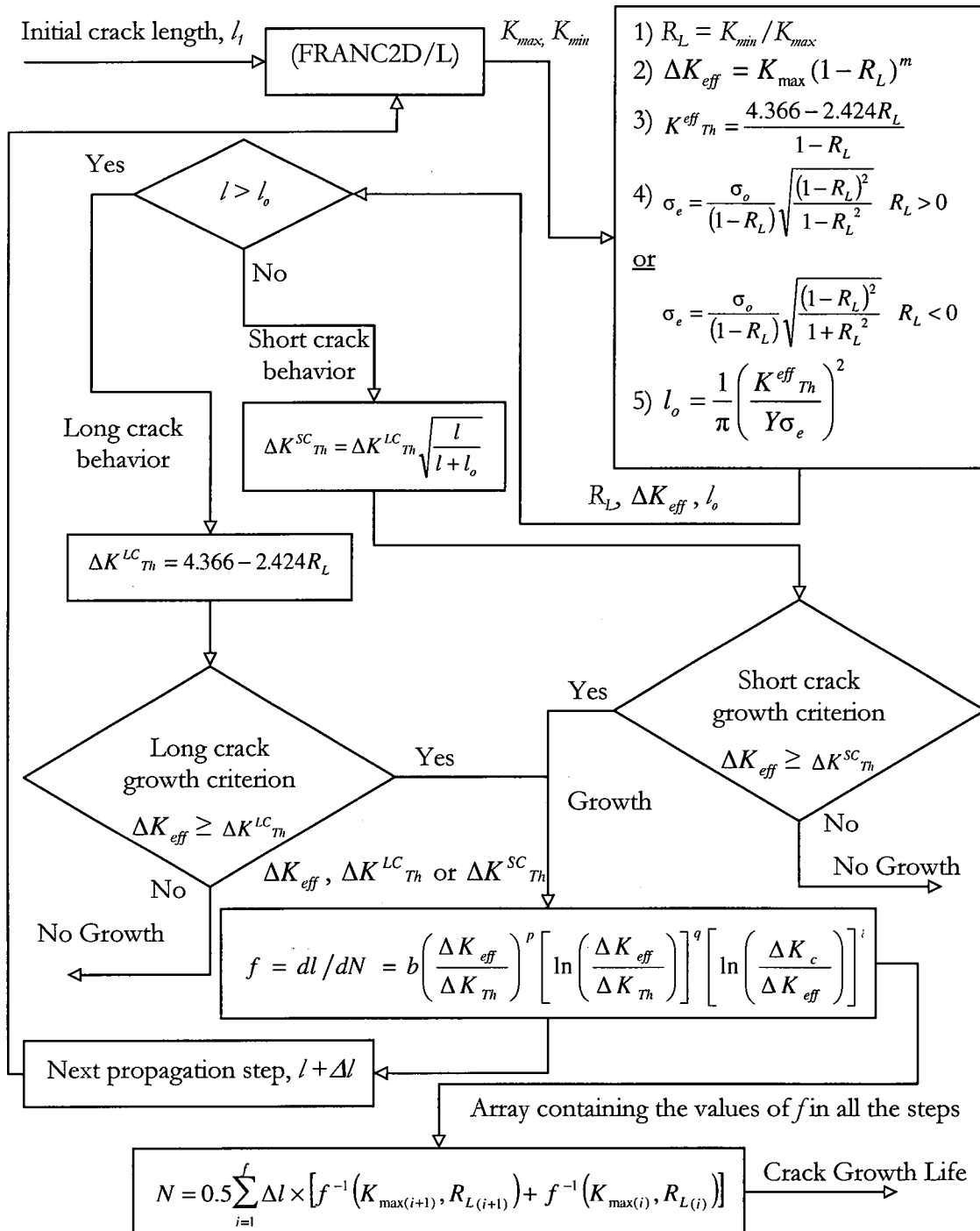


Figure 3.19 Flow chart summarizing the crack growth steps

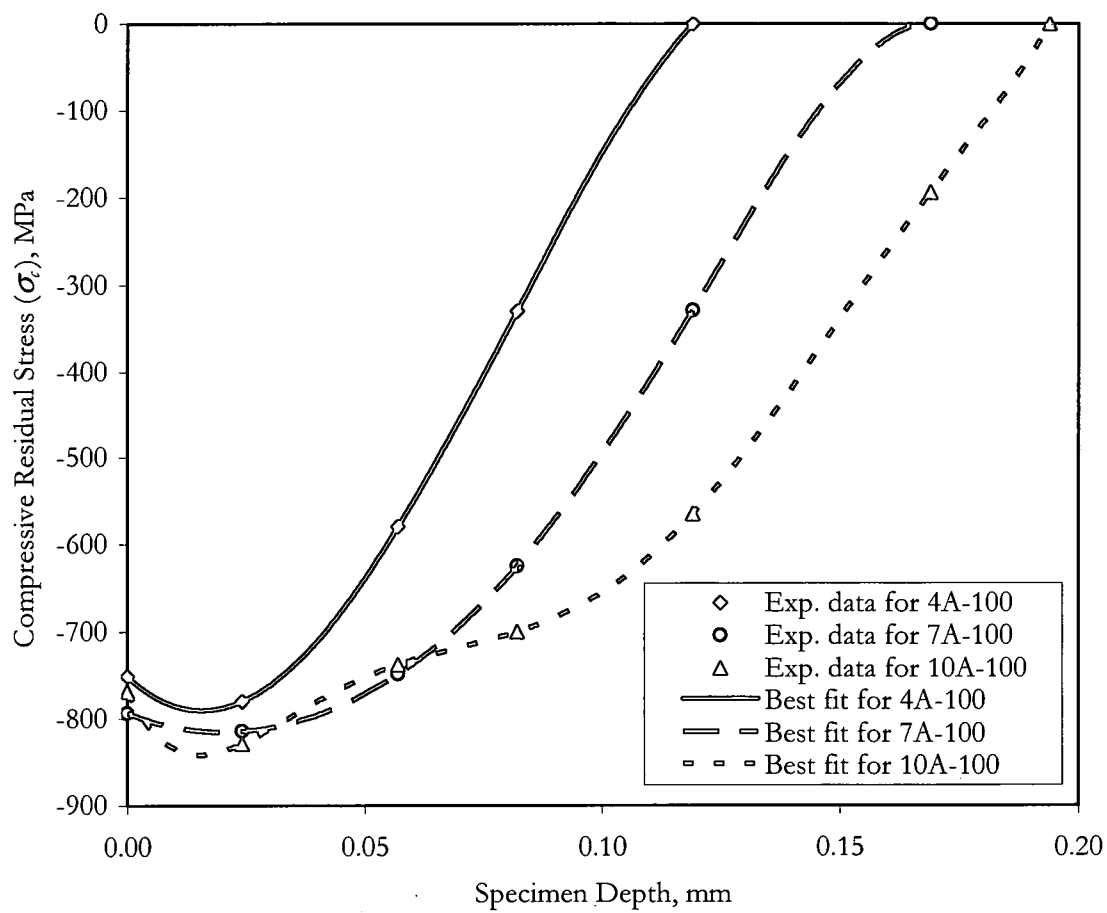


Figure 3.20 Compressive residual stress profiles

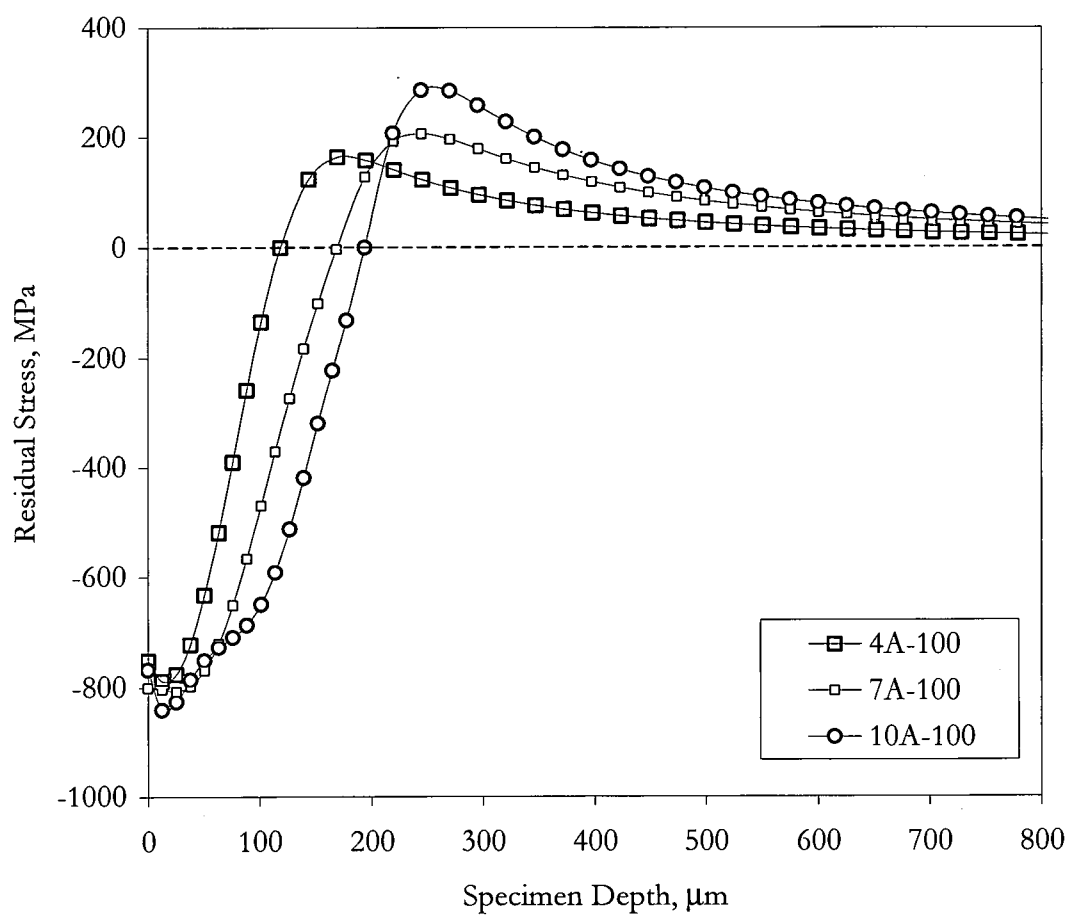


Figure 3.21 The residual stress profiles

Table 3.1 Loading conditions for the cylindrical and flat pads

Case #	Case Name	Pad Radius	Specimen Thickness (mm)	σ_{max} (MPa)	σ_{min} (MPa)	$\Delta\sigma$ (MPa)	R	σ_{eff} (MPa)	P (N)	f	Q/fP	Q_{max} (N)	Q_{min} (N)
1	<i>C_Pad_1</i>	50.8 mm	1.9	700	44	656	0.0	680	1,335	0.5	0.85	570	-570
2	<i>C_Pad_2</i>			529	232	297	0.4	408					
3	<i>C_Pad_3</i>			410	273	137	0.7	250					
4	<i>Flat_Pad_1</i>	Flat	1.9	691	36	655	0.0	675	1,335	0.5	0.85	570	-570
5	<i>Flat_Pad_2</i>			484	174	310	0.4	396					
6	<i>Flat_Pad_3</i>			535	356	179	0.7	327					

Table 3.2 Experimental fretting fatigue lives [19]

Case #	Case Name	Pad Radius	Specimen Thickness (mm)	σ_{max} (MPa)	σ_{min} (MPa)	$\Delta\sigma$ (MPa)	R	σ_{eff} (MPa)	P (N)	N_t (Cycles)
1	<i>C_Pad_1</i>	50.8 mm	1.9	700	44	656	0.0	680	1,335	13,734
2	<i>C_Pad_2</i>			529	232	297	0.4	408		612,604
3	<i>C_Pad_3</i>			410	273	137	0.7	250		22,910,129
4	<i>Flat_Pad_1</i>	Flat	1.9	691	36	655	0.0	675	1,335	19,453
5	<i>Flat_Pad_2</i>			484	174	310	0.4	396		1,176,308
6	<i>Flat_Pad_3</i>			535	356	179	0.7	327		5,164,669

Table 3.3 Loading conditions for the parametric study

(a) Loading conditions for different values of the normal load P

Case #	Pad Radius	σ_{max} (MPa)	σ_{min} (MPa)	$\Delta\sigma$ (MPa)	R	σ_{eff} (MPa)	f	Q/fP	P (N)	Q_{max} (N)	Q_{min} (N)
1	50.8 mm	529	232	297	0.4	408	0.5	0.85	1,335	570	-570
2									2,670	1,140	-1,140
3									4,005	1,710	-1,710
4	Flat	484	174	310	0.4	396	0.5	0.85	1,335	570	-570
5									2,670	1,140	-1,140
6									4,005	1,710	-1,710

(b) Loading conditions for different values of the coefficient of friction f

Case #	Pad Radius	σ_{max} (MPa)	σ_{min} (MPa)	$\Delta\sigma$ (MPa)	R	σ_{eff} (MPa)	P (N)	Q/fP	f	Q_{max} (N)	Q_{min} (N)
1	50.8 mm	529	232	297	0.4	408	1,335	0.85	0.5	570	-570
2									0.75	855	-855
3									1.0	1,140	-1,140
4	Flat	484	174	310	0.4	396	1,335	0.85	0.5	570	-570
5									0.75	855	-855
6									1.0	1,140	-1,140

Table 3.3 Loading conditions for the parametric study (Continued)

(c) Loading conditions for different values of the ratio Q/fP

Case #	Pad Radius	σ_{max} (MPa)	σ_{min} (MPa)	$\Delta\sigma$ (MPa)	R	σ_{eff} (MPa)	P (N)	f	Q/fP	Q_{max} (N)	Q_{min} (N)
1	50.8 mm	529	232	297	0.4	408	1,335	0.5	0.35	234	-234
2									0.60	400	-400
3									0.85	570	-570
4	Flat	484	174	310	0.4	396	1,335	0.5	0.35	234	-234
5									0.60	400	-400
6									0.85	570	-570

Table 3.4 Experimental data from Ref. [44]

Case #	Almen, % Cov.	σ_{max} (MPa)	σ_{min} (MPa)	$\Delta\sigma$ (MPa)	R	P (N)	Q_{max} N	Q_{min} (N)	ΔQ (N)	Avg. N_i (Cycles)
1	4A-100	500	50	450	0.1	1,335	1,451	-557	2,008	60,060
2							976	-600	1,576	
3							1,364	-666	2,030	
4	7A-100	550	50	500	0.11	1,335	1,082	-964	2,046	155,540
5							804	-719	1,523	
6	10A-100	500	50	450	0.1	1,335	1,501	-692	2,193	3,563,930
7							1,607	-440	2,047	

Table 3.5 The mesh sizes used for global and sub-models

Pad Type	Grid Size		$\sigma_{xx, max}$ (MPa)	Discretization Error	
				Difference	ε_d (%)
Cylindrical Pad	Global	Medium (24.8 μm x 24.8 μm)	848	--	--
		Sub-model Medium (9.3 μm x 9.3 μm)	905	--	--
		Fine (6.9 μm x 6.9 μm)	913	8.00	0.88
	Global	Fine (12.4 μm x 12.4 μm)	882	--	--
		Sub-model Medium (9.3 μm x 9.3 μm)	898	--	--
		Fine (6.9 μm x 6.9 μm)	907	9.00	0.99
Flat Pad	Global	Medium (56 μm x 56 μm)	533	--	--
		Sub-model Medium (14 μm x 14 μm)	596	--	--
		Fine (11.2 μm x 11.2 μm)	598	2.00	0.33
	Global	Fine (28 μm x 28 μm)	557	--	--
		Sub-model Medium (14 μm x 14 μm)	596	--	--
		Fine (11.2 μm x 11.2 μm)	598	2.00	0.33

Table 3.6 The boundary condition errors for the sub-models based on σ_{xx}

Pad Type	Grid Size		$\sigma_{xx, max}^{mbc}$ (MPa)	$\sigma_{xx, max}^{bc}$ (MPa)	Boundary Condition Error	
					Difference	ε_{bc} (%)
Cylindrical Pad	Sub-model	Medium (9.3 μm x 9.3 μm)	905	898	-7.00	-0.78
		Fine (6.9 μm x 6.9 μm)	913	907	-6.00	-0.66
Flat Pad	Sub-model	Medium (14 μm x 14 μm)	596	596	0.00	0.00
		Fine (11.2 μm x 11.2 μm)	598	598	0.00	0.00

Table 3.7 The curve-fitting constants of Equation (3.12)

Curve Fitting Constants	4A-100	7A-100	10A-100
$Y_0 =$	119 μm	169 μm	194 μm
$p =$	58	75.9	62.8
$q =$	342.7	434.3	609.2
$r =$	1.1	1.9	1.3
$s =$	6.5	10.9	12.8

Table 3.8 Critical values of the residual stress profiles (Figure 3.21)

Case	Compressive Residual Stress at the Surface (MPa)	Maximum Compressive Residual Stress (MPa)	Maximum Tensile Residual Stress (MPa)
4A-100	-751	-789 (at depth of 13 μm)	164 (at depth of 170 μm)
7A-100	-793	-807 (at depth of 24 μm)	205 (at depth of 235 μm)
10A-100	-768	-840 (at depth of 13 μm)	290 (at depth of 250 μm)

CHAPTER IV

RESULTS AND DISCUSSIONS

This chapter presents the results of the research performed as part of this dissertation. The discussion of the results is divided into three main sections. The first section describes the results obtained from the investigation of the effect of effective stress σ_{eff} on crack propagation behavior. The results of the parametric study that quantifies the effects of the normal load P , the coefficient of friction f , and the ratio Q/fP , will be discussed in the second section. The final section discusses the results obtained from the investigation of the effects of shot-peening and its intensities on crack propagation behavior.

As discussed in the previous chapters, the material of all the investigated fretting specimens (unpeened and shot-peened) was titanium alloy Ti-6Al-4V. For the unpeened cases, the fretting fatigue specimens with 1.9 mm thickness were used; while specimens with 6.4 mm thickness were used for the shot-peened cases. The finite element sub-modeling technique was used for all the cases to help in achieving a more precise stress, strain, and displacement fields in the vicinity of the critical contact zone. FRANC2D/L fracture mechanics code was used for the crack propagation analysis of the unpeened cases; while FRANC2D was used for the shot-peened ones. In both of these codes, the stress intensity factors were extracted so that they can be used in a crack growth model to estimate the propagation life of the fretting fatigue cracks. The crack growth model used in this dissertation was the Walker crack growth model.

4.1 Effect of the Effective Stress (σ_{eff})

The results of this section are divided into three parts. The first part discusses the application of crack growth criteria. The second part addresses the influence of the effective stress σ_{eff} on the effective stress intensity factor ΔK_{eff} . In the last part, the effects of effective stress on the propagation and initiation lives of the fretting fatigue cracks are investigated.

4.1.1 Crack Growth Criteria

In general, crack growth depends on the material properties as well as the stress and strain distribution around the assumed crack. The crack growth criteria are defined as follows:

$$\Delta K_{eff} \geq \Delta K_{Th}^{LC} \quad \text{for } l > l_o \quad (\text{long crack behavior}) \quad (4.1)$$

$$\Delta K_{eff} \geq \Delta K_{Th}^{SC} \quad \text{for } l < l_o \quad (\text{short crack behavior}) \quad (4.2)$$

Figures 4.1 and 4.2 were constructed, for all the cases given in Table 3.1, using the value of axial stress ratio \bar{R} instead of R_L , because R_L changes at every step of crack increment. Table 4.1 summarizes the parameters used in constructing these diagrams. These figures were plotted to estimate the minimum crack length, required for growth to start, for various cases of cylindrical and flat pads, respectively. To generate these figures, size dependent threshold was calculated using Equation (2.95) and plotted against crack length. In addition, the initial effective stress intensity factors ΔK_{eff_1} (Equation 2.85) for different initial crack lengths (3 μm , 6 μm , and 20 μm for cylindrical pads and 6 μm , 10 μm , 20 μm , and 30 μm for flat pads) were calculated and shown in these figures. The intersections of the two sets of curves yielded the minimum estimated crack length required for growth to start.

During this study, four different initial crack lengths (20 μm , 30 μm , 50 μm , and 80 μm) were used for each of the loading conditions and pad geometries. The minimum initial crack length to be tested was chosen to be 20 μm , which is about two times the grain size and is larger than the minimum estimated initial crack length required for growth to start. This length was further used to estimate crack growth life. From Figures 4.1 and 4.2, it can be noticed that for the high loading case, the cracks have a tendency to grow at a lower initial length than that for the lower loading case as shown by the arrows. From the same figures, one can conclude that the propagation behavior of fretting fatigue cracks in cylindrical pad cases is worse than that of the flat pads as demonstrated by the difference in the estimated values of the initial crack length. For example, by comparing the high load cases, *C_Pad_1* and *Flat_Pad_1*, the difference between the estimated initial crack lengths is about 9 μm .

4.1.2 Effective Stress Intensity Factors (ΔK_{eff})

The most important crack growth parameters are the opening Mode I stress intensity factor K_{max} , and the stress intensity ratio (or the local stress ratio) R_L . Together, they define the effective stress intensity factor ΔK_{eff} , in Walker's formula (Equation (2.85)). The effective stress intensity factor is an essential parameter in the estimation of the crack growth life. Since the values of K_{max} and R_L change at each propagation step, ΔK_{eff} will consequently have a new value at each propagation step. The variation of the effective stress intensity factor ΔK_{eff} through the crack growth is plotted as a function of crack length for each of the cases in order to examine the effects of the loading level (Figures 4.3 and 4.4). It can be noticed that the effective stress intensity factor ΔK_{eff} increases as the crack length increases. This indicates

that the crack will grow with an initial crack length of 20 μm . This is true for all the studied cases. It can also be noticed that as the value of effective stress σ_{eff} increases, the effective stress intensity factor ΔK_{eff} increases. The rate of increase of ΔK_{eff} , increases with crack length. Therefore, for the cylindrical pads, the ratio $\Delta K_{eff}(\sigma_{eff} - \text{High})/\Delta K_{eff}(\sigma_{eff} - \text{Low})$, was found to be about 1.75 and 3.07, at the beginning and the end of crack propagation, respectively. Similar behavior was found for the flat pads.

4.1.3 Crack Propagation Life (N_p)

The crack propagation life N_p , is defined in terms of the number of cycles for a crack to grow from an initial length l_i , to the final length l_f . This is computed using Equation (2.88). The final length is assumed to be the crack length at which failure occurs. Here, the final length was chosen to be 0.45 mm for both the cylindrical and flat pad cases. This was done to ensure that the sub-model length C (Figures 3.15 and 3.16), was at least ten times the maximum crack length¹. Since the early steps of crack propagation analysis usually define the majority of the crack growth life, at 0.45 mm crack length, about 90 % (or more) of the propagation life will be defined. The rest of the propagation life can be easily predicted by extrapolation. This portion of life was then added to each case. It was found to vary between 2% to 8% of the total life.

As mentioned earlier, four different initial crack lengths were investigated for each case of Table 3.1. Table 4.2 and Figure 4.5 summarize the crack propagation data as a function of the assumed initial crack length. It can be noticed in Figure 4.5 that, as the initial crack length

¹ Note that the value of C for the cylindrical pad cases is 5.08mm and for the flat pad cases is 12.28mm.

increases the propagation life decreases. In addition, at lower loads the number of cycles for the crack to grow to a certain length is higher than that for higher loads. This observation is more apparent for the flat pads. Furthermore, the crack growth life seems to be independent of the initial crack length after a specific value. For example, for an initial crack length ≥ 51 μm , the propagation life does not appear to change significantly. The propagation lives, which were plotted in Figure 4.5, were later normalized by dividing them by the corresponding experimental total lives. These normalized lives were plotted against the initial crack lengths as shown in Figure 4.6. The same trends as in Figure 4.5, are noticed. However, as the initial crack length increases, the normalized propagation life N_p/N_t decreases and as the effective stress gets lower, the normalized propagation life N_p/N_t approaches zero. This means, that for low values of effective stress, the dominant portion of the fretting fatigue crack life is consumed during the initiation phase.

As mentioned earlier, an initial crack length of 20 μm was used for the evaluation of propagation life. Figures 4.7 and 4.8 show the propagation life as a function of the loading level for the cylindrical and flat pads, respectively. The propagation life was calculated by Equation (2.88). From these figures, it can be noticed that as the effective stress σ_{eff} decreases the crack propagation life increases. Let the values of σ_{eff} be denoted as "High", "Intermediate", and "Low" for three loading cases. For the cylindrical pad, the propagation life is increased by factors $N_{Intermediate}/N_{High} = 2.34$ and $N_{Low}/N_{High} = 6.86$, respectively as the load is decreased from "High" to "Low" level. For the flat pad cases, the propagation life is increased by factors $N_{Intermediate}/N_{High} = 4.79$ and $N_{Low}/N_{High} = 8.05$. These results also show the

effect of contact geometry on the crack propagation behavior, which is much better for the flat pads than for the cylindrical pads.

Since the crack life is divided into propagation and initiation portions, the initiation portion also needs to be quantified to understand the fracture process. The initiation life N_i can be calculated by subtracting the propagation life N_p from the total life N_t which is usually determined by experiments. From an experimental study conducted by Lykins [19], the total specimen lives N_t are available for the same loading conditions that are used in this study. Table 4.3 summarizes the results of the crack initiation and propagation lives for cylindrical as well as flat pads. Figures 4.9 and 4.10 show the estimated crack propagation and initiation lives as functions of the effective stress σ_{eff} , respectively for both types of pads. The crack propagation life of the flat pads is higher than that of the cylindrical pads. However, the crack initiation lives (Figure 4.10) for both the cylindrical and flat pad cases are almost the same, as demonstrated by the best-fit curve. The propagation and initiation lives were then normalized by dividing them by the total lives in order to determine their variance with effective stress (Figures 4.11 and 4.12). From these figures, it is noticed that as the effective stress increases, the normalized propagation life increases while the normalized initiation life decreases. This implies that as the effective axial loading gets higher, a larger portion of the life is spent in the propagation phase. This also implies that for higher axial loading, only a small fraction of the crack life is spent in the initiation phase.

4.2 Parametric Study

This section describes the results of the parametric study that investigated the effects of the normal load P , the friction coefficient f , and the ratio Q/fP , on the propagation behavior of the fretting fatigue cracks. Figures 4.13 to 4.15 show the crack propagation life N_p , as a function of normal load, the friction coefficient, and the ratio Q/fP , respectively. Note that as the values of these parameters increase, the propagation life decreases both for the cylindrical and flat pads. Table 4.4 lists the change in propagation lives for various values of the studied parameters for both types of pads. Of these parameters, the ratio Q/fP has the most significant effect on the crack propagation life, followed by the normal load P . The coefficient of friction f , has the least effect on the propagation life. However, if the results of the previous section are considered, the effective stress σ_{eff} still has the dominant effect on the fretting crack propagation life, since the difference between the propagation lives corresponding high and low effective stresses was 62,547 cycles, and 128,556 cycles for the cylindrical and flat pads cases, respectively.

4.3 Effects of Shot-Peening and its Intensity

This section discusses the results from the study of the effects of shot-peening and its various intensities on the propagation behavior of the fretting fatigue cracks. The results are again divided into four parts. The first part discusses the crack initiation location in the shot-peened specimen. The second part evaluates the impact of shot-peening and its intensity on the effective stress intensity factor ΔK_{eff} . In the third part, the effects of shot-peening and its intensity on the propagation and initiation lives of fretting fatigue cracks are discussed. Finally, a parametric study was conducted in the last part to study the effects of the ratio Q/fP and the residual stress relaxation on the propagation behavior of the fretting cracks in shot-peened specimen.

4.3.1 Crack Initiation Location in Shot-Peened Specimens

This study is a continuation of a previous experimental study that addressed the effects of shot-peening and its intensity on the initiation behavior of fretting fatigue cracks in Ti-6Al-4V [44]. In this study, the fretting cracks initiated at the contact surface in the specimens with shot-peening intensities of 4A and 7A; whereas for specimens with 10A intensity, the initiation occurred at a depth away from the contact surface (where the tensile residual stress is maximum). This difference in crack initiation locations was attributed to the relaxation of residual stresses [25, 42, 44, 81]. The extent of this relaxation could not be precisely quantified [44].

As discussed in chapter II, the residual stress profile is divided into two portions: compressive and tensile. The compressive portion is obtained completely by experimental measurement through the use of X-Ray diffraction technique; while the tensile part is determined by using Equation (2.101), which was discussed in chapter II. The relaxation of residual stresses will affect the overall profile. For example, if there is a 50% relaxation in residual stresses, only half of the residual stress (both tensile and compressive) will be present through the specimen thickness.

Here, 0% stress relaxation was assumed, which implies that 100% of the residual stress is present within the specimen thickness. As a result of this assumption, the initiation location of the fretting fatigue cracks would be at a depth below the contact surface for all the three cases of shot-peening intensities. This is the location where the compensatory tensile stress is maximum. Figure 4.16 supports this conclusion, since it shows the total x -direction stress component (σ_x) as a function of the specimen's depth for all the shot-peening intensities cases as well as the unpeened case. This stress is the main contributor to crack propagation, since it

represents the Mode I loading. According to Figure 4.16 and Table 3.8, the locations of the fretting cracks initiation were found to be at depths of 170 μm , 235 μm , and 250 μm , for 4A, 7A, and 10A shot-peening intensity cases, respectively.

Figures 4.17 and 4.18 exhibit the crack growth trajectories for the unpeened and one of the shot-peened cases. The crack has one growing tip for the unpeened case; whereas there are two growing tips for the shot-peened cases (Figures 4.17 and 4.18). Due to the existence of two growing tips in the shot-peening cases, the crack growth trajectory has two branches: upper and lower. Note that there will be no significant difference between the crack growth trajectories of the three shot-peening intensities. The only difference would be in the location of the crack initiation. Note that the lower branch would propagate under tensile stress field. This stress field includes the far field tensile stress produced by the fretting loading and compensatory tensile residual stress induced by shot-peening. However, the upper branch is influenced mostly by the compressive stress field induced by shot-peening since this tip is much closer to the contact surface than the lower one. The growth rate is expected to be lower for the upper branch than the lower one.

The initial crack length for this investigation was chosen to be 25 μm , which is two and a half times the material grain size. The selection was based on the information provided by Figure 4.19. This figure was constructed by the same way as Figures 4.1 and 4.2 were drawn except that the upper branch initial tip of the crack was considered here². This figure shows the effect of shot-peening on the estimated minimum initial crack length needed to start the crack growth. Shot-peening increases this minimum initial crack length to a value of about

² Note that the initial values of the effective stress intensity factors are almost identical for both initial tips of the propagation branches.

20 μm instead of 2 μm as in the unpeened case. Figure 4.19 also shows that there is no significant difference among the three types of shot-peening intensities.

4.3.2 Shot-Peening Intensity and the Effective Stress Intensity Factors (ΔK_{eff})

In this subsection, the crack propagation results of the upper branch will be discussed only. Figure 4.20 shows the effective stress intensity factor ΔK_{eff} as a function of crack length through the crack propagation steps for both the unpeened and the shot-peened cases. From this figure, it can be noticed that, in general, shot-peening reduces the values of the effective stress intensity factor ΔK_{eff} , up to a particular crack length. This is because the effective opening Mode I loading is reduced by the compressive residual stress. This reduces the values of the maximum stress intensity factor K_{max} , and the stress intensity ratio R_L . In addition, Figure 4.20 shows that the effective stress intensity factor decreases as the shot-peening intensity increases from 4A to 10A.

4.3.3 Effect of Shot-Peening Intensity on Crack Propagation Life (N_p)

The same procedure, which was used in the first section, is followed here to obtain the crack propagation results for the unpeened specimens. However, the shot-peened case is more complicated since there are two propagating branches as shown in Figure 4.18. The total lengths of the branches and the initial crack should fall within the limit and do not violate the assumption used for the sub-model length C (Figure 3.15). Note that the propagation steps for both the branches were synchronized; i.e. they are propagating at the same time and with the same crack length increment Δl . In addition, the propagation life was evaluated for each

branch individually. The highest life on a branch represents the propagation life of the specimen.

Since both branches are propagating with the same ΔK , the upper branch will reach the surface of the sub-model before the lower branch reaches the bottom. FRANC2D has a constraint that it becomes unstable when the crack tip approaches the model boundary. Consequently, the crack propagation simulation has to be terminated whenever the upper branch got too close to the upper edge of the sub-model; i.e. within 10 μm . Even though there is a large portion of the uncracked specimen thickness (toward the bottom edge of the sub-model), its propagation life was found to be less than 3% of the total life, which was considered insignificant.

Here, the initial crack length l_i , was chosen to be 25 μm . However, the final crack propagation length was found to be different for each case of shot-peening intensity, because each case has a different initiation location. For example, the initiation location of 4A case is at a depth of 170 μm while for the 10A case, it is at a depth of 250 μm . This indicates that the final length should be shorter for the 4A case since its initial crack is much closer to the surface than that for the 10A case.

Figure 4.21 shows the propagation life for each of the shot-peening intensities for both the upper and the lower propagation branches. It is obvious that the upper branch has the longest propagation life for all the cases. This implies that the propagation life of the upper branch represents the propagation life of the shot-peened specimen. The propagation lives in this figure were calculated by Equation (2.88). Figure 4.22 compares the propagation lives of the three cases of shot-peening intensities (for the upper branch only) along with the propagation life of the unpeened specimen. The first conclusion that can be made from this

figure is that shot-peening improves the propagation life of the fretting fatigue cracks in general. However, it is obvious that the difference in shot-peening intensity has no significant effect on the propagation behavior of the cracks. This conclusion is much obvious in Figure 4.23, which shows the crack propagation life as a function of the shot-peening intensity.

Combining the results of this study with the experimental data of Sabelkin *et al.* [44], the crack initiation life N_i is computed. Figure 4.24 is a bar chart showing the crack initiation lives for the three shot-peening intensities. The crack initiation life increases as the shot-peening intensity increases. This means that the shot-peening intensity has a greater influence on the initiation behavior of the fretting fatigue cracks. This is expected, since the initiation of a crack in a highly compressive stress zone is much more difficult than its propagation.

The propagation and initiation lives were then normalized by dividing them by the corresponding total lives to determine their percentages to the total life as functions of shot-peening intensity as shown by Figures 4.25 and 4.26, respectively. From these figures, one can observe that as the shot-peening intensity increases, the normalized propagation life decreases while the normalized initiation life increases. This means that as the shot-peening intensity gets higher, a higher percentage of the life is spent in the initiation phase. This also implies that for higher shot-peening intensities, only a small fraction of the crack life is spent in the propagation phase.

4.3.4 Parametric Study for Shot-Peened Specimens

In this subsection, the effects of two parameters on the propagation behavior of the fretting fatigue cracks in shot-peened specimens will be investigated. These parameters are the ratio Q/fP and the relaxation of residual stresses.

4.3.4.1 *Effect of the Ratio Q/fP*

The parametric study conducted in the second section studied the effects of the normal load P , the coefficient of friction f , and the ratio Q/fP on the propagation behavior of fretting fatigue cracks in unpeened specimens. The study found that as the normal load P and the ratio Q/fP increases, the propagation life decreases. Since it has been established that the effective stress has the most significant effect on the propagation behavior of fretting fatigue cracks, thus only the effect of the ratio Q/fP on crack propagation behavior in shot-peened specimens was investigated. One shot-peening intensity was studied only; namely 10A. This investigation reveals that the same trend for the ratio Q/fP , as in the unpeened specimen case, was found (Figure 4.27). The propagation life increases as the ratio Q/fP decreases. However, the propagation life was found to increase as the normal load P increases, which is the opposite of the results achieved in the second section (Figure 4.28). This is because the stick zone size c increases with the normal load P (while keeping Q fixed) as defined by Equation (2.29). As the stick zone size gets larger, the slip zone will get smaller thus reducing the slip amplitude. This leads to a higher propagation life.

4.3.4.2 *Effect of Residual Stress Relaxation*

So far in all the shot-peening cases, a 0% residual stress relaxation was assumed. What happens when there is a residual stress relaxation other than 0%? In this subsection, the results, when a 50% residual stress relaxation is assumed, will be discussed. A 50% residual stress relaxation means that only 50% of the residual stress is present through the specimen thickness. The analysis revealed that the locations of the maximum tensile stress in all the shot-peening intensity cases are still at depth and away from the contact surface (the same locations as for the 0% stress relaxation cases) as suggested by Figure 4.29. From this figure, one can also conclude that there is a chance that the crack can initiate at the contact surface for all the shot-peening intensities. However, the initial length has to be longer than 25 μm . From Figure 4.30, it can be noticed that the propagation life is higher for the lower branch in all the cases. This is due to the fact that the compressive zone effect was eliminated to the half because of the 50% stress relaxation; i.e. there is no significant suppression as in the 0% stress relaxation case. In Figure 4.31, the propagation lives of the lower branch of all the cases of shot-peening intensities along with the unpeened case are shown. The propagation lives increased by about 10,000 Cycles more than the 0% stress relaxation case. It is because the maximum compensatory tensile stresses in a 50% stress relaxation cases is only one-half that of the 0% stress relaxation cases that the life is dominated by the lower branch of the crack.

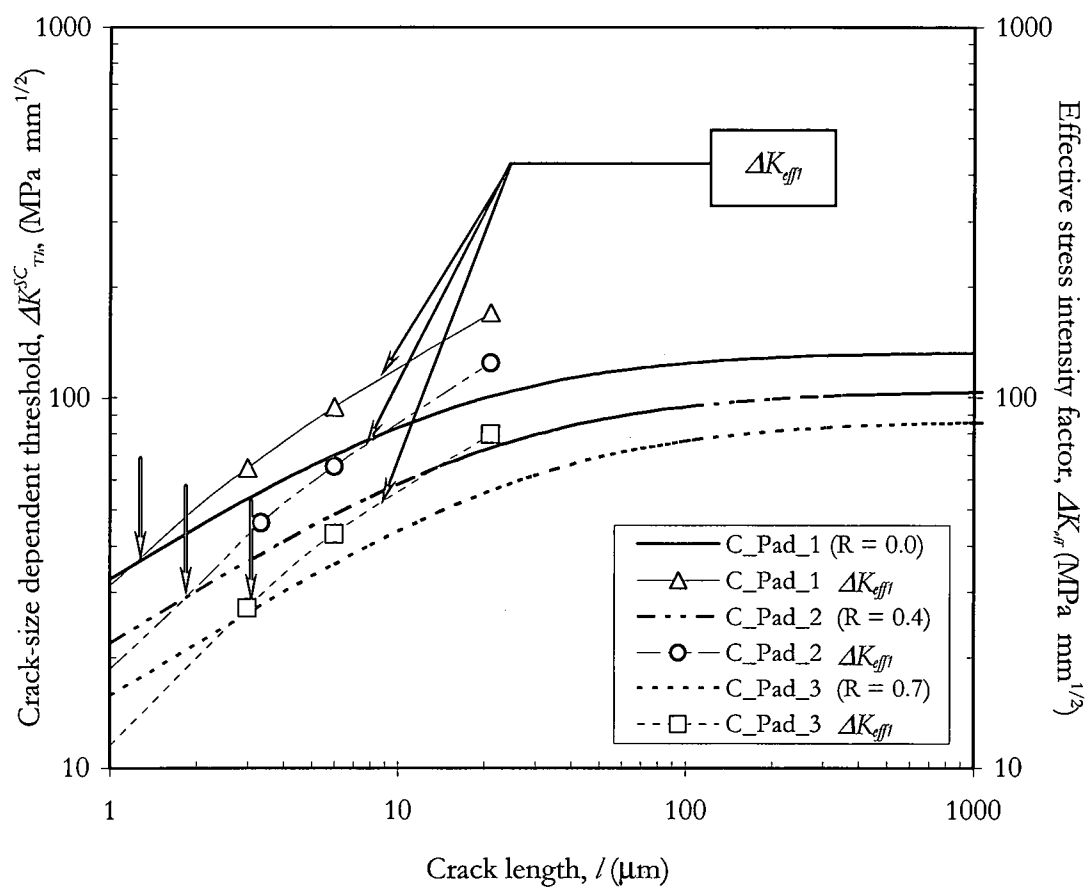


Figure 4.1 Crack-size dependent threshold as a function of the crack length (cylindrical pad)

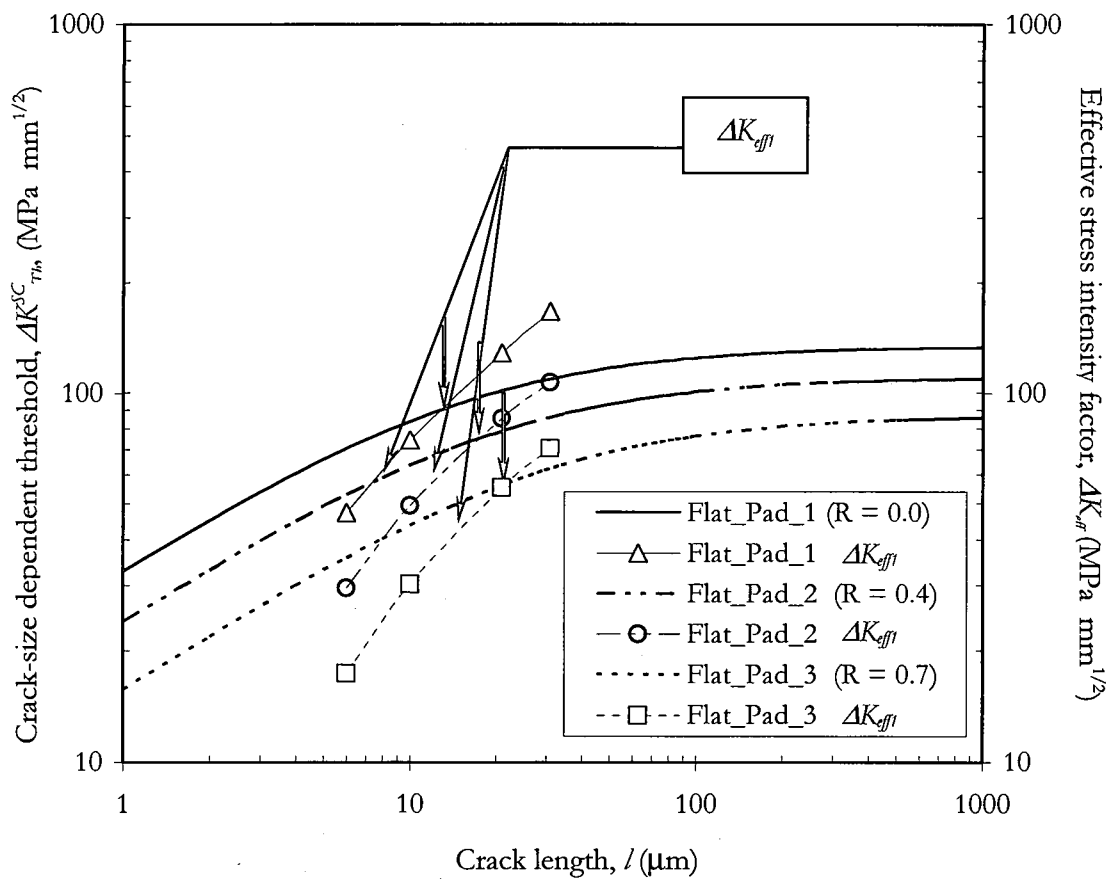


Figure 4.2 Crack-size dependent threshold as a function of the crack length (flat pad)

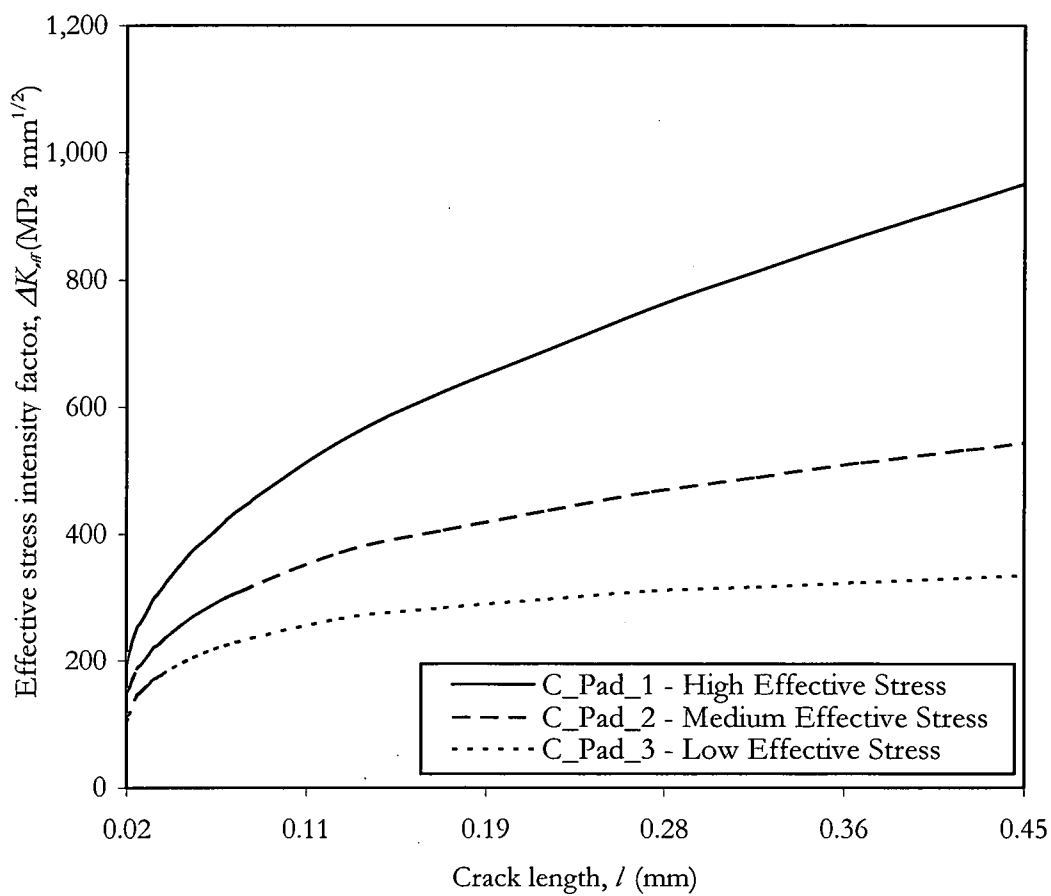


Figure 4.3 Effective stress intensity factor as a function of crack length and loading level (cylindrical pad). $(\sigma_{eff})_{High} = 680 \text{ MPa}$, $(\sigma_{eff})_{Medium} = 408 \text{ MPa}$, $(\sigma_{eff})_{Low} = 250 \text{ MPa}$.

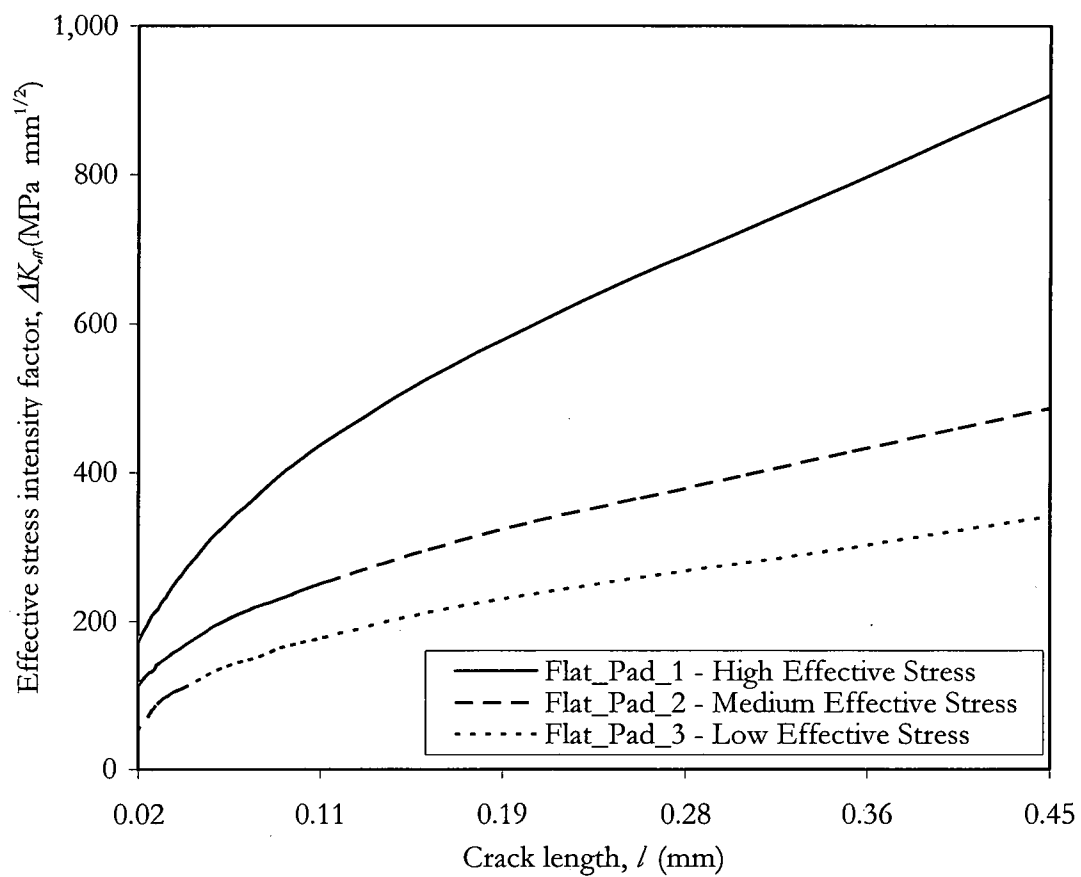


Figure 4.4 Effective stress intensity factor as a function of crack length and loading level (flat pad). $(\sigma_{eff})_{High} = 675$ MPa, $(\sigma_{eff})_{Medium} = 396$ MPa, $(\sigma_{eff})_{Low} = 327$ MPa.

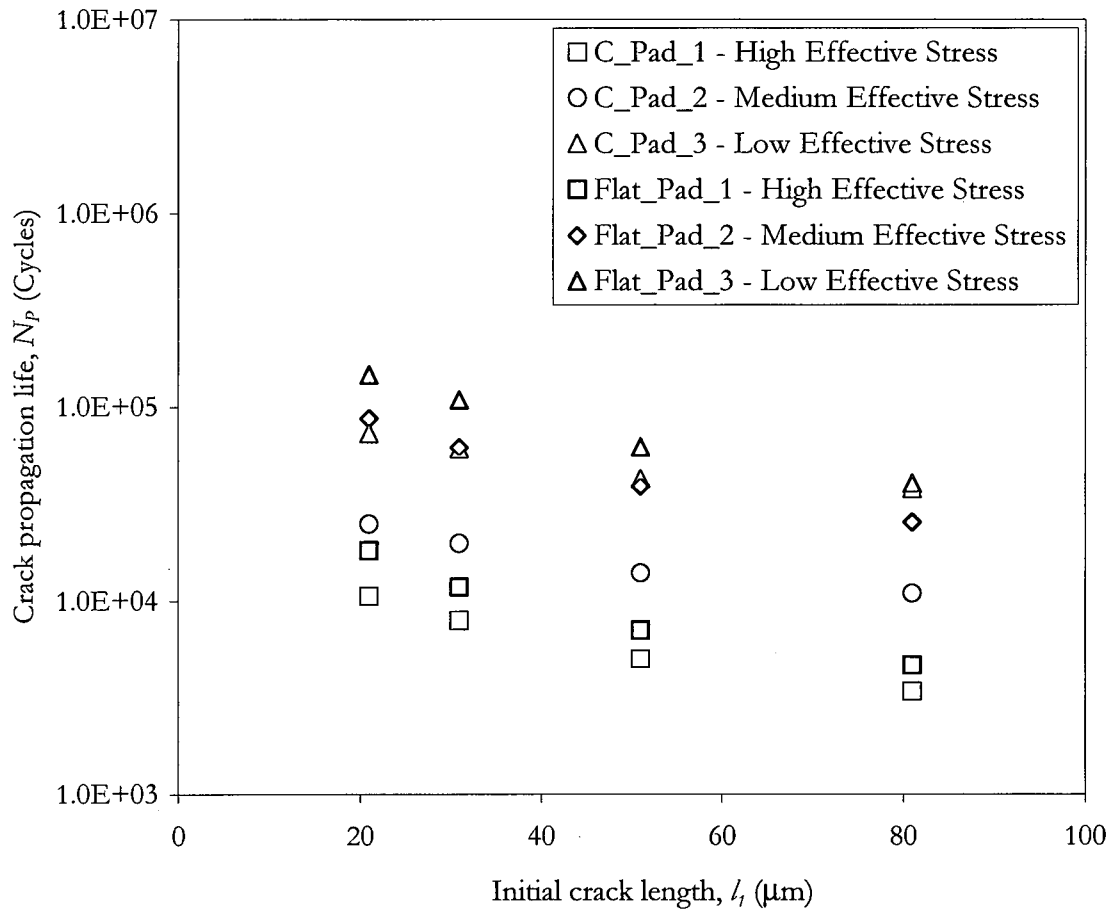


Figure 4.5 Crack propagation life as a function of initial crack length. For cylindrical pads: $(\sigma_{eff})_{High} = 680 \text{ MPa}$, $(\sigma_{eff})_{Medium} = 408 \text{ MPa}$, $(\sigma_{eff})_{Low} = 250 \text{ MPa}$. For flat pads: $(\sigma_{eff})_{High} = 675 \text{ MPa}$, $(\sigma_{eff})_{Medium} = 396 \text{ MPa}$, $(\sigma_{eff})_{Low} = 327 \text{ MPa}$.

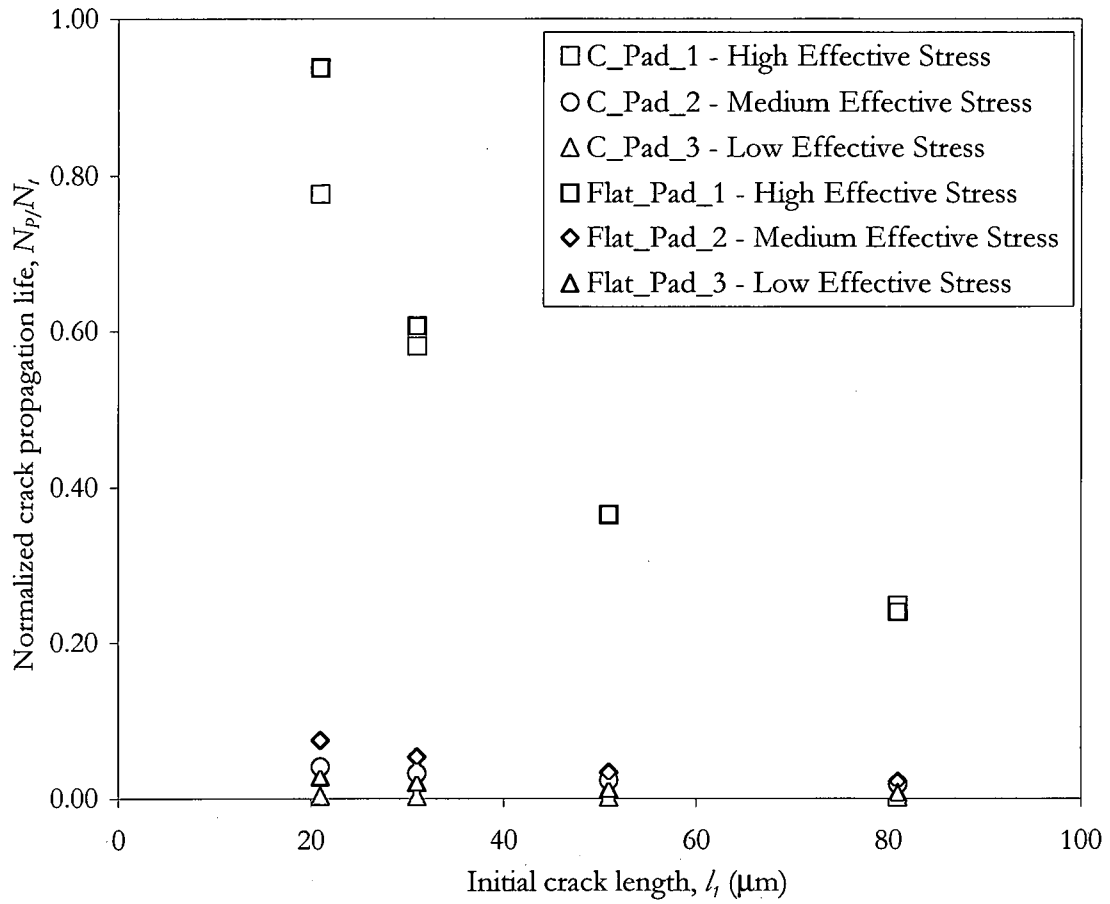


Figure 4.6 Normalized crack propagation life as a function of initial crack length. For cylindrical pads: $(\sigma_{eff})_{High} = 680$ MPa, $(\sigma_{eff})_{Medium} = 408$ MPa, $(\sigma_{eff})_{Low} = 250$ MPa. For flat pads: $(\sigma_{eff})_{High} = 675$ MPa, $(\sigma_{eff})_{Medium} = 396$ MPa, $(\sigma_{eff})_{Low} = 327$ MPa.

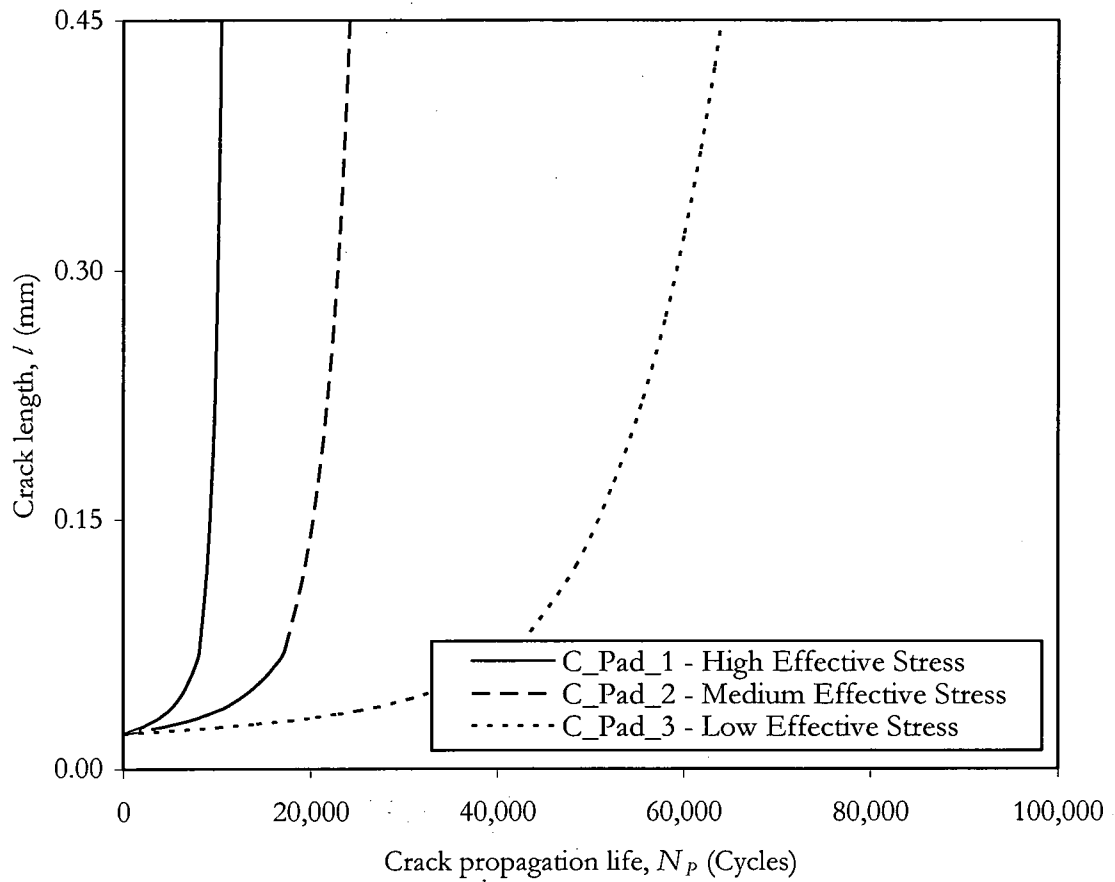


Figure 4.7 Crack propagation lives for the cylindrical pads. Initial crack length = 20 μm . $(\sigma_{eff})_{\text{High}} = 680 \text{ MPa}$, $(\sigma_{eff})_{\text{Medium}} = 408 \text{ MPa}$, $(\sigma_{eff})_{\text{Low}} = 250 \text{ MPa}$

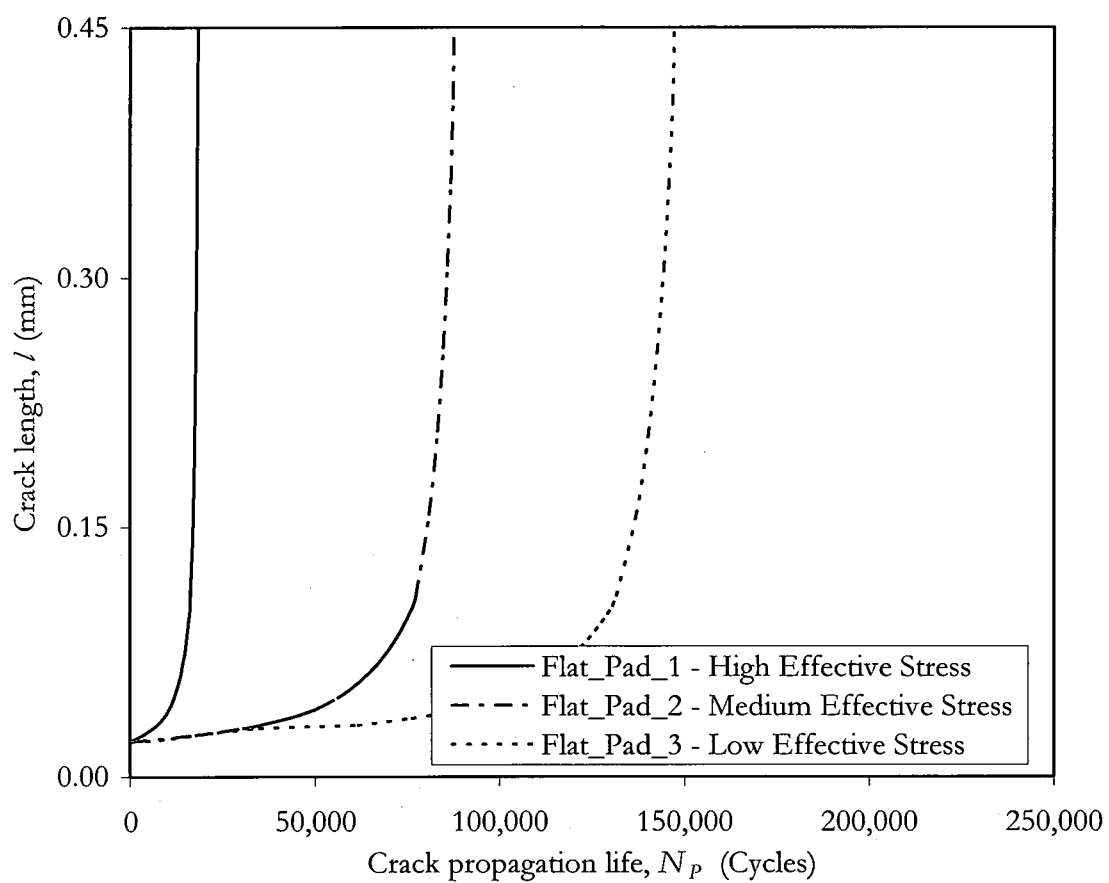


Figure 4.8 Crack propagation lives for the flat pads. Initial crack length = $20\text{ }\mu\text{m}$. $(\sigma_{eff})_{\text{High}} = 675\text{ MPa}$, $(\sigma_{eff})_{\text{Medium}} = 396\text{ MPa}$, $(\sigma_{eff})_{\text{Low}} = 327\text{ MPa}$.

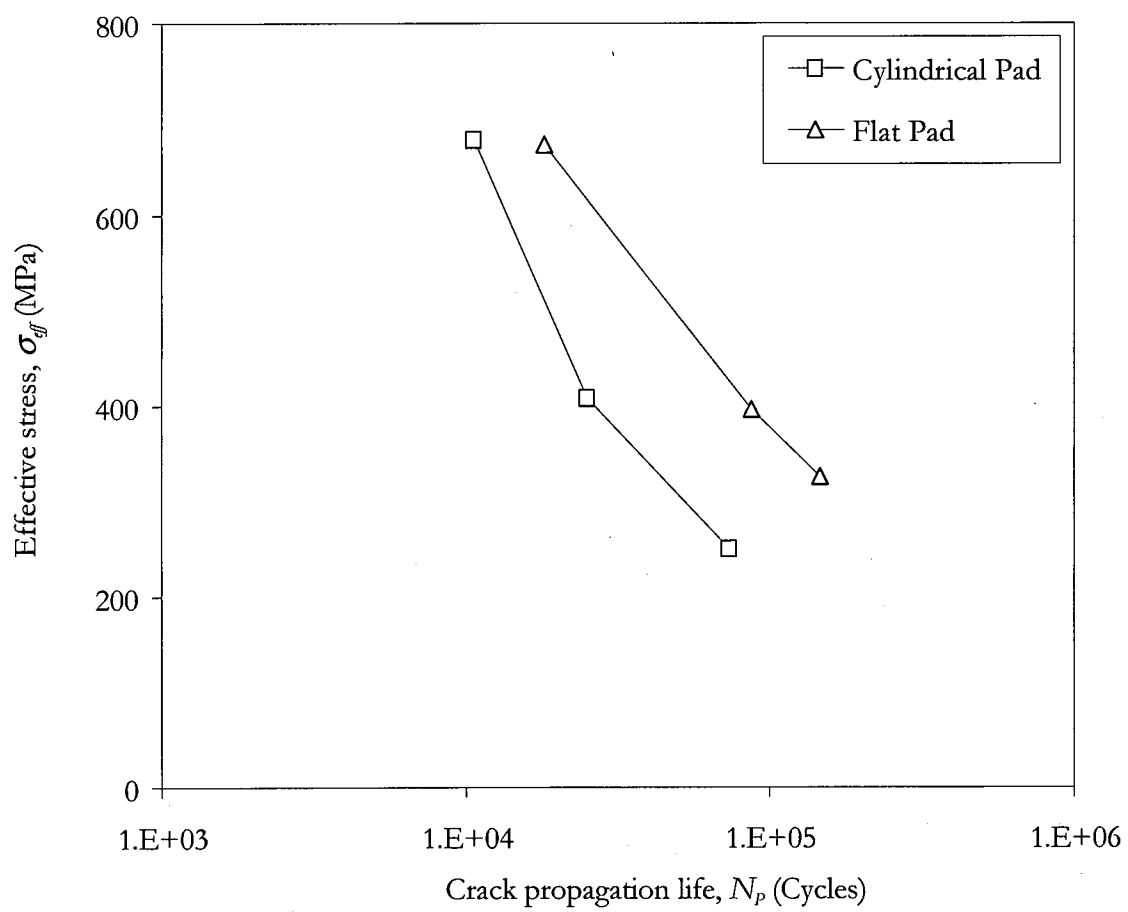


Figure 4.9 Crack propagation life as a function of the effective stress

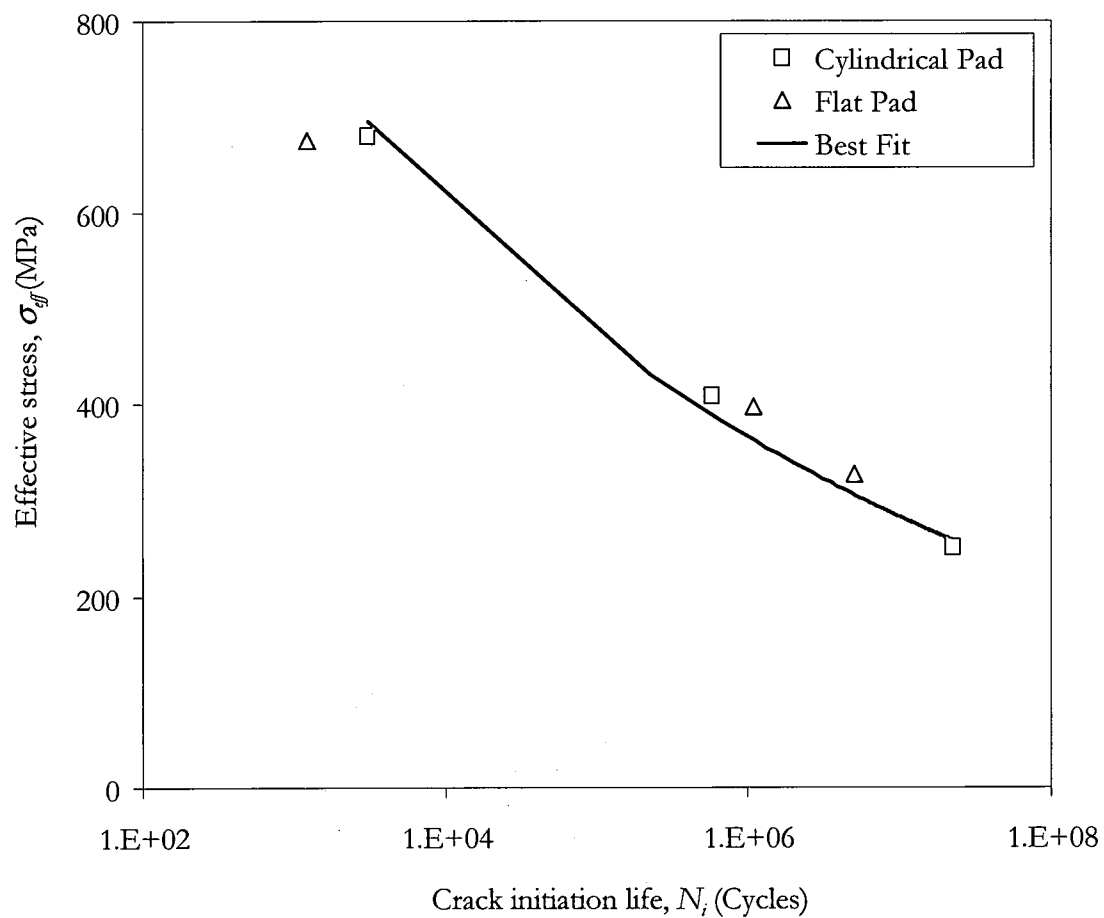


Figure 4.10 Crack initiation life as a function of the effective stress

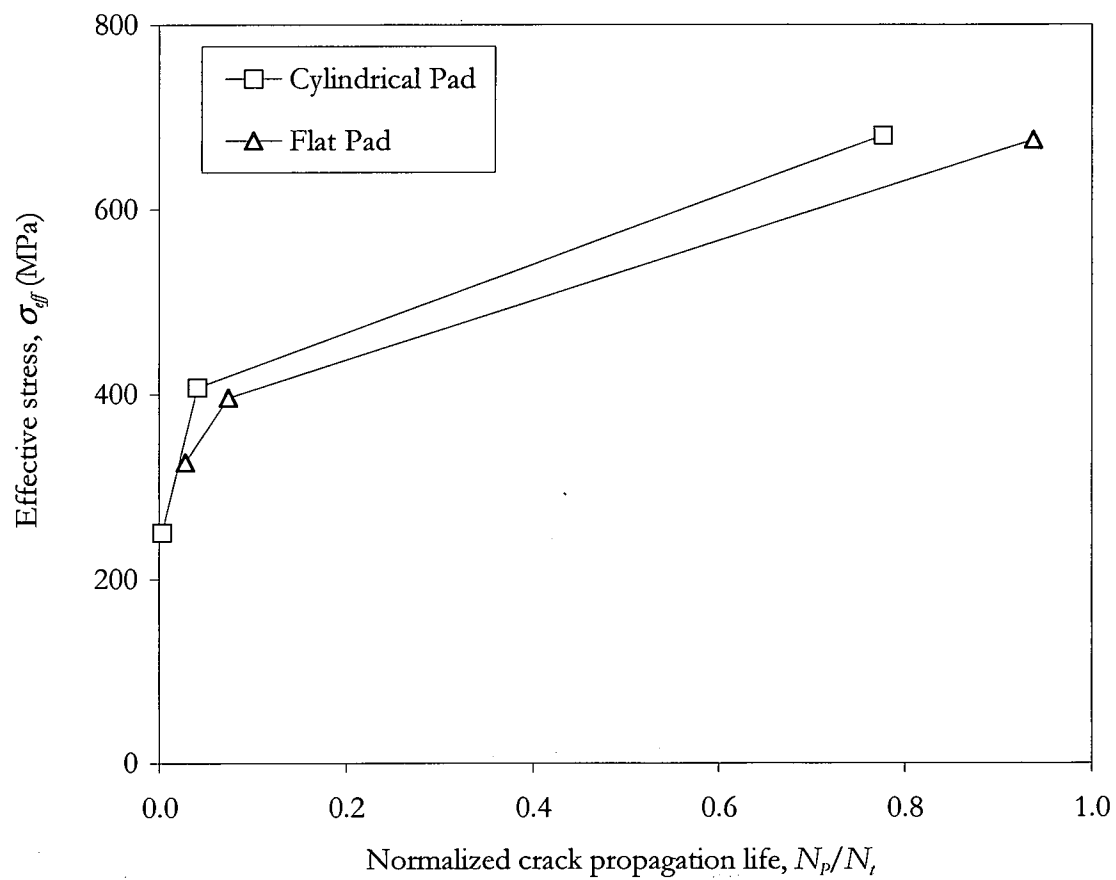


Figure 4.11 Normalized crack propagation life as a function of the effective stress

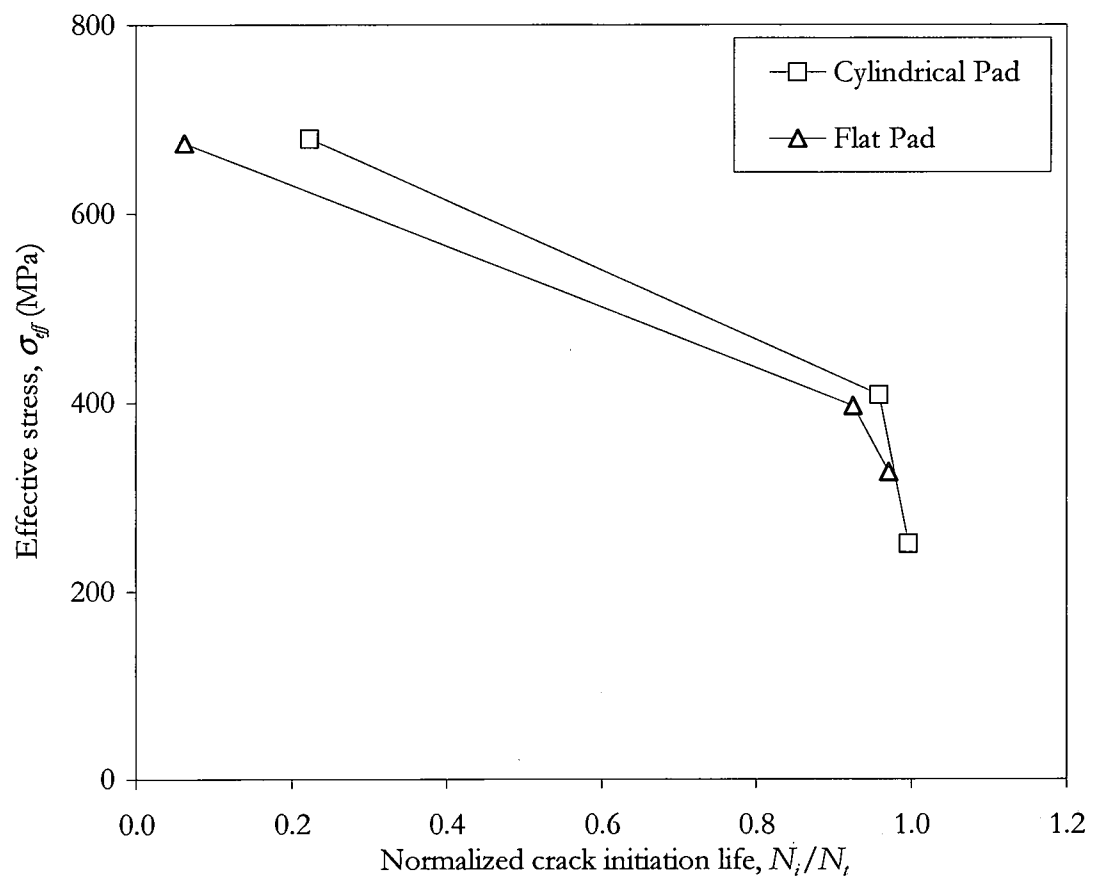


Figure 4.12 Normalized crack initiation life as a function of the effective stress

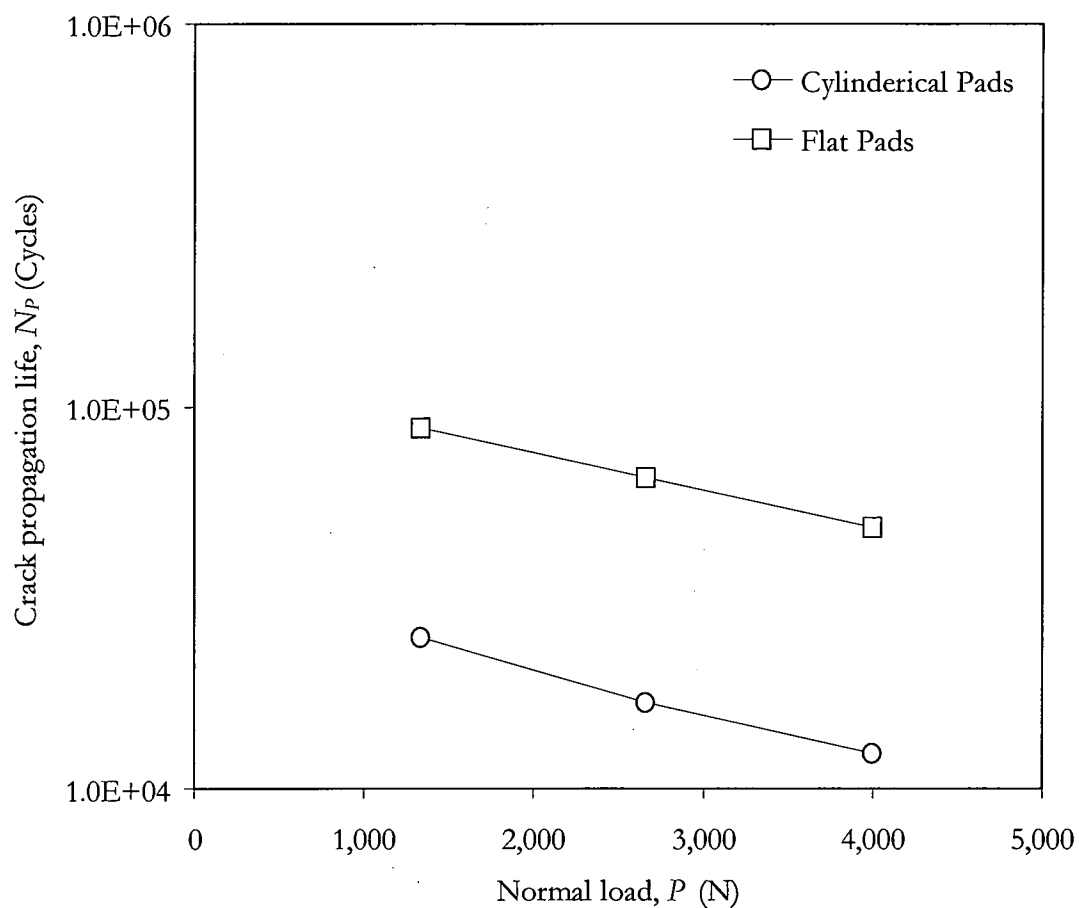


Figure 4.13 Crack propagation life as a function of the normal load. Initial crack length = 20 μm . Loading conditions: $\sigma_{\text{eff}} = 408$ MPa for the cylindrical pad, $\sigma_{\text{eff}} = 396$ MPa for the flat pad, $f = 0.5$, $Q/fP = 0.85$.

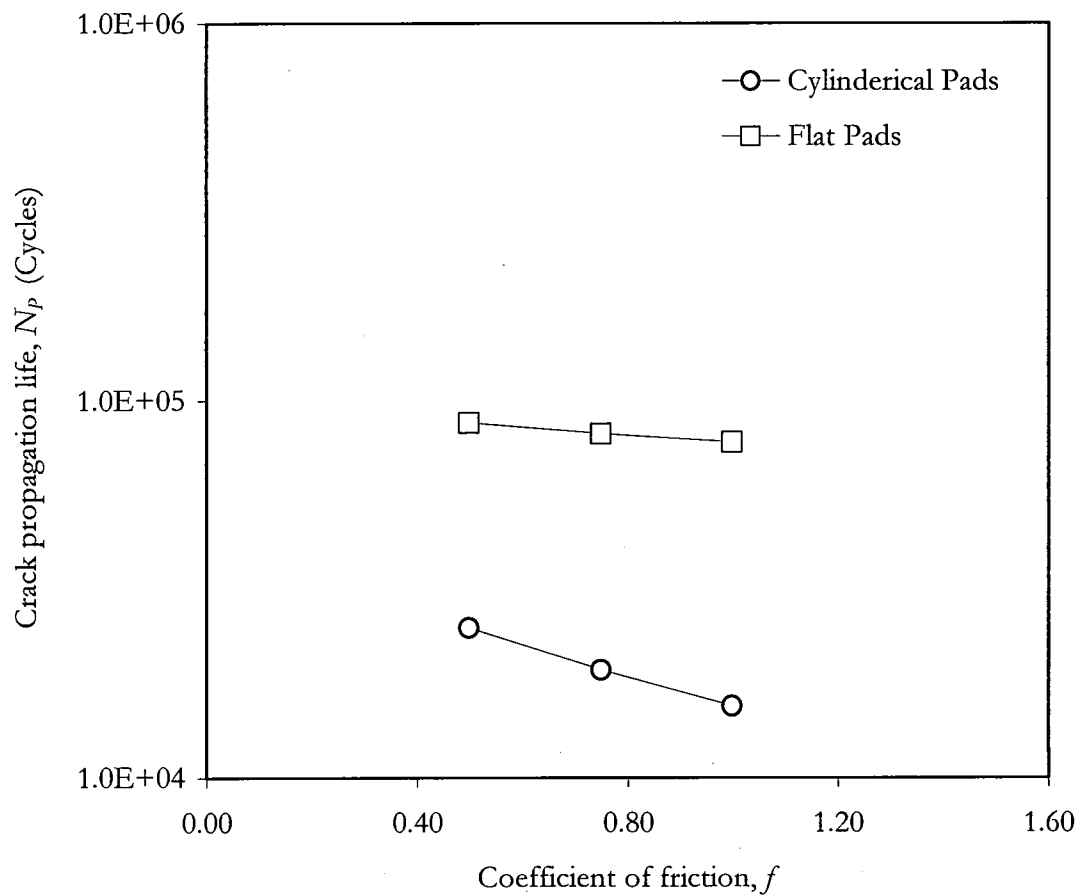


Figure 4.14 Crack propagation life as a function of coefficient of friction. Initial crack length = 20 μm . Loading conditions: $\sigma_{eff} = 408 \text{ MPa}$ for the cylindrical pad, $\sigma_{eff} = 396 \text{ MPa}$ for the flat pad, $P = 1335 \text{ N}$, $Q/fP = 0.85$

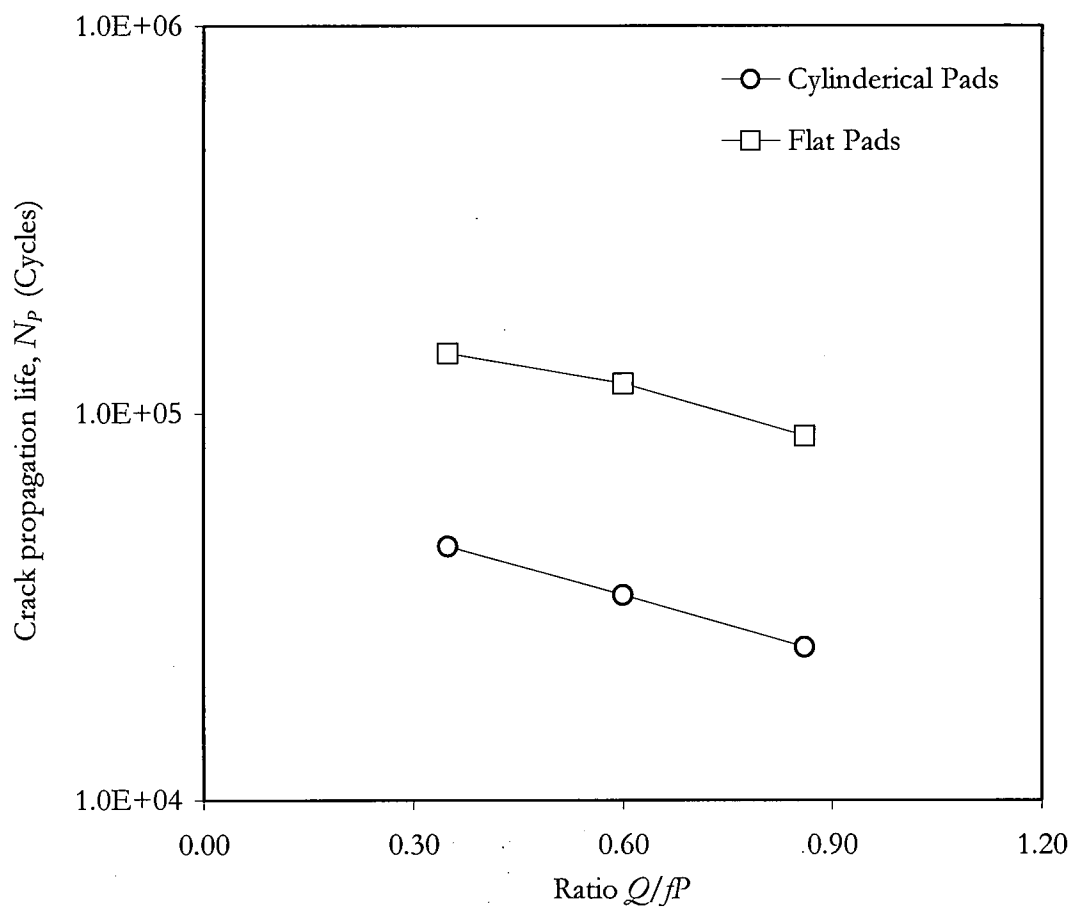


Figure 4.15 Crack propagation life as a function of ratio Q/fP . Initial crack length = 20 μm . Loading conditions: $\sigma_{eff} = 408$ MPa for the cylindrical pad, $\sigma_{eff} = 396$ MPa for the flat pad, $P = 1335$ N, $f = 0.5$

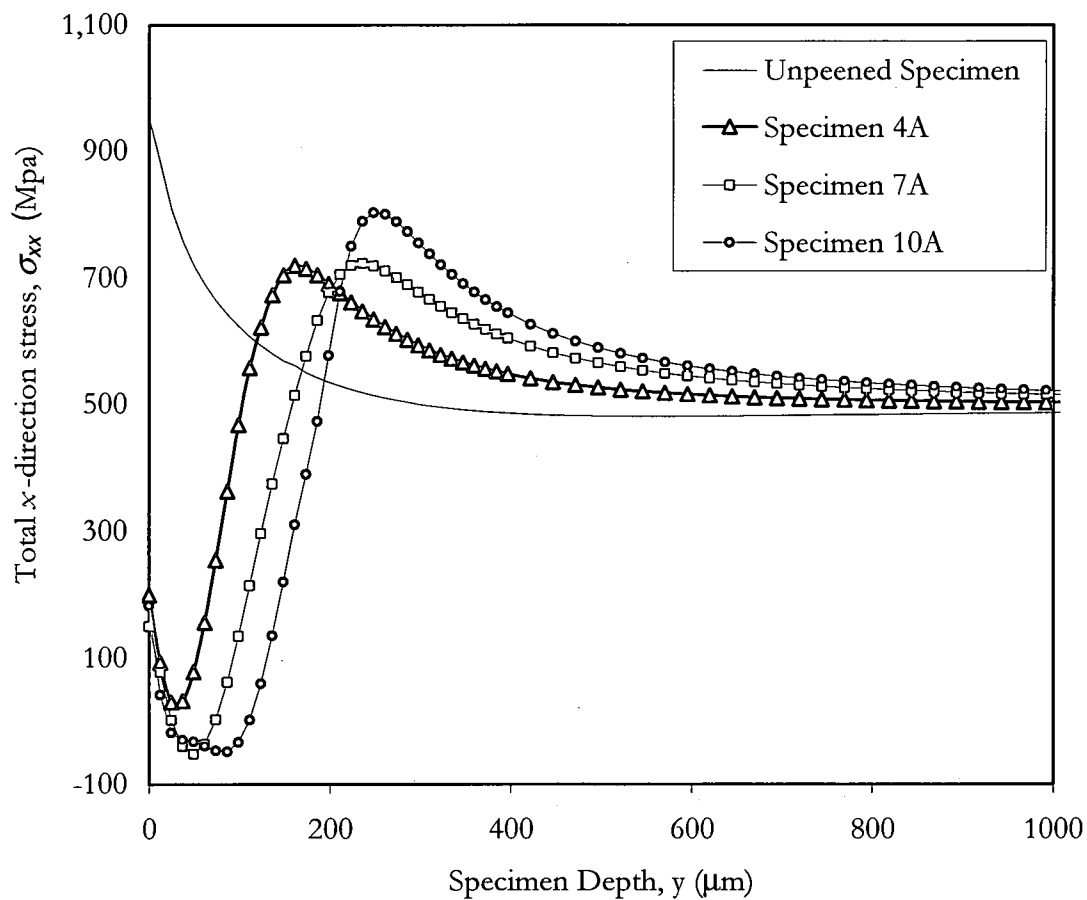


Figure 4.16 Total x -direction stress as a function of the specimen depth. Assumed residual stress relaxation = 0%.

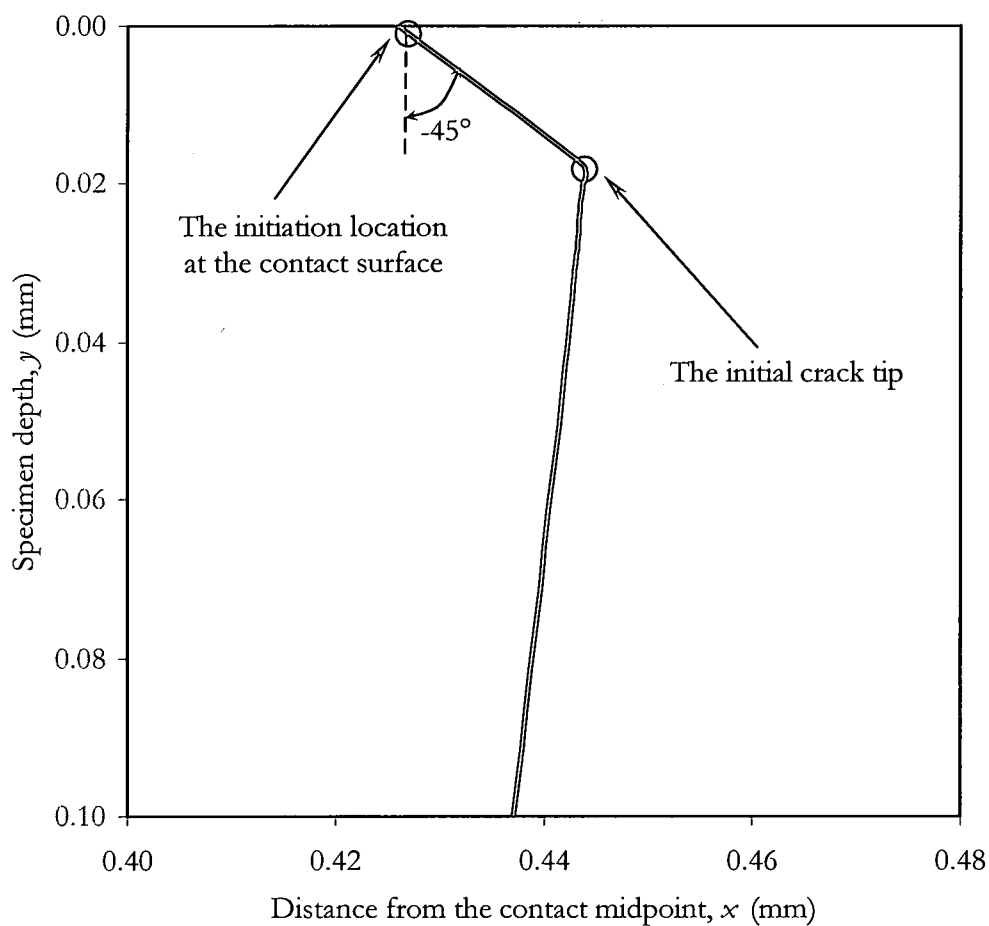


Figure 4.17 Crack trajectory in the unpeened specimen. Initial crack length = $25\text{ }\mu\text{m}$, specimen thickness = 6.4 mm , cylindrical pad radius = 50.8 mm . Loading conditions: $\Delta\sigma = 450\text{ MPa}$, $R = 0.1$, $\Delta Q = 2000\text{ N}$, $P = 1335\text{ N}$, $f = 1.0$

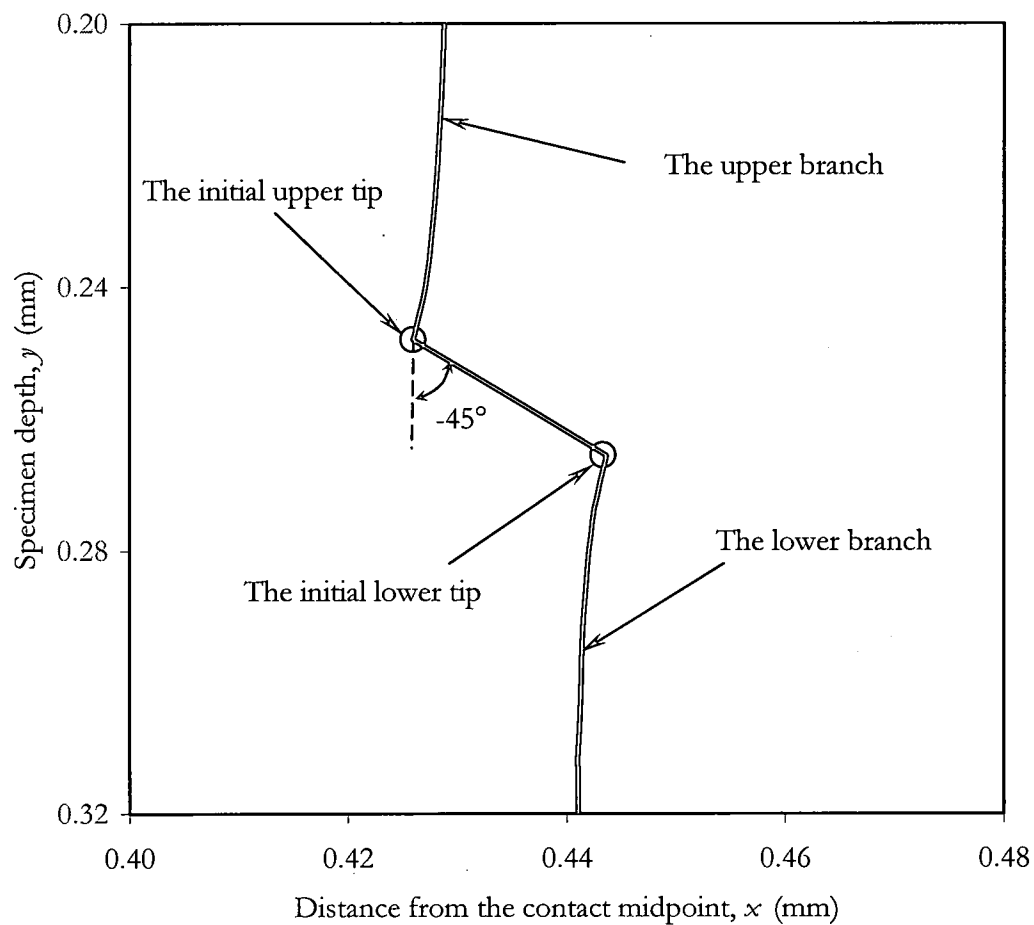


Figure 4.18 Crack trajectory in the shot-peened specimen with 10A with no residual stress relaxation. Initial crack length = $25\text{ }\mu\text{m}$ at an initiation location of $250\text{ }\mu\text{m}$ below the contact surface, specimen thickness = 6.4 mm , cylindrical pad radius = 50.8 mm . Loading conditions: $\Delta\sigma = 450\text{ MPa}$, $R = 0.1$, $\Delta Q = 2000\text{ N}$, $P = 1335\text{ N}$, $f = 1.0$.

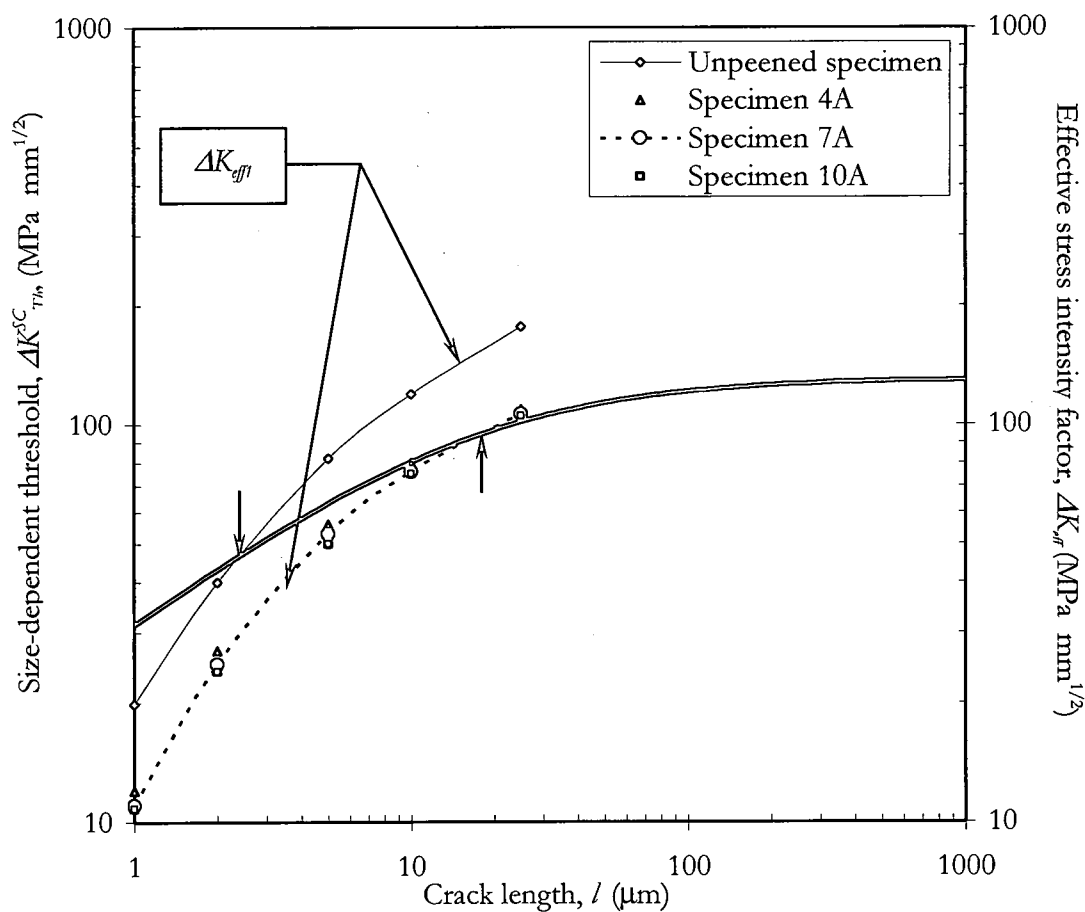


Figure 4.19 Estimation of the minimum initial crack length for the unpeened and shot-peened specimens. The assumed residual stress relaxation = 0%. Initial crack length = 25 μm at an initiation location of 170 μm below the contact surface for the 4A case, 235 μm for the 7A case, 250 μm for the 10A case, and at the contact surface for the unpeened case. Specimen thickness = 6.4 mm, cylindrical pad radius = 50.8 mm. Loading conditions: $\Delta\sigma = 450$ MPa, $R = 0.1$, $\Delta Q = 2000$ N, $P = 1335$ N, $f = 1.0$.

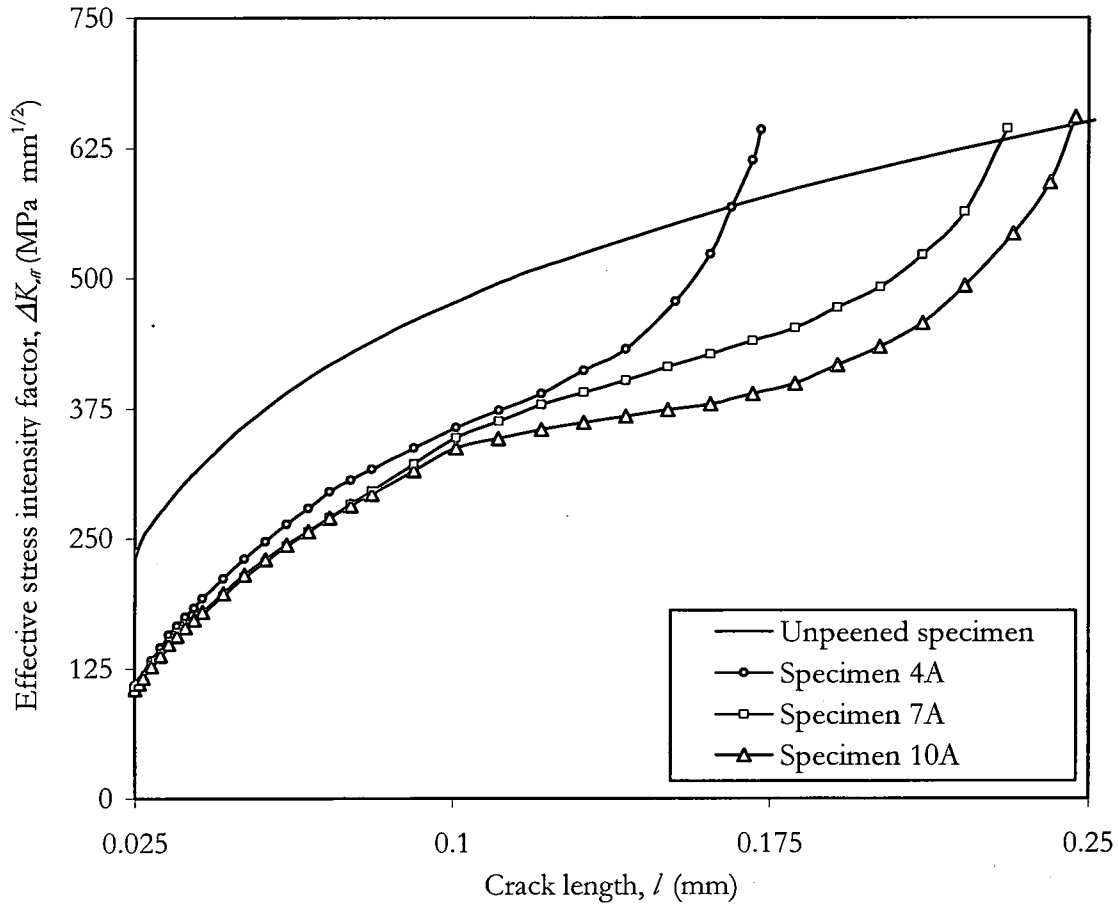


Figure 4.20 The effective stress intensity factor as a function of crack length and shot-peening intensity (upper branch). The assumed residual stress relaxation = 0%. Initial crack length = 25 μm at an initiation location of 170 μm below the contact surface for the 4A case, 235 μm for the 7A case, 250 μm for the 10A case, and at the contact surface for the unpeened case. Specimen thickness = 6.4 mm, cylindrical pad radius = 50.8 mm. Loading conditions: $\Delta\sigma = 450$ MPa, $R = 0.1$, $\Delta Q = 2000$ N, $P = 1335$ N, $f = 1.0$.

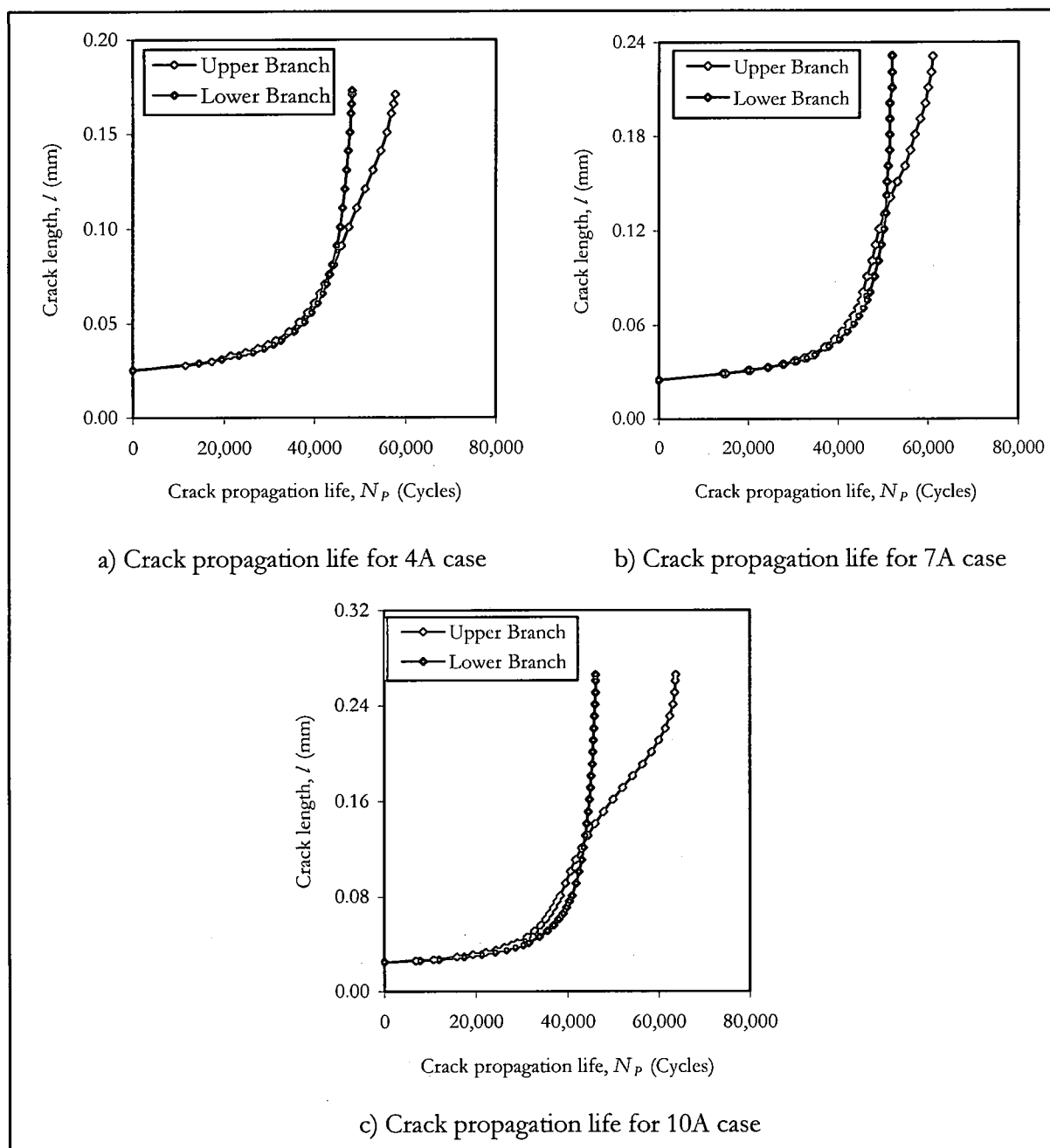


Figure 4.21 Crack propagation lives as a function of shot-peening intensity. The assumed residual stress relaxation = 0%. Initial crack length = 25 μm at an initiation location of 170 μm below the contact surface for the 4A case, 235 μm for the 7A case, and 250 μm for the 10A case. Specimen thickness = 6.4 mm, cylindrical pad radius = 50.8 mm. Loading conditions: $\Delta\sigma = 450$ MPa, $R = 0.1$, $\Delta Q = 2000$ N, $P = 1335$ N, $f = 1.0$.

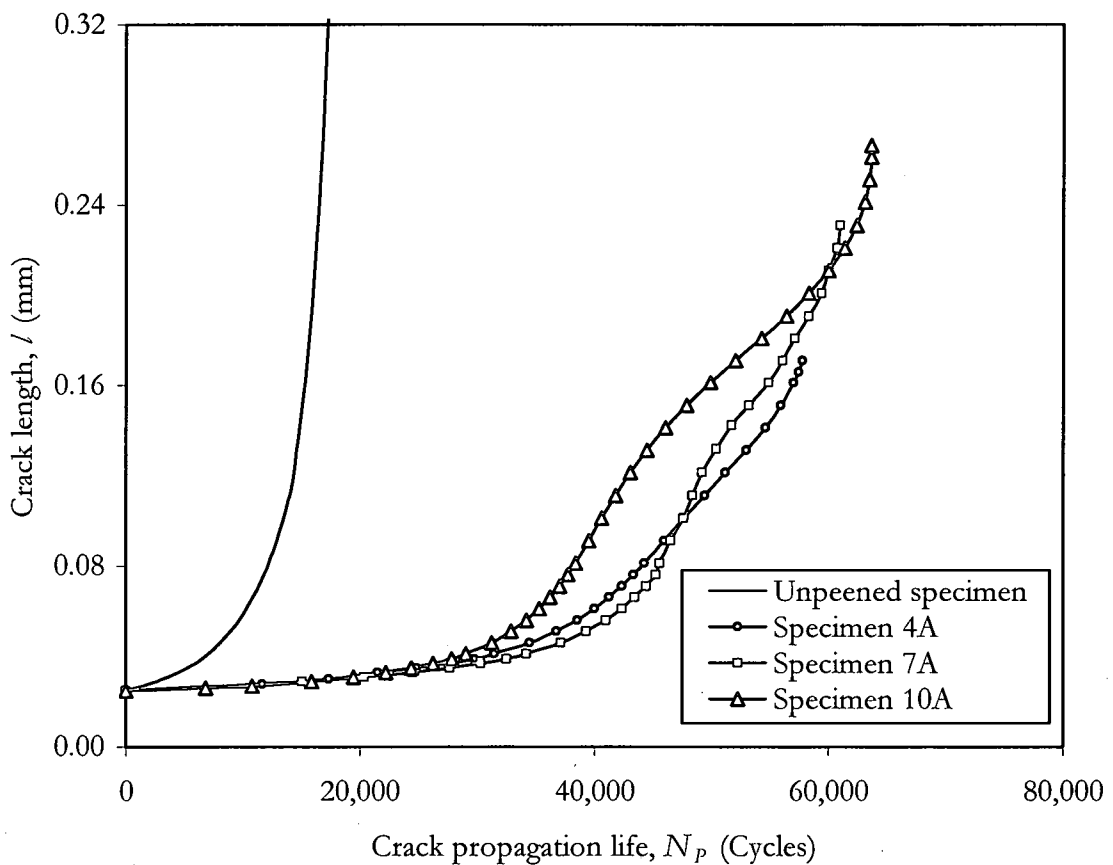


Figure 4.22 Comparison of the crack propagation lives of shot-peened specimens (upper branch) with the unpeened specimen. The assumed residual stress relaxation = 0%. Initial crack length = 25 μm at an initiation location of 170 μm below the contact surface for the 4A case, 235 μm for the 7A case, 250 μm for the 10A case, and at the contact surface for the unpeened case. Specimen thickness = 6.4 mm, cylindrical pad radius = 50.8 mm. Loading conditions: $\Delta\sigma = 450$ MPa, $R = 0.1$, $\Delta Q = 2000$ N, $P = 1335$ N, $f = 1.0$.

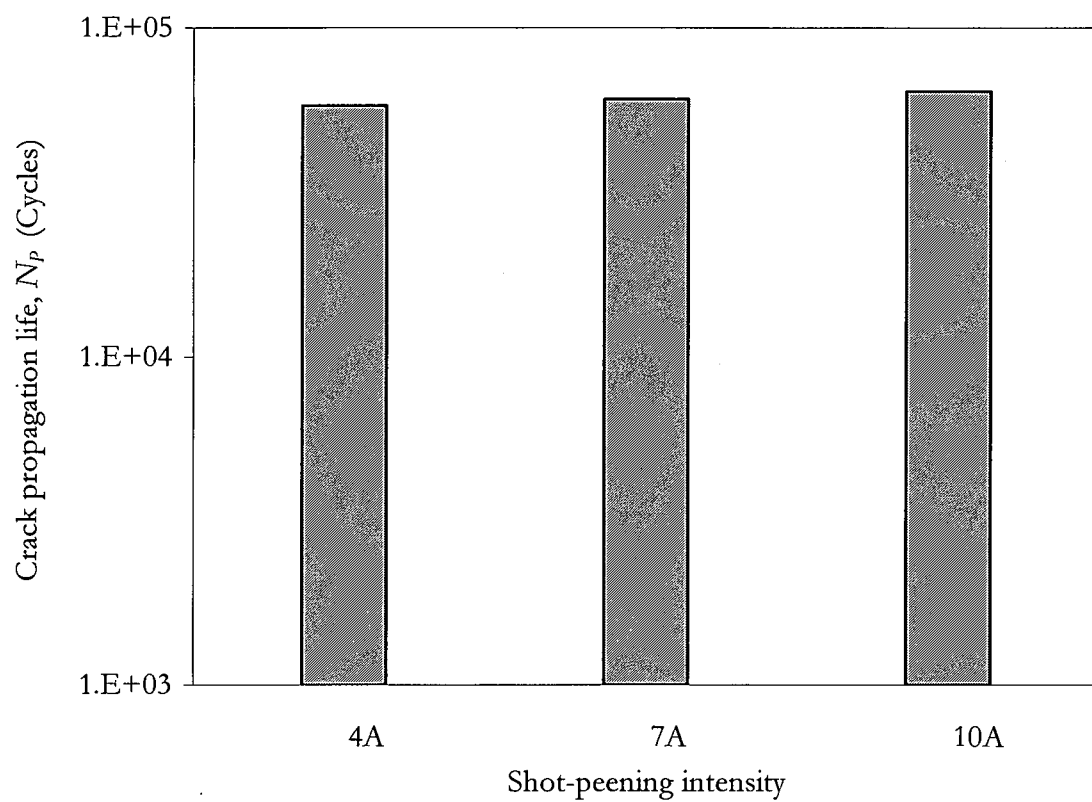


Figure 4.23 Variation of crack propagation life with shot-peening intensity

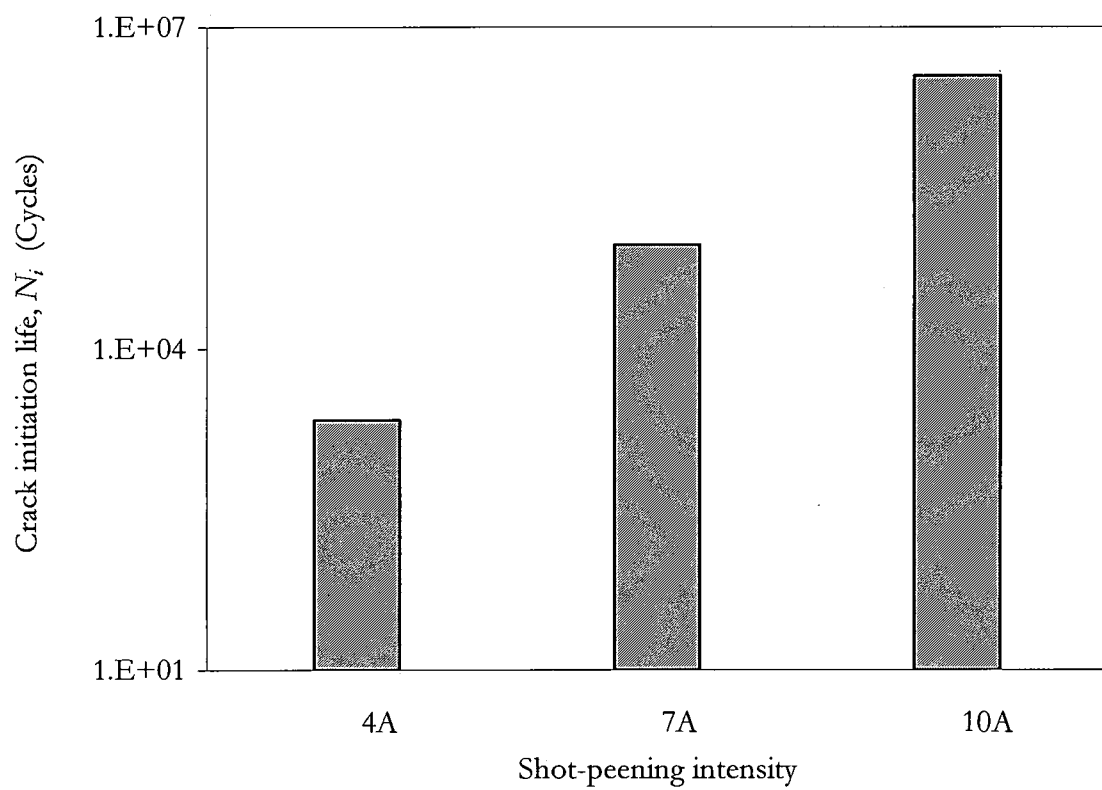


Figure 4.24 Variation of crack initiation life with shot-peening intensity

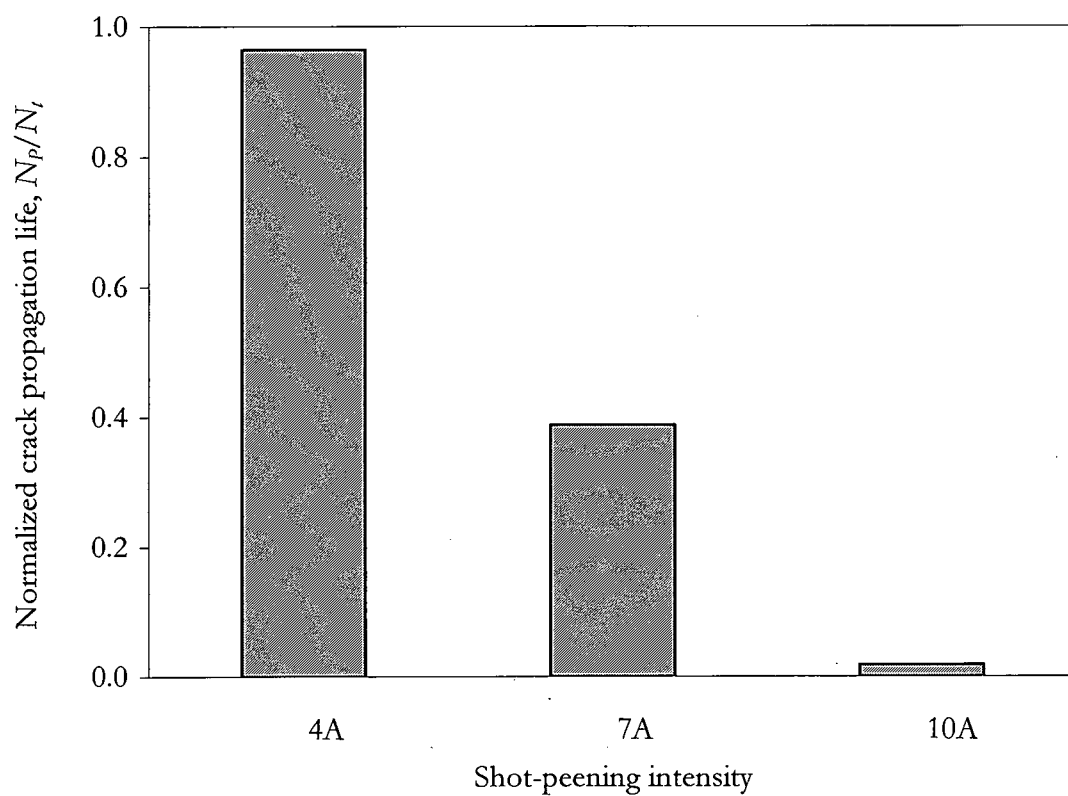


Figure 4.25 Variation of the normalized crack propagation life with shot-peening intensity

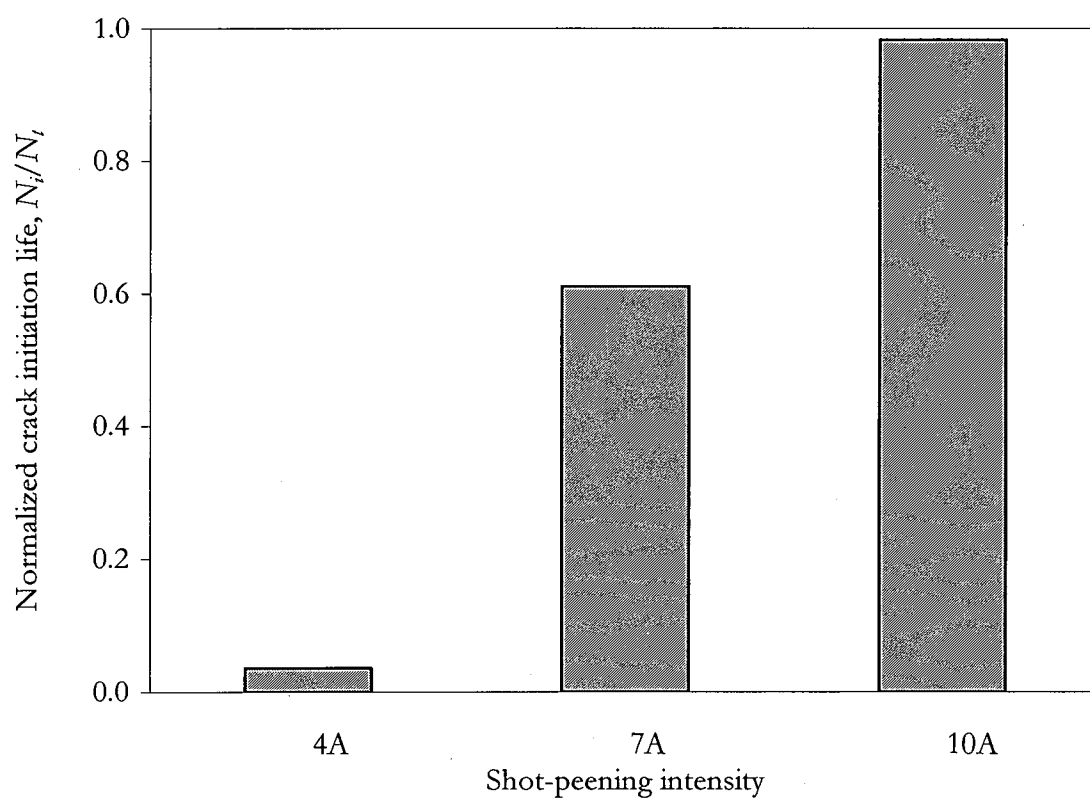


Figure 4.26 Variation of the normalized crack initiation life with shot-peening intensity

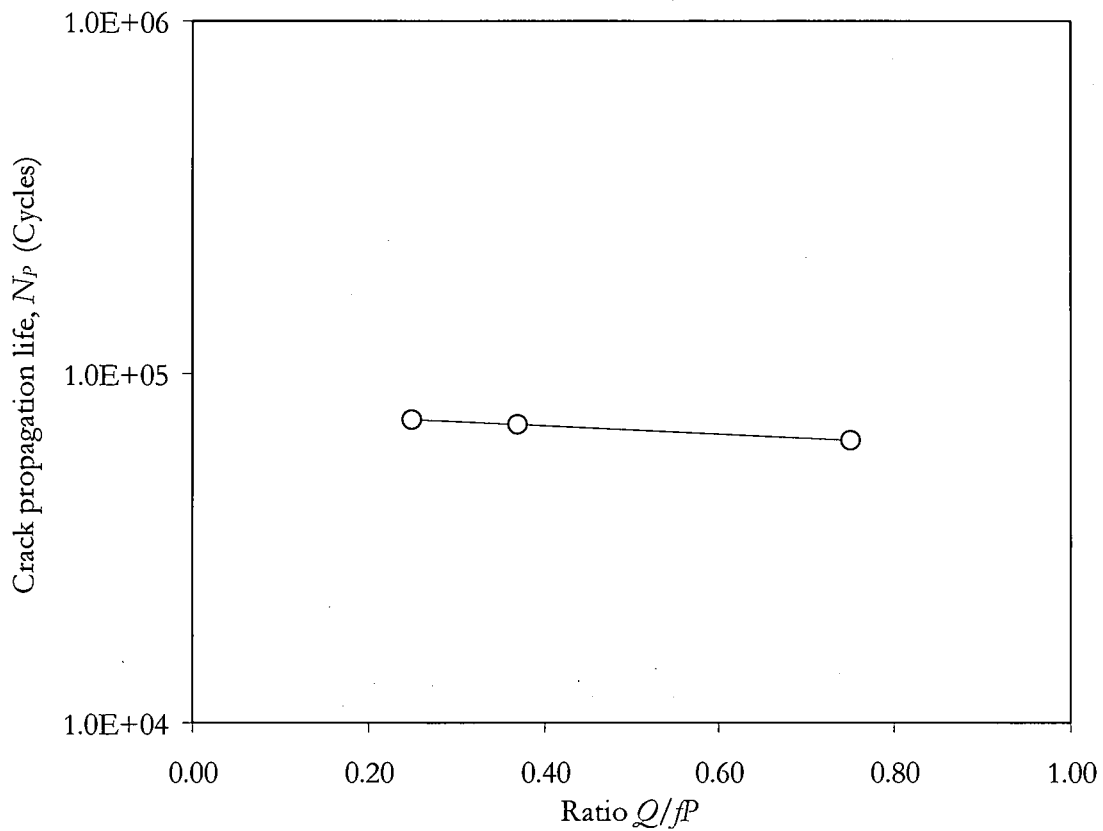


Figure 4.27 Crack propagation life as a function of ratio Q/fP in 10A shot-peened specimen. The assumed residual stress relaxation = 0%. Initial crack length = 25 μm at an initiation location of 250 μm below the contact surface, specimen thickness = 6.4 mm, cylindrical pad radius = 50.8 mm. The loading conditions: $\Delta\sigma = 450 \text{ MPa}$, $R = 0.1$, $\Delta Q = 2000 \text{ N}$, $f = 1.0$.

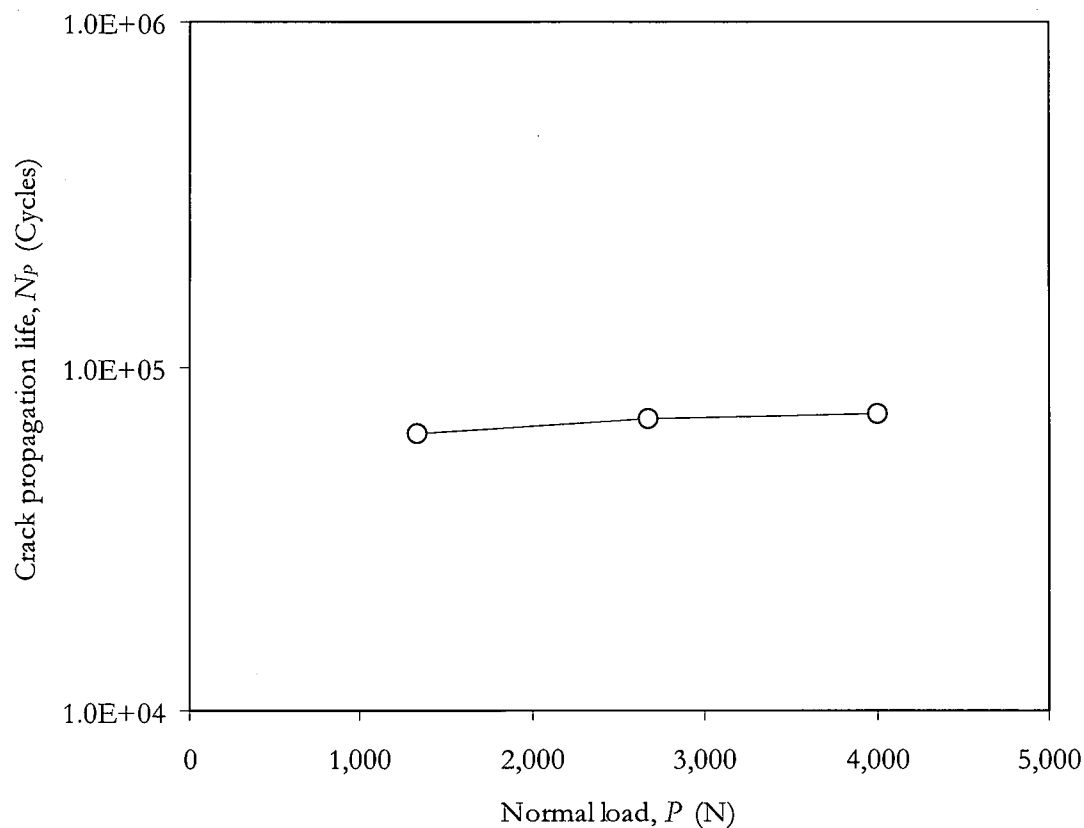


Figure 4.28 Crack propagation life as a function of the normal load in 10A shot-peened specimen. The assumed residual stress relaxation = 0%. Initial crack length = 25 μm at an initiation location of 250 μm below the contact surface, specimen thickness = 6.4 mm, cylindrical pad radius = 50.8 mm. The loading conditions: $\Delta\sigma = 450$ MPa, $R = 0.1$, $\Delta Q = 2000$ N, $f = 1.0$.

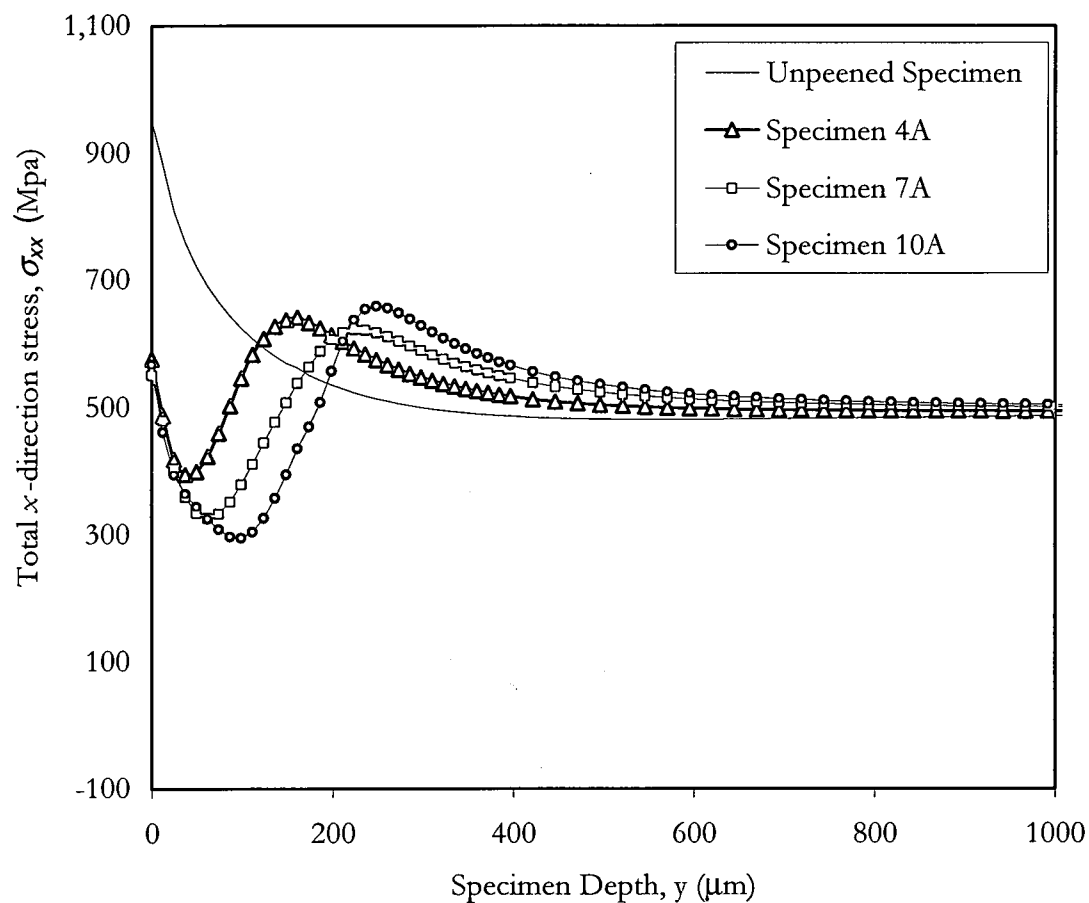


Figure 4.29 Total x -direction stress as a function of the specimen depth. The assumed residual stress relaxation = 50%.

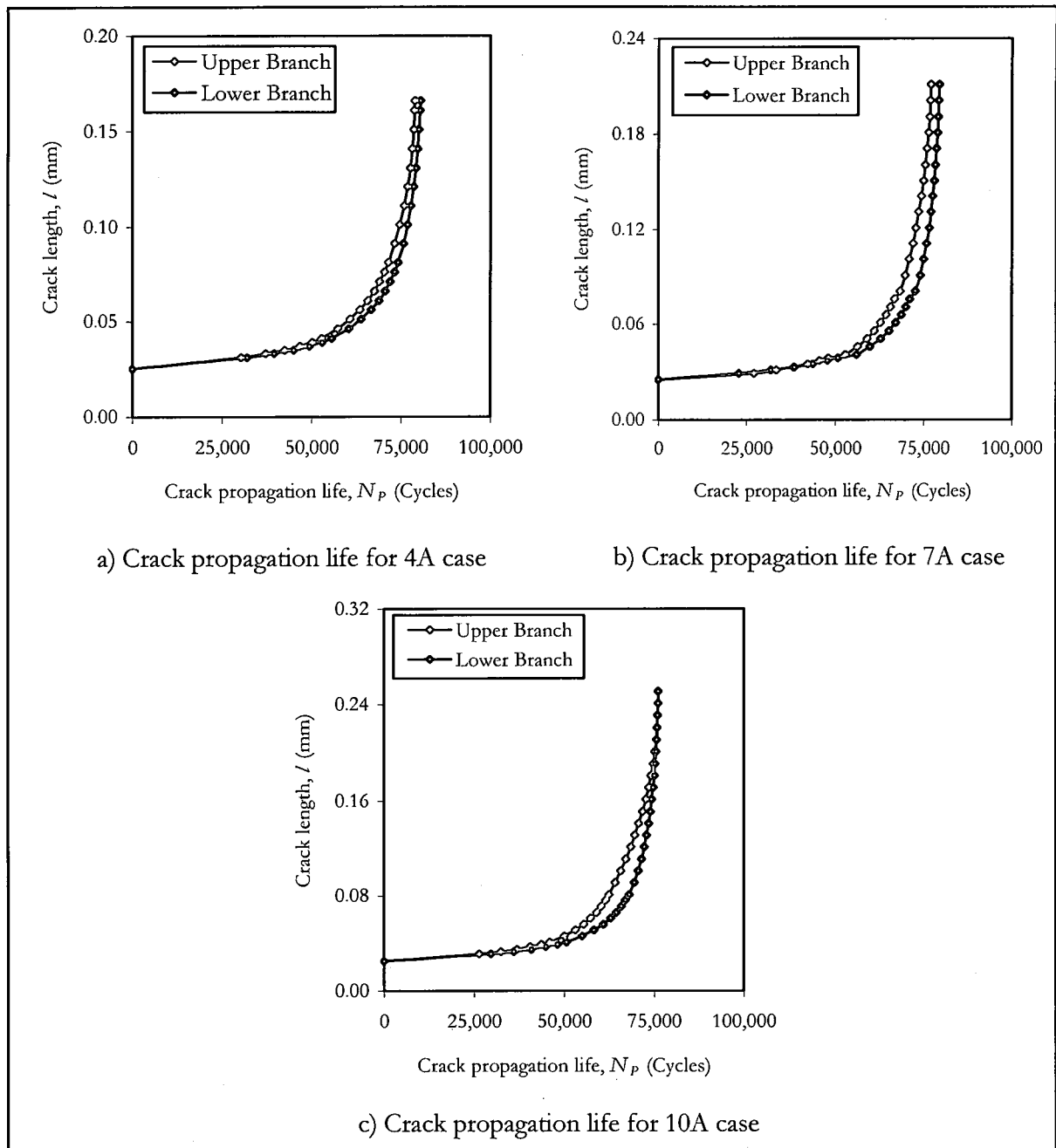


Figure 4.30 Crack propagation lives as a function of shot-peening intensity. The assumed residual stress relaxation = 50%. Initial crack length = $25\text{ }\mu\text{m}$ at an initiation location of $170\text{ }\mu\text{m}$ below the contact surface for the 4A case, $235\text{ }\mu\text{m}$ for the 7A case, and $250\text{ }\mu\text{m}$ for the 10A case. Specimen thickness = 6.4 mm , cylindrical pad radius = 50.8 mm . Loading conditions: $\Delta\sigma = 450\text{ MPa}$, $R = 0.1$, $\Delta Q = 2000\text{ N}$, $P = 1335\text{ N}$, $f = 1.0$.

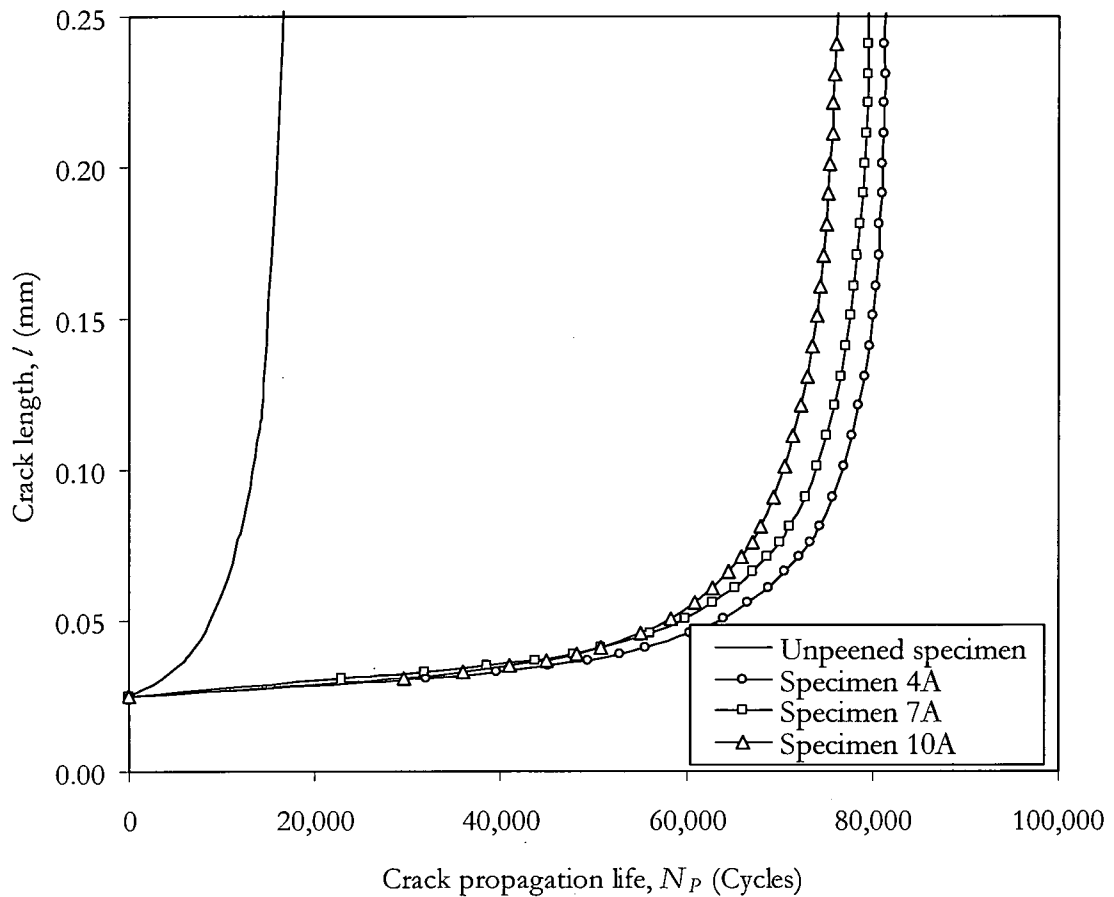


Figure 4.31 Comparison of the crack propagation lives of shot-peened specimens (lower branch) with the unpeened specimen. The assumed residual stress relaxation = 50%. Initial crack length = 25 μm at an initiation location of 170 μm below the contact surface for the 4A case, 235 μm for the 7A case, 250 μm for the 10A case, and at the contact surface for the unpeened case. Specimen thickness = 6.4 mm, cylindrical pad radius = 50.8 mm. Loading conditions: $\Delta\sigma = 450$ MPa, $R = 0.1$, $\Delta Q = 2000$ N, $P = 1335$ N, $f = 1.0$.

Table 4.1 Summary of the parameters involved in constructing Figures 4.1 and 4.2

Case	R	ΔK^{LC}_{Tb} (MPa mm ^{1/2})	l_o (μ m)
<i>C_Pad_1</i>	0.0	133	15.8
<i>C_Pad_2</i>	0.4	104	21.9
<i>C_Pad_3</i>	0.7	87	29.6
<i>Flat_Pad_1</i>	0.0	134	15.6
<i>Flat_Pad_2</i>	0.4	111	20.3
<i>Flat_Pad_3</i>	0.7	87	29.6

Table 4.2 Propagation life as a function of initial crack length

Case Name	l_o (μ m)	N_p (Cycles) For Initial Crack Length l_i				Experimental N_t (Cycles)
		20 μ m	30 μ m	50 μ m	80 μ m	
<i>C_Pad_1</i>	15.8	10,670	7,980	5,010	3,410	13,734
<i>C_Pad_2</i>	21.9	25,000	19,980	14,020	11,000	612,604
<i>C_Pad_3</i>	29.8	73,210	60,930	42,380	37,730	22,910,129
<i>Flat_Pad_1</i>	15.6	18,240	11,800	7,100	4,660	19,453
<i>Flat_Pad_2</i>	20.3	87,430	61,850	38,920	25,380	1,176,308
<i>Flat_Pad_3</i>	29.6	146,800	108,730	62,180	40,300	5,164,669

Table 4.3 Data used for the calculation of crack initiation life

Case Name	σ_{eff} (MPa)	Predicted N_P (Cycles)	Experimental N_t (Cycles)	Predicted $N_i = N_t - N_P$ (Cycles)	N_P/N_t	N_i/N_t
<i>C_Pad_1</i>	680	10,670	13,734	3,064	0.78	0.22
<i>C_Pad_2</i>	408	25,000	612,604	587,604	0.04	0.96
<i>C_Pad_3</i>	250	73,210	22,910,129	22,836,919	0.00	1.00
<i>Flat_Pad_1</i>	675	18,240	19,453	1,213	0.94	0.06
<i>Flat_Pad_2</i>	396	87,430	1,176,308	1,088,878	0.07	0.93
<i>Flat_Pad_3</i>	327	146,800	5,164,669	5,017,869	0.03	0.97

Table 4.4 Data used for the parametric study

	P (N)		Life Difference (Cycles)
	1335 N	4005 N	
N_P (Cycles) – Cylindrical Pads	25,000	12,350	12,660
N_P (Cycles) – Flat Pads	87,430	48,330	39,104
	f		Life Difference (Cycles)
	0.5	1.0	
N_P (Cycles) – Cylindrical Pads	25,000	15,430	9,574
N_P (Cycles) – Flat Pads	87,430	77,770	9,655
	Q/fP		Life Difference (Cycles)
	0.35	0.85	
N_P (Cycles) – Cylindrical Pads	45,410	25,000	20,402
N_P (Cycles) – Flat Pads	142,480	87,430	55,053

CHAPTER V

CONCLUSIONS AND RECOMMENDATIONS FOR FUTURE WORK

5.1 Conclusions

The propagation behavior of fretting fatigue cracks in the titanium alloy, Ti-6Al-4, has been studied. The effects of the normal load P , the coefficient of friction f , the ratio Q/fP , the cyclic axial stress, and the fretting pad geometry on the crack initiation and propagation have been investigated. The effective axial stress was used as the major loading factor instead of the cyclic axial stress. Three levels of the effective stress were used for two different fretting pads (cylindrical and flat) while keeping all the remaining factors constant. These were categorized as high, medium, and low. Later on, the medium level of effective stress, for both types of fretting pads, was chosen as the base line to investigate the effects of the other fretting fatigue parameters. The fretting cracks initiation lives for these cases were then quantified by subtracting the estimated propagation lives from the failure lives obtained from a previous experimental study involving the same loading conditions and the same types of pads. In addition, the effects of shot-peening on the growth behavior of fretting cracks have also been investigated. The effects of three different shot-peening intensities namely 4A, 7A, and 10A (with 100% surface coverage) were evaluated. The crack propagation analysis results of the shot-peening cases were compared to a previous experimental study involving the same loading conditions and the same shot-peening intensities. Two finite element analysis codes, ABAQUS and ANSYS, were used to evaluate the stress, strain, and displacement fields for all the investigated fretting

fatigue cases. Finite element sub-modeling technique was used to achieve more accurate stress, strain, and displacement fields and to reduce the finite element computation time. The crack propagation analysis was performed by the fracture mechanics code FRANC2D/FRANC2D-L. The code was used to calculate the stress intensity factors along the fretting crack path with the corresponding crack lengths. Then, an advanced crack growth model was used to estimate the crack propagation life. The following conclusions can be made based on this work:

1. The crack propagation and initiation lives were found to decrease as the effective axial stress σ_{eff} increases.
2. As the normal load P increases, the crack propagation life decreases for the unpeened specimens.
3. Similarly, as the friction force Q increases, crack propagation life decreases.
4. The value of the ratio Q/fP indicates the size of the stick zone. As the ratio Q/fP increases, the crack propagation life decreases; i.e. the crack propagation life decreases as the stick zone gets smaller.
5. The crack propagation life decreases as the friction coefficient f increases.
6. The crack propagation life was found to be higher for flat pads than for the cylindrical pads under identical loading conditions.
7. Among all the loading factors, the effective axial stress was found to be the dominant factor that affects the fretting crack propagation life followed by the ratio Q/fP , then the normal load P . The friction coefficient has the least effect on the fretting crack propagation life.

8. As the shot-peening intensity increases, the size of the compressive residual stress zone increases, which leads to a compensatory tensile stress zone with a higher peak.
9. The shot-peening treatment improved the crack propagation life.
10. For all the shot-peening intensities, the fretting cracks were found to initiate at a depth below the surface in the specimen when a 0% stress relaxation is assumed. This depth was found to coincide with the location of the maximum tensile stress.
11. For 50% stress relaxation, the possibility for the crack to initiate at the surface became high. However, the location of the maximum tensile stress was still located at a depth in the specimen.
12. For 50% stress relaxation, the crack propagation life was found to be around 10,000 cycles higher than for the 0% stress relaxation case.
13. By combining the crack propagation lives of this study with the experimental results of a previous study involving the same loading conditions and the same shot-peening intensities, it was found that the shot-peening intensity has no significant effect on the propagation behavior of the fretting cracks. The normalized crack initiation life increases, while the normalized propagation life decreases.
14. The propagation life was found to decrease as the ratio Q/P increases in shot-peened specimen with 10A intensity; while the propagation life increases with the normal load P .

5.2 Recommendations for Future Work

The following recommendations are made for future work:

1. Perform a 3D finite element analysis to better understand the overall fretting problem instead of 2D analysis.
2. Study the effects of using other fretting pad geometries on the propagation behavior of fretting fatigue cracks. Some of these pad geometries are: spherical, cylindrical with different radii of curvatures.
3. Study the effect of different initial crack orientations other than -45° .

APPENDIX A

Evaluating the Experimental Data

This appendix explains the procedure used in the evaluation of the experimental data used in the study of the effect of the cyclic bulk stress on the propagation behavior of the fretting fatigue cracks. The original experimental data were developed by Lykins [19] in his dissertation. Figures A.1 and A.2 show the experimental data and their best fits for the cylindrical and flat pads cases, respectively. In these two plots, the experimental total fretting fatigue lives were plotted against the effective stress, σ_{eff} . Tables A.1 and A.2 summarize all of these data.

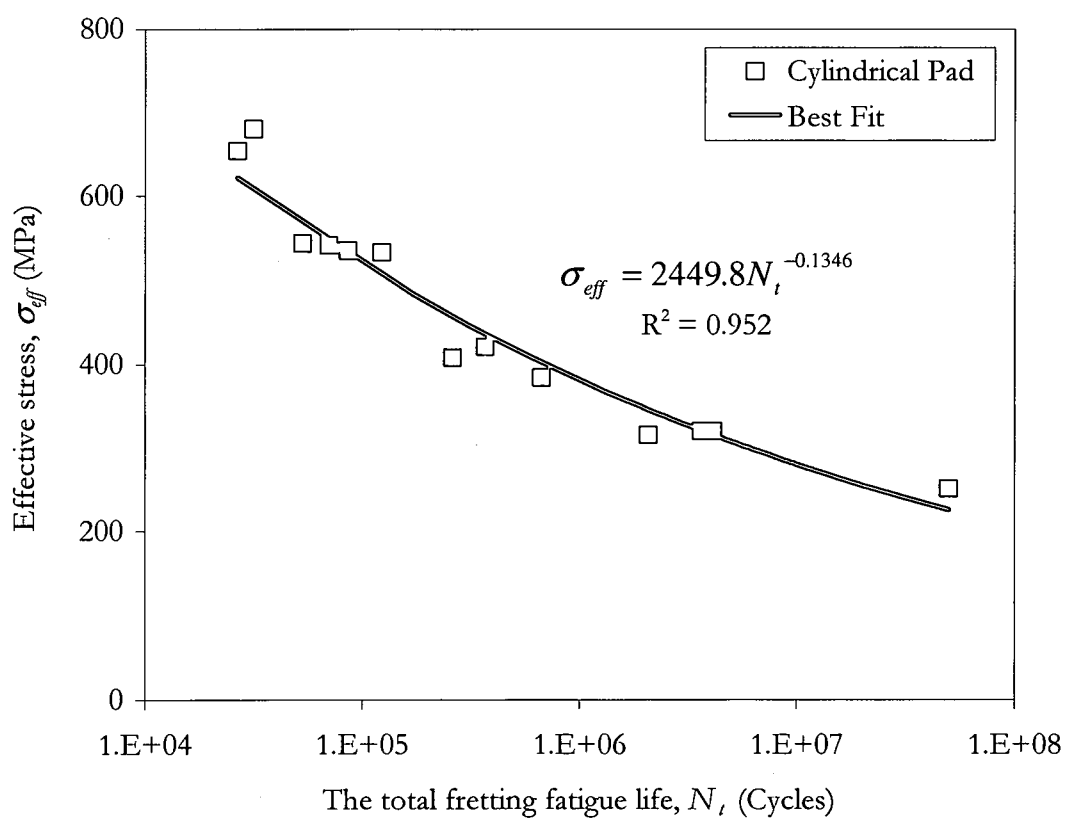


Figure A.1 The total fretting fatigue life as a function of the effective stress (cylindrical pad)

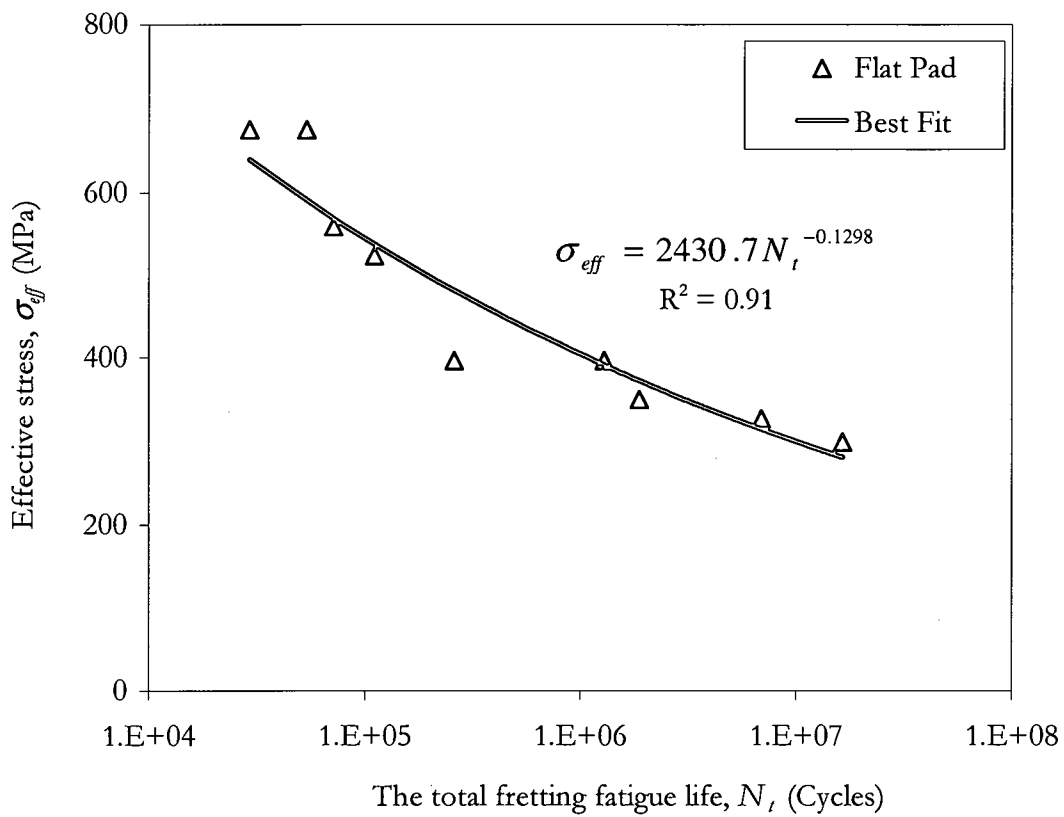


Figure A.2 The total fretting fatigue life as a function of the effective stress (flat pad)

Table A.1 Experimental fretting fatigue lives for the cylindrical pad case

Case #	σ_{max} (MPa)	σ_{min} (MPa)	$\Delta\sigma$ (MPa)	σ_{eff} (MPa)	P (N)	N_i (Cycles)	N_i (Best Fit) (Cycles)
1	636	-40	675	653	1,335	26,700	18,387
2	700	44	656	680		31,600	13,734
3	552	18	534	544		53,400	71,988
4	566	53	513	542		70,600	74,063
5	687	291	396	536		86,200	80,229
6	686	294	392	533		124,000	83,412
7	529	232	297	408		262,000	612,604
8	687	456	231	420		371,000	486,551
9	582	351	231	384		672,000	952,441
10	413	186	227	315		2,080,000	4,133,061
11	420	191	229	320		3,660,000	3,734,129
12	540	372	168	319		4,140,000	3,745,359
13	410	273	137	250		50,000,000	22,910,129

Table A.2 Experimental fretting fatigue lives for the flat pad case

Case #	σ_{max} (MPa)	σ_{min} (MPa)	$\Delta\sigma$ (MPa)	σ_{eff} (MPa)	P (N)	N_t (Cycles)	N_t (Best Fit) (Cycles)
1	692	37	655	675	1,335	29,300	19,334
2	691	36	655	675		54,000	19,453
3	574	32	542	559		71,600	82,316
4	696	326	370	524		111,000	136,658
5	484	174	310	396		260,000	1,176,308
6	613	381	232	396		1,300,000	1,180,591
7	556	357	199	350		1,890,000	3,038,887
8	535	356	179	327		6,930,000	5,164,669
9	394	181	213	299		16,500,000	10,331,355

APPENDIX B

Typical ABAQUS Input File

```
*HEADING
FRETTING FATIGUE CONTACT ANALYSIS WITH FLAT PAD
**
** UNITS: IN, LPF
*PRE PRINT, MODEL=NO, ECHO=NO, HISTORY=NO
*NODE
1001, -0.75, 0.
1065, -0.241421356, 0.
1193, -0.1, 0.
1321, 0.1, 0.
1449, 0.241421356, 0.
1513, 0.75, 0.
**
** CREATE BOTTOM OF PLATE
*NGEN, NSET=NPBOT
1001, 1065
1065, 1193
1193, 1321
1321, 1449
1449, 1513
** CREATE TOP OF PLATE
*NCOPY, CHANGE NUMBER=256000, OLD SET=NPBOT, NEW SET=NPTOP, SHIFT
0., 0.0375
0., 0., 0., 0., 0., 1., 0.
** CREATE NEAR TOP(0.02013 INCH FROM TOP) OF PLATE
*NCOPY, CHANGE NUMBER=238000, OLD SET=NPBOT, NEW SET=NPTOP1, SHIFT
0., 0.01737
0., 0., 0., 0., 0., 1., 0.
** CREAT NODES BETWEEN NPBOT AND NPTOP1 NODES OF PLATE
*NFill, NSET=NPLATE
NPBOT, NPTOP1, 238, 1000
**CREAT NODES BETWEEN NPTOP1 AND NPTOP NODES OF PLATE
*NFill, NSET=NPLATE
NPTOP1, NPTOP, 18, 1000
**
** CREATE PLATE MESH WITH PLANE STRAIN ELEMENTS
*ELEMENT, TYPE=CPE4
1001, 256001, 256002, 257002, 257001
** CREATE 512 ELEMENTS (1-512) ALONG X AXIS AND 32 LAYERS ALONG Y-AXIS
*ELGEN, ELSET=EPLATE1
1001, 512, 1, 1, 32, -1000, 1000
*ELEMENT, TYPE=CPE4
```

```

33001, 223001, 223003, 225003, 225001
** CREATE 256 ELEMENTS (1-256) ALONG X AXIS AND 48 LAYERS ALONG Y-AXIS
*ELGEN, ELSET=EPLATE2
33001, 256, 2, 1, 48, -2000, 1000
*ELEMENT, TYPE=CPE4
81001, 125001, 125005, 129005, 129001
** CREATE 128 ELEMENTS (1-128) ALONG X AXIS AND 32 LAYERS ALONG Y-AXIS
*ELGEN, ELSET=EPLATE3
81001, 128, 4, 1, 32, -4000, 1000
*ELSET, ELSET=ELPLATE
EPLATE1, EPLATE2, EPLATE3
*NSET, NSET=INDEPA, GENERATE
225001, 225511, 2
*NSET, NSET=INDEPB, GENERATE
225003, 225513, 2
*NSET, NSET=INDP, GENERATE
225002, 225512, 2
*NSET, NSET=INDEPA1, GENERATE
129001, 129509, 4
*NSET, NSET=INDEPB1, GENERATE
129005, 129513, 4
*NSET, NSET=INDP1, GENERATE
129003, 129511, 4
*MPC
LINEAR, INDP, INDEPA, INDEPB
LINEAR, INDP1, INDEPA1, INDEPB1
*SOLID SECTION, ELSET=ELPLATE, MATERIAL=TI64
0.25,
*MATERIAL, NAME=TI64
*ELASTIC, TYPE=ISO
1.83E7, 0.32
**
**
** CREATE CYLINDER
*NODE, NSET=NCBOT1
258001, -0.3, 0.2375
*NODE, NSET=NCBOT4
258065, -0.241421356, 0.096078643
*NODE, NSET=NCBOT2
258193, -0.1, 0.0375
*NODE, NSET=NCBOT0
258257, 0.0, 0.0375
*NODE, NSET=NCBOT3
258321, 0.1, 0.0375
*NODE, NSET=NCBOT5
258449, 0.241421356, 0.096078643
*NODE, NSET=NCBOT
258001, -0.3, 0.2375
*NODE
514065, -0.241421356, 0.45
514193, -0.1, 0.45
514321, 0.1, 0.45
514001, -0.3, 0.45
514449, 0.241421356, 0.45
514513, 0.3, 0.45

```

```

** CREATE TOP OF CYLINDER
*NGEN,NSET=NCTOP
514001,514065
514065,514193
514193,514321
514321,514449
514449,514513
** CREATE BOTTOM OF CYLINDER
*NCOPY, CHANGE NUMBER=1, OLD SET=NCBOT1, NEW SET=NCBOT, SHIFT, MULTIPLE=64
0., 0., 0.
-0.1, 0.2375, 0., -0.1, 0.2375, 1., 0.703125
*NCOPY, CHANGE NUMBER=1, OLD SET=NCBOT4, NEW SET=NCBOT, SHIFT, MULTIPLE=128
0., 0., 0.
-0.1, 0.2375, 0., -0.1, 0.2375, 1., 0.3515625
*NGEN,NSET=NCBOT
258193,258257
258257,258321
*NCOPY, CHANGE NUMBER=1, OLD SET=NCBOT3, NEW SET=NCBOT, SHIFT, MULTIPLE=128
0., 0., 0.
0.1, 0.2375, 0., 0.1, 0.2375, 1., 0.3515625
*NCOPY, CHANGE NUMBER=1, OLD SET=NCBOT5, NEW SET=NCBOT, SHIFT, MULTIPLE=64
0., 0., 0.
0.1, 0.2375, 0., 0.1, 0.2375, 1., 0.703125
** CREATE NEAR BOTTOM (0.02013INCH FROM BOTTOM) OF CYLINDER
*NCOPY, CHANGE NUMBER=18000, OLD SET=NCBOT, NEW SET=NCBOT8, SHIFT
0., 0.02013
0., 0., 0., 0., 0., 1., 0.
** CREATE NODES BETWEEN NCBOT AND NCBOT8 NODES OF CYLINDER
*NFill, NSET=NCYL
NCBOT, NCBOT8, 18, 1000
** CREATE NODES BETWEEN NCBOT8 AND NCTOP NODES OF CYLINDER
*NFill, NSET=NCYL
NCBOT8, NCTOP, 238, 1000
**
** CREATE CYLINDER MESH WITH PLANE STRAIN ELEMENTS
*ELEMENT, TYPE=CPE4
113001, 258001, 258002, 259002, 259001
** CREATE 512 ELEMENTS (1-512) ALONG X AXIS AND 32 LAYERS ALONG Y-AXIS
*ELGEN, ELSET=ECYLIND1
113001, 512, 1, 1, 32, 1000, 1000
*ELEMENT, TYPE=CPE4
145001, 290001, 290003, 292003, 292001
** CREATE 256 ELEMENTS (1-256) ALONG X AXIS AND 48 LAYERS ALONG Y-AXIS
*ELGEN, ELSET=ECYLIND2
145001, 256, 2, 1, 48, 2000, 1000
*ELEMENT, TYPE=CPE4
193001, 386001, 386005, 390005, 390001
** CREATE 128 ELEMENTS (1-128) ALONG X AXIS AND 32 LAYERS ALONG Y-AXIS
*ELGEN, ELSET=ECYLIND3
193001, 128, 4, 1, 32, 4000, 1000
*ELSET, ELSET=ECYLINDR
ECYLIND1, ECYLIND2, ECYLIND3
*NSET,NSET=INDEPA2, GENERATE
290001,290511,2
*NSET,NSET=INDEPB2, GENERATE

```

```

290003,290513,2
*NSET,NSET=INDP2, GENERATE
290002,290512,2
*NSET,NSET=INDEPA3, GENERATE
386001,386509,4
*NSET,NSET=INDEPB3, GENERATE
386005,386513,4
*NSET,NSET=INDP3, GENERATE
386003,386511,4
*MPC
LINEAR,INDP2,INDEPA2,INDEPB2
LINEAR,INDP3,INDEPA3,INDEPB3
*SOLID SECTION, ELSET=ECYLINDR, MATERIAL=TI64
0.25,
**
** CREATE LATERAL SPRING PAD
*NODE
257961, -1.2, 0.2375
513961, -1.2, 0.45
** CREATE BOTTOM OF SPRING PAD
*NGEN, NSET=NSBOT
257961, 258001
** CREATE NEAR BOTTOM (0.02013INCH FROM BOTTOM) OF SPRING
*NCOPY, CHANGE NUMBER=18000, OLD SET=NSBOT, NEW SET=NSBOT1, SHIFT
0, 0.02013
0, 0, 0, 0, 0, 1, 0.
** CREATE TOP OF SPRING PAD
*NGEN, NSET=NSTOP
513961, 514001
* CREATE NODES BETWEEN NSBOT AND NSBOT1 NODES OF SPRING PAD
*NFill, NSET=NSPRPAD
NSBOT, NSBOT1, 18, 1000
** CREATE NODES BETWEEN NSBOT1 AND NSTOP NODES OF SPRING PAD
*NFill, NSET=NSPRPAD
NSBOT1, NSTOP, 238, 1000
** CREATE SPRING PAD MESH WITH PLANE STRAIN ELEMENTS
*ELEMENT, TYPE=CPE4
225001, 257961, 257962, 259962, 259961
** CREATE 40 ELEMENTS (1-40) ALONG X AXIS AND 64 LAYERS ALONG Y-AXIS
*ELGEN, ELSET=ESPRPAD
225001, 40, 1, 1, 64, 2000, 1000
*ELEMENT, TYPE=CPE4
289001, 385961, 385962, 389962, 389961
** CREATE 40 ELEMENTS (1-40) ALONG X AXIS AND 32 LAYERS ALONG Y-AXIS
*ELGEN, ELSET=ESPRPAD
289001, 40, 1, 1, 32, 4000, 1000
*NSET,NSET=INDEPA4, GENERATE
258001,288001,2000
*NSET,NSET=INDEPB4, GENERATE
260001,290001,2000
*NSET,NSET=INDP4, GENERATE
259001,289001,2000
*MPC
LINEAR,INDP4,INDEPA4,INDEPB4
*SOLID SECTION, ELSET=ESPRPAD, MATERIAL=SPRING

```

```

0.25,
*MATERIAL, NAME=SPRING
*ELASTIC, TYPE=ISO
5., 0.3
**
*ELSET, ELSET=EPTOP, GENERATE
1001, 1512
*ELSET, ELSET=ECBOT, GENERATE
113001, 113512
*ELSET, ELSET=ECTOP, GENERATE
224001, 224128
*NSET, NSET=NPLEFT, GENERATE
1001, 257001, 1000
*NSET, NSET=NSPLEFT, GENERATE
257961, 513961, 1000
**
**APPLY BOUNDARY CONDITIONS
*BOUNDARY, OP=NEW
NPBOT, 2, 2, 0.
NPLEFT, 1, 1, 0.
NSPLEFT, 1, 1, 0.
257961, 2, 2, 0.
**
*NGEN, NSET=NCTOP1
514001, 514065
514449, 514513
**
*EQUATION
2,
NCTOP1, 2, 1, 0, 514257, 2, -1.0
**
** DEFINE SURFACES
*SURFACE DEFINITION, NAME=SPLATE
EPTOP, S3
*SURFACE DEFINITION, NAME=SCYLINDR
ECBOT, S1
**
** SURFACE INTERACTION, OR CONTACT
*CONTACT PAIR, INTERACTION=SI1, SMALL SLIDING, ADJUST=1E-10
** SCYLINDR, SPLATE
SPLATE, SCYLINDR
*SURFACE INTERACTION, NAME=SI1
0.25
*FRICTION, LAGRANGE
0.75
***STEP, NLGEOM, INC=1000
**STATIC NONLINEAR CONTACT ANALYSIS
*STATIC
0.1, 1.
*DLOAD
ECTOP, P3, 3200.
**
** OUT PUT TO DAT FILE EVERY 100 INCREMENT (DEFAULT IS LAST ALWAYS)
*NODE PRINT, FREQ=10
U, RF

```

```

*EL PRINT, POSITION=AVERAGED AT NODES, FREQ=10
S,
E,
**
** OUT PUT TO FIL FILE EVERY INCREMENT (TO READ TO PATRAN)
*NODE FILE, FREQ=10
U,RF
*EL FILE, FREQ=10
S,
E,
**
*PRINT, FREQ=1, CONTACT=YES
**
*CONTACT PRINT, FREQ=10
*CONTACT FILE, FREQ=10
**
*END STEP
**
** STEP 2, ADD HORIZONTAL FORCE  $Q=0.5 \cdot P \cdot (\text{FRICTION COEFICIENT})$ 
** STEP 3, ADD BULK TENSILE STRESS
**
*STEP, NLGEOM, INC=1000
**
*STATIC
0.1, 1.0
**
*BOUNDARY, OP=MOD
**
*ELSET, ELSET=QPRESS, GENERATE
113001,224001,1000
**
*ELSET, ELSET=BULKST, GENERATE
1512,32512,1000
33256,80256,1000
81128,112128,1000
**
**
*DLOAD
QPRESS, P4, -378.32
BULKST, P2, -79413.0
**
*END STEP
*STEP, NLGEOM, INC=1000
**
*STATIC
0.1, 1.0
**
*BOUNDARY, OP=MOD
**
*ELSET, ELSET=QPRESS, GENERATE
113001,224001,1000
**
*ELSET, ELSET=BULKST, GENERATE
1512,32512,1000
33256,80256,1000

```

81128,112128,1000

**

**

*DLOAD

QPRESS, P4, 378.32

BULKST, P2, 79413.0

**

*END STEP

APPENDIX C

Residual Stress Input File Format

C.1 The Residual Stress Input File Format

FLG Comments

FLG XCoord YCoord

SIG X SIG Y SIG XY SIG Z

EPS X EPS Y GAM XY EPS Z

This line is inserted for one time only at the beginning of the input file.

These lines are repeated as many times as the number of points desired to define the residual stresses and strains through the model thickness.

C.2 Detailed Description

Comment line:

FLG Comments

where:

FLG - One character flag field that must contain the value "C" or "c". This flag should always be placed in the first column.

Comments - String of characters with any desired comment.

Main line:

FLG XCoord YCoord

where:

FLG - One character flag field that must contain the value "B" or "b" for point located at the model boundary or "I" or "i" for point located inside of the model.

XCoord – The X coordinate of this point.

YCoord – The Y coordinate of this point.

Data line:

For stresses:

SIG X SIG Y SIG XY SIG Z

where:

SIG X SIG Y SIG XY SIG Z – The residual stress components

For strains:

EPS X EPS Y GAM XY EPS Z

where:

EPS X EPS Y GAM XY EPS Z – The residual strain components

Note that in the current dissertation there are no residual strains. Therefore, zero values were inserted in this line.

BIBLIOGRAPHY

- [1] Szolwinski, M. P. and Farris, T. N., "Mechanics of Fretting Fatigue Crack Formation," *Wear*, 1996; 198:93-107.
- [2] Golden, P. J., Bartha, B. B., Grandt, A. F., Jr, and Nicholas, T., "Measurement of the Fatigue Crack Propagation Threshold of Fretting Induced Cracks in Ti-6Al-4V," *International Journal of Fatigue*, 2004; 26:281-288.
- [3] Golden, P. J. and Grandt, A. F., "Fracture Mechanics Based Fretting Fatigue Life Predictions in Ti-6Al-4V," *Engineering Fracture Mechanics*, 2004; 71:2229-2243.
- [4] Leiva, O., "Effect of Shear Load on Fretting Fatigue Behavior of Ti-6Al-4V," PhD. Dissertation, University of Dayton, 2003.
- [5] Dobromirski, J. M., "Variables of Fretting Process: Are There 50 of Them?," in *Standardization of Fretting Fatigue Test Methods and Equipment*, ASTM STP 1159, (Eds.) M. H. Attia and R. B. Waterhouse, American Society for Testing and Materials, Philadelphia, PA, 1992: 60-66.
- [6] Iyer, K. and Mall, S., "Analysis of Contact Pressure and Stress Amplitude Effects on Fretting Fatigue Life," *ASME Journal of Engineering Materials and Technology*, 2001; 123:85-93.
- [7] Hoepfner, D. W., "Mechanism of Fretting Fatigue," in *Fretting Fatigue*, ESIS 18, (Eds.) R. B. Waterhouse and T. C. Lindley, Mechanical Engineering Publications, London, 1994: 3-19.
- [8] Adibnazari, S. and Hoepfner, D., "The Role of Normal Pressure in Modeling Fretting Fatigue," in *Fretting Fatigue*, ESIS 18, (Eds.) R. B. Waterhouse and T.C. Lindley, Mechanical Engineering Publications, London, 1994: 125-133.
- [9] Nakazawa, K., Sumita, M., and Maruyama, N., "Effect of Contact on Fretting Fatigue of High Strength Steel and Titanium Alloy," in *Standardization of Fretting Fatigue Test Methods and Equipment*, ASTM STP 1159, (Eds.) M. H. Attia and R. B. Waterhouse, American Society for Testing and Materials, Philadelphia, PA, 1992: 115-125.
- [10] Lee, S.K., Nakazawa, K., Sumita, M., and Maruyama, N., "Effects of Contact Load and Contact Curvature Radius of Cylindrical Pad on Fretting Fatigue in High Strength Steel," in *Fretting Fatigue: Current Technology and Practices*, ASTM STP 1367, (Eds.)

D. W. Hoepfner, V. Chandrasekaran, and C. B. Elliott III, American Society for Testing and Materials, West Conshohocken, PA, 2000: 199-212.

- [11] Nishioka, K. and Hirakawa, K., "Fundamentals Investigations into Fretting Fatigue," Bulletin of J.S.M.E., 1969; 12(50):180-187.
- [12] Nix, K. J. and Lindley, T. C., "The Influence of Relative Slip Range and Contact Materials on the Fretting Fatigue Properties of 3.5 NiCrMo V Rotor Steel," Wear, 1988; 125:147-162.
- [13] Endo, K., Goto, H., and Fukunaga, T., "Behavior of Friction Force in Fretting Fatigue," Bulletin of J.S.M.E., 1974; 17(108):647-654.
- [14] Vingsbo, O. and Söderberg, S., "On Fretting Maps," Wear, 1988; 126:131-147.
- [15] Jin, O. and Mall, S., "Effects of Independent Pad Displacement on Fretting Fatigue Behavior of Ti-6Al-4V," Wear, 2002; 253:585-596.
- [16] Wallace, J. M. and Neu, R. W., "Fretting Fatigue Crack Nucleation in Ti-6Al-4V," Fatigue Fract. Engng. Mater. Struct., 2003; 26:199-214.
- [17] Iyer, K., "Peak Contact Pressure, Cyclic Stress Amplitude, Contact Semi-Width and Slip Amplitude: Relative Effects on Fretting Fatigue Life," International Journal of Fatigue, 2001; 23:193-206.
- [18] Nowell, D., Hills, D. A., and Moobola, R., "Length Scale Considerations in Fretting Fatigue," in Fretting Fatigue: Current Technology and Practices, ASTM STP 1367, (Eds.) D. W. Hoepfner, V. Chandrasekaran, and C. B. Elliott III, American Society for Testing and Materials, West Conshohocken, PA, 2000: 141-153.
- [19] Lykins, C. D., "An investigation Of Fretting Fatigue Crack Initiation Behavior on the Titanium Alloy Ti-6Al-4V," PhD. Dissertation, University of Dayton, 1999.
- [20] Lykins, C. D., Mall, S., and Jain, V., "An Evaluation of Parameters for Predicting Fretting Fatigue Crack Initiation," International Journal of Fatigue, 2000; 22:703-716.
- [21] Lykins, C. D., Mall, S., and Jain, V., "A Shear Stress-Based Parameter for Fretting Fatigue Crack Initiation," Fatigue Fract. Engng. Mater. Struct., 2001; 24:461-473.
- [22] Fannes, S., "Inclined Cracks in Fretting Fatigue," Engineering Fracture Mechanics, 1995; 52:71-82.
- [23] Mutoh, Y., Xu, J.O., and Kondoh, K., "Observations and Analysis of Fretting Fatigue Crack Initiation and Propagation," in Fretting Fatigue: Advances in Basic Understanding and Applications, ASTM STP 1425, (Eds.) Y. Mutoh, S. Kinyon, and D. W. Hoepfner, American Society for Testing and Materials, West Conshohocken, PA, 2003: 61-75.

- [24] Erdogan, F. and Sih, G. C., "On The Crack Extension in Plates Under Plane Loading and Transverse shear," *ASME Journal of Basic Engineering*, 1963; 85(4):519-527.
- [25] Shkarayev, S. and Mall, S., "Computational Modeling of Shot-Peening Effects on Crack Propagation Under Fretting Fatigue," *Journal of Strain Analysis*, 2003; 38:495-506.
- [26] Navarro, C., Garcia, M., and Dominguez, J., "A Procedure for Estimating the Total Life in Fretting Fatigue," *Fatigue Fract. Engng. Mater. Struct.*, 2003; 26:459-468.
- [27] Navarro, C., Garcia, M., and Dominguez, J., "An Estimation of Life in Fretting Fatigue Using an Initiation-Propagation Model," in *Fretting Fatigue: Advances in Basic Understanding and Applications*, ASTM STP 1425, (Eds.) Y. Mutoh, S. Kinyon, and D. W. Hoepfner, American Society for Testing and Materials, West Conshohocken, PA, 2003: 121-132.
- [28] Paris, P. C. and Erdogan, F., "A Critical Analysis of Crack Propagation Laws," *Journal of Basic Engineering*, 1960; 85:528-534.
- [29] Lankford, J., "The Growth of Small Fatigue Cracks in 7075-T6 Aluminum," *Fatigue Engng. Mater. Struct.*, 1982; 5:233-248.
- [30] "Improved High Cycle Fatigue Life Prediction," AFRL-ML-WP-TR-2001-4159, Material and Manufacturing Directorate, Air Force Research Laboratory, WPAFB, Ohio 45433-7750, January 2001.
- [31] Walker, K., "The Effect of Stress Ratio During Crack Propagation and Fatigue for 2024-T3 and 7075-T6 Aluminum," in *Effects of Environment and Complex Load History on Fatigue Life*, ASTM STP 462, (Eds.) M. Rosenfeld, D. W. Hoepfner, and R. I. Stephens, American Society for Testing and Materials, West Conshohocken, PA, 1970: 1-14.
- [32] Haritos, G. K., Nicholas, T., and Painter, G. O., "Evaluation of Crack Growth Models for Elevated-Temperature Fatigue," in *Fracture Mechanics: Eighteens Symposium*, ASTM STP 945, (Eds.) D. T. Read and R. P. Reed, American Society for Testing and Materials, Philadelphia, PA, 1988: 206-220.
- [33] Nicholas, T., Huston, A., John, R., and Olson, S., "A Fracture Mechanics Methodology Assessment for Fretting Fatigue," *International Journal of Fatigue*, 2003; 25:1069-1077.
- [34] Kitagawa, H. and Takahashi, S., "Applicability of Fracture Mechanics to Very Small Cracks or the Cracks in the Early Stage," in *Proceedings of Second International Conference on Mechanical Behavior of Materials*, Boston, MA, 1976: 627-631.
- [35] Chan, K. S., Lee, Y.-D., Davidson, D. L., and Hudak Jr., S. J., "A Fracture Mechanics Approach to High Cycle Fretting Fatigue Based on the Worst Case Fret Concept," *International Journal of Fracture*, 2001; 112:299-330.

- [36] Waterhouse, R. B., "Avoidance of Fretting Fatigue Failures," in Fretting Fatigue, (Ed.) R. B. Waterhouse, Applied Science Publishers, London, 1981: 221-240.
- [37] Leadbeater, G., Noble, B., and Waterhouse, R. B., "The Fatigue of an Aluminum Alloy Produced by Fretting on Shot-Peened Surfaces," Proceedings of 6th Int. Conf. On Fracture, India, 1984; 3:2125-2132.
- [38] Gabel, M. K. and Bethk, J. J., "Coatings for Fretting Prevention," Wear, 1979; 46:81-96.
- [39] Vardiman, R. G. and Creighton, D., "Effect of Ion Implantation on Fretting Fatigue in Ti-6Al-4V Alloy," in Materials Evaluation under Fretting Conditions, ASTM STP 780, (ED.) S. R. Brown, American Society for Testing and Materials, West Conshohocken, PA, 1982: 138-149.
- [40] Tanaka, K., Mutoh, Y., and Sakoda, S., "Effect of Contact Materials on Fretting Fatigue in a Spring Steel," Trans. J.S.M.E., Ser. A, 1985; 51(464):1200-1207.
- [41] Namjoshi, S. A., Jain, V. K., and Mall, S., "Effects of Shot-Peening on Fretting Fatigue Behavior of Ti-6Al-4V," Journal of Engineering Material Technology, 2002; 124:1-7.
- [42] Lee, H., Jin, O., and Mall, S., "Fretting Fatigue Behavior of Shot-Peened Ti-6Al-4V at Room and Elevated Temperatures," Fatigue Fract. Engng. Mater. Struct., 2003; 26:767-778.
- [43] Vohringer, O., "Changes in the State of the Material by Shot-Peening," in Proceedings of the Third International Conference on Shot-Peening, Shot-Peening: Science, Technology, Applications, (Eds.) H. Wohlfahrt, R. Koop, and O. Vohringer, InformationsGessellschaft, 1987:221-230.
- [44] Sabelkin, V., Martinez, S. A., Mall, S., Sathish, S., and Blodgett, M. P., "Effects of Shot-Peening Intensity on Fretting Fatigue Crack Initiation Behavior of Ti-6Al-4V," Fatigue Fract. Engng. Mater. Struct., 2005; 28:321-332.
- [45] Miyoshi, K., Lerch, B. A., and Draper, S. L., "Fretting Wear Of Ti-48Al-2Cr-2Nb," Tribology International, 2003; 36:145-153.
- [46] Hills, D. A. and Nowell, D., Mechanics of Fretting Fatigue, Kluwer Academic Publishers, Dordrecht, 1994.
- [47] Fellows, L. J., Nowell, D., and Hills, D. A., "Contact Stresses in Moderately Thin Strip," Wear, 1995; 185:235-238.
- [48] Muskhelishvili, N. I., Some Basic Problems of the Mathematical Theory of Elasticity, Noordhoff, Gröningen, 1953.
- [49] Hills, D. A., Nowell, D., and Stackfield, A., Mechanics of Elastic Contacts, Butterworth-Heinemann, Oxford, 1993.

- [50] Mindlin, R., "Compliance of Elastic Bodies in Contact," *Journal of Applied Mechanics*, 1949; 16:259-268.
- [51] Nowell, D. and Hills, D. A., "Mechanics of Fretting Fatigue Tests," *International Journal of Mechanical Science*, 1987; 29.5:355-365.
- [52] Gladwell, G. M. L., Contact Problems in the Classical Theory of Elasticity, Sijthoff and Noordhoff International Publisher, Alphen aan den Rijn, The Netherlands, 1980.
- [53] Inglis, C. E., "Stresses in a Plate due to Presence of Cracks and Sharp Corners," *Transactions of the Institute of Naval Architect*, 1913; 55(1):219-241.
- [54] Griffith, A. A., "The Phenomena of Rupture and Flow in Solids," *Philosophical Transactions of the Royal Society*, 1921; A221:163-198.
- [55] Kanninen, M. F. and Popelar, C. H., Advanced Fracture Mechanics, Oxford University Press, New York, 1985.
- [56] Irwin, G., Kies, J. A., and Smith, H. L., "Fracture Strengths Relative to Onset and Arrest of Crack Propagation," *Proceedings of American Society for Testing Materials*, 1958; 58:640-657.
- [57] Hussain, M. A., Pu, S. L., and Underwood, J. H., "Strain Energy Release Rate for a Crack under Combined Mode I and II," in *Fracture Analysis*, ASTM STP 560, (Eds.) P. C. Paris and G. R. Irwin, 1974: 2-28.
- [58] Sih, G. C., "Strain-Energy-Density Factor Applied to Mixed-Mode Crack Problems," *Int. Journal of Fracture*, 1974; 10:305-321.
- [59] Miranda, A. C. O., Meggiolaro, M. A., Castro, J. T. P., Martha, L. F., and Bittencourt, T. N., "Fatigue Life and Crack Path Predictions in Generic 2D Structural Components," *Engineering Fracture Mechanics*, 2003; 70:1259-1279.
- [60] Bittencourt, T. N., Wawrzynek, P. A., Ingraffea, A. R., and Sousa, J. L. A., "Quasi-Automatic Simulation of Crack Propagation for 2D LEFM Problems," *Engineering Fracture Mechanics*, 1996; 55:321-334.
- [61] Shih, C. F., De Lorenzi, H. G., and German, M. D., "Crack Extension Modeling with Singular Quadratic Isoparametric Elements," *Int. Journal of Fracture*, 1976; 12:647-651.
- [62] Bittencourt, T. N., "Computer Simulation of Linear and Nonlinear Crack Propagation in Cementitious Materials," PhD. Dissertation, Cornell University, 1993.
- [63] Rice, J. R., "Weight Function Theory for Three-Dimensional Elastic Cracks," in *Fracture Mechanics: Perspectives and Directions (20th Symposium)*, ASTM STP 1020, (Eds.) E. P. Wei and R. P. Gangloff, 1989; 29-57.

- [64] Dodds Jr., R. H. and Vargas, P. M., "Numerical Evaluation of Domain and Contour Integrals for Nonlinear Fracture Mechanics: Formulation and Implementation Aspects," Report, University of Illinois at Urbana-Champaign, Department of Civil Engineering, 1988.
- [65] Denyse de Araujo, T., Bittencourt, T. N., Roehl, D., and Martha, L. F. "Numerical Estimation of Fracture Parameters in Elastic and Elastic-Plastic Analysis," European Congress on Computational Methods in Applied Sciences and Engineering, Barcelona, Spain, 2000:328.1-328.18.
- [66] Knowles, J. K. and Sternberg, E., "On a Class of Conservation Laws in Linearized and Finite Elastostatics," Archives for Rational Mechanics & Analysis, 1972; 44:187-211.
- [67] Hellen, T. K. and Blackburn, W. S., "Non-Linear Fracture Mechanics and Finite Elements," Engineering Computation, 1987; 4:2-14.
- [68] Bui, H. D. and Blackburn, W. S., "Associated Path Independent J-Integrals for Separating Mixed Modes," J. Mech. Phys. Solids, 1983; 31(6):439-448.
- [69] Chen, K. L. and Alturi, N., "Comparison of Different Methods of Evaluation of Weight Functions for 2D Mixed-Mode Fracture Analysis," Engineering Fracture Mechanics, 1989; 34(4):935-956.
- [70] Nikishkov, G. P. and Alturi, N., "Calculation of Fracture Mechanics Parameters for an Arbitrary Three-Dimensional Crack by the 'Equivalent Domain Integral' method," International Journal of Numerical Methods in Engineering, 1987; 24:1801-1821.
- [71] Rybicki, E. F. and Kanninen, M. F., "A Finite Element Calculation of Stress Intensity Factors by a Modified Crack Closure Integral," Engineering and Fracture Mechanics, 1977; 9:931-938.
- [72] Meggiolaro, M. A., Castro, J. T. P., Miranda, A. C. O., Martha, L. F., and Bittencourt, T. N., "Prediction of Fatigue Life and Crack Path in Generic 2D Structural Components under Complex Loading," Anais do 16o Congresso Brasileiro de Engenharia Mecanica (COBEM), Fracture Mechanics and Structural Integrity, 2001; 12:257-266.
- [73] Raju, I. S., "Calculation of Strain-Energy Release Rates with Higher Order and Singular Elements," Engineering and Fracture Mechanics, 1987; 28(3):251-274.
- [74] Ramamurthy, T. S., Krishnamurthy, T. S., Badarinarayana, K., Vijayakumar, K., and Dataguru, B., "Modified Crack Closure Integral Method with Quarter Point Elements," Mech. Research. Comm., 1986; 13(4):179-186.
- [75] Anderson, T. L., Fracture Mechanics: Fundamentals and Applications, 2nd Edition, CRC Press, USA, 1995.
- [76] Final Report, USAF Contract F33615-96-C-5269, "Improved High Cycle Fatigue Life Prediction," University of Dayton Research Institute Prime Contractor, August 1999.

- [77] El Haddad, M. H., Smith, K. N., and Topper, T. H., "Fatigue Crack Propagation of Short Cracks," *J. Eng. Mater. Techno.*, 1979; 101:42-46.
- [78] Tanaka, K., Nakai, Y., and Yamashita, M., "Fatigue Growth Threshold of Small Cracks," *International Journal of Fracture*, 1981; 17:519-533.
- [79] Chan, K. S., "Fatigue Crack Growth Thresholds of TiAl Alloys," *Proceeding of the 2nd International Symposium of Gamma Titanium Aluminide*, TMS, 1999; 517-525.
- [80] Brown, C. W., and Taylor, D., "The Effects of Texture and Grain Size on the Short Fatigue Crack Growth Rates in Ti-6Al-4V," In *Fatigue Crack Growth Threshold Concepts*, Metallurgical Society of AIME, (Eds.) D. L. Davidson and S. Suresh, 1984; 433-445.
- [81] Yuksul, H. I., "Effects of Shot-Peening on High Cycle Fretting Fatigue Behavior of Ti-6Al-4V," *Master Thesis, Air Force Institute of Technology at WPAFB*, 2002.
- [82] Jin, O., Lee, H., and Mall, S., "Investigation into Cumulative Damage Rules to Predict Fretting Fatigue Life of Ti-6Al-4V under Two-Level Block Loading Condition," *Journal of Engineering Materials and Technology*, 2003; 125:315-323.
- [83] Namjoshi, S. A., Mall, S., Jain, V. K., and Jin, O., "Fretting Fatigue Crack Initiation Mechanism in Ti-6Al-4V," *Fatigue Fract. Engng. Mater. Struct.*, 2002; 25:955-964.
- [84] Namjoshi, S. A. and Mall, S., "Fretting Behavior of Ti-6Al-4V under Combined High Cycle and Low Cycle Fatigue Loading," *International Journal of Fatigue*, 2001; 23:S455-S461.
- [85] Lykins, C. D., Mall, S., and Jain, V. K., "Combined Experimental-Numerical Investigation of Fretting Fatigue Crack Initiation," *International Journal of Fatigue*, 2001; 23:703-711.
- [86] ABAQUS v 6.3 Standard User Manual, RI (USA), Hibbit Karlsson & Sorensen, Inc., 2002.
- [87] Beisheim, J. R. and Sinclair, G. B., "On the Three-Dimensional Finite Element Analysis of Dovetail Attachments," *Journal of Turbomachinery*, 2003; 125:372-379.
- [88] Dowling, N. E., Mechanical Behavior of Materials: Engineering Methods for Deformation, Fracture, and Fatigue, 2nd Edition, Prentice-Hall Inc., United States of America, 1999.
- [89] Shaw, R. D. and Pitchen, R. G., "Modifications to the Suhara-Fukuda Method of Network Generation," *Int. J. Numer. Meth. Eng.*, 1978; 12:93-99.

R702031733